The Role of Mechanical Forces in Patterning and Morphogenesis of the Vertebrate Gut

The Role of Mechanical Forces in Patterning and Morphogenesis of the Vertebrate Gut

A dissertation presented

by

Amy Elizabeth Shyer

to

The Division of Medical Sciences

in partial fulfillment of the requirements

for the degree of

Doctor of Philosophy

in the subject of

Cell and Developmental Biology

Harvard University

Cambridge, Massachusetts

April 2013

Dissertation Advisor: Dr. Clifford J. Tabin Amy Elizabeth Shyer

The Role of Mechanical Forces in Patterning and Morphogenesis of the Vertebrate Gut

Abstract

The vertebrate small intestine is responsible for nutrient absorption during digestion. To this end, the surface area of the gut tube is maximally expanded, both through a series of loops extending its length and via the development of a complex luminal topography.

Here, I first examine the mechanism behind the formation of intestinal loops. I demonstrate that looping morphogenesis is driven by mechanical forces that arise from differential growth between the gut tube and the anchoring dorsal mesenteric sheet. A computational model based on measured parameters not only quantitatively predicts the looping pattern in chick, verifying that these physical forces are sufficient to explain the process, but also accounts for the variation in the gut looping patterns seen in other species.

Second, I explore the formation of intestinal villi in chick. I find that intestinal villi form in a stepwise process as a result of physical forces generated as proliferating endodermal and mesenchymal tissues are constrained by sequentially differentiating layers of smooth muscle. A computational model incorporating measured differential

growth and the geometric and physical properties of the developing chick gut recapitulates the morphological patterns seen during chick villi formation. I also demonstrate that the same basic biophysical processes underlie the formation of intestinal folds in frog and villi in mice.

Finally, I focus on the process by which intestinal stem cells are ultimately localized to the base of each villus. The endoderm expresses the morphogen, Sonic hedgehog (Shh). As the luminal surface of the gut is deformed during villus formation there are resulting local maxima of Shh signaling in the mesenchyme. This results, at high threshold, in the induction of a new signaling center under the villus tip termed the villus cluster. This, in turn, feeds back to restrict proliferating progenitors in the endoderm, the presumptive precursors of the stem cells, to the base of each villus.

Together, these studies provide new insight into the formation of the small intestine as a functional organ and highlight the interplay between physical forces, tissue-level growth, and signaling during development.

Table of Contents

List of Figures and Tables

Chapter One: General Introduction

Chapter Two: On the Growth and Form of the Gut

Chapter Three: Villification

Chapter Four: Epithelial Topography Mediates Localization of Proliferating Progenitors to the Presumptive Intestinal Stem Cell Niche

Acknowledgements

My first exposure to the big wide world of what a lab can be came early. My grandmother was a research technician in a lab that studied toxoplasmosis until she retired at the spritely age of 80. Back in the days when I was bottom drawer-height, she would keep the bottom drawer of her bedroom dresser stocked with curious containers that served as bowling pins for Barbie and stealth jelly bean holders. Only later did I realize these were falcon tubes and scintillation vials, and that my play things from back then are now the stuff of work. – I am confident the lab ware was unused… Looking back, I am a grateful that she encouraged me in all my pursuits, even my brief foray into Barbie bowling, and that she also nudged the nuts and bolts of day-to-day lab life towards me right from the start.

My dad has a flare for the humanities but begrudgingly has jumped on the biology bandwagon simply because I expressed interest sometime in high school. Ever since, as a teenager, I somewhat casually laid claim to having an interest in neuroscience my dad has been energetically clipping out newspaper articles – "Oh, Amy I saw this article…". In the name of rebellion, I often cast the carefully clipped pieces to the side only to be hounded with "Did you read that article I gave you??". I didn't read all the articles, and I still don't always get to the ones he emails me, but I cherish having a parent who so willingly obsesses over whatever I decide matters to me. And I smile whenever he mentions a new article as I know it means he's thinking of me.

I would consider myself so lucky to end up just like my mom. I've never known anyone with a stronger work ethic or generosity of spirit ("I wanted to sit outside!"). I

still remember our conversation when I was deciding whether to leave my cozy life in the Bay Area to come to Boston, I could not have made this move without her support. I knew when I left that giving up our Sundays together would be difficult, but it was much harder than I imagined. Still, I can't count how many times my walk home was brightened by a call home to get her council on some grown-up decision, or by a package of cookies greeting my at my front door (that's right, my mom still sends me care packages!). My mom's been with me for this whole ride in Boston – she's in my beautiful quilt, my very functional curtains, and those creative pj pants, and I could not have done it without her.

My brother Justin turned out to be a scientist too, but it would be wrong to say he's been following in my footsteps as he's always been wise beyond his years and an inspiration to me. There's no one I'd rather spend time with and I hope he remembers the little people like me when he's a big shot.

I spent several years working in David Krantz's lab at UCLA. David is a patient, smart, genuine person and mentor. My time in this lab taught be a lot about how a lab works generally, how to troubleshoot (we did lots of troubleshooting), and generally how to work with people. I am indebted to my first mentor in the Krantz Lab, David Patton, who was diagnosed with MS the first week I worked in the lab. He asked me then to be his hands and his second opinion going forward. I still use my pipette tips in order like he taught me, and remember that when you grab a handful tubes, and it turns out to be just the right number, it's going to be a good experiment.

After college, I was hired as a technician in Jeremy Reiter's lab at UCSF. I told myself if I still loved science after a year or two I'd apply to grad school. Under Jeremy's mentorship I grew more confident that I wanted to pursue research. Jeremy also helped me fall in love with development (he had me at his gastrulation dance). It's amazing to watch his brilliant mind work, and his high expectations (the lab called me A-team) pushed me to grow. I worked closely with a senior postdoc in the lab, Kevin Corbit. Kevin taught me how to plan and carry out experiments and how to interpret results. He helped me laugh at my mistakes, push through the disappointments, and celebrate the small victories. He's also brilliant and an excellent experimentalist. I'll always remember working with Kevin as one of the highlights of my training. The graduate students in Jeremy's lab took me in as one of their own, and I'm especially grateful to have come away with Bill and Veena as friends.

Since coming to graduate school, my work has consistently involved collaboration with L. Mahadevan. I could have never predicted my thesis work would take this turn towards the world of physics (I hated physics in college!) but I am so grateful to have had the chance to work closely with Maha. No one can so elegantly clarify complicated notions of physics and mechanics for me better than he can, and I have learned so much from our collaboration - I like physics now. I have worked with two postdocs from his Maha's lab, Thierry Savin and Tuomas Tallinen who have been ideal research partners. I am also grateful to the other members of my DAC, Max Heiman and Ramesh Shivdasani for their attentiveness and careful feedback along the way.

I knew I wanted to join the Tabin lab from the first day of my rotation. I loved it then and I love it more now. Cliff is exceptional. The words "hands off" get thrown around a lot, but Cliff is always accessible and his email response time is unmatched, it's truly amazing how supportive he is. I've loved our weekly meetings and am so grateful for the intellectual and personal council he's provided. I have certainly been spoiled by his generosity, and fear it will never be matched.

One of the greatest gifts Cliff provides is a lab full of people who are a delight to be around and at the same time an invaluable scientific resource. I'll admit I plan my experiments around lunch in order to ensure I don't miss out on whatever is on the day's conversation docket. From cell culture to cephalopods, there's no telling what I'll learn or laugh about. Thanks to Amanda, Karolina, Lehoczky, Yana, Jenna, Eddy, Aysu, J.C., Christina, and Abby for all of our lunch dates. I also count my blessings that Nandan joined the lab. His ability to speak the language of physics has been so valuable and I am grateful for all of his council and experimental contribution. I'm always pleased when he steals a seat at a neighboring scope in the chick room, as I know we'll be laughing or talking about food, or both.

I have a very special bench, as it is in Bay 6 - the best bay. Wenjia, Veeda (and of course Dan) currently complete our ladies-only bay and make coming to work a pleasure. I also have to thank Jimmy and Aysu, my scrabble opponents and dear friends for making Bay 6 home. I'm so happy to have made a friend in Matt, he makes me laugh and is just genuinely excited about exploring science. My time in Boston would have been bleak without my 'only friend' Maija. I'm inspired by how strong she is (not just her biceps – sweaterballs!) and might not have made it through this without her.

I'm so lucky to have a partner who brings out the wonder in me, Alan, you were an unexpected result, but those are always the best kind. Here's to keeping the party going.

I find myself just so happy surrounded by the entire Cepko-Tabin crew and can't imagine doing science without passing these people in the hall, bothering them with experimental questions, and catching up in the lunch room. I hope the spirit week tradition is carried on, and that it is an annual reminder of how lucky we are to be a part of this place.

Dedication

To Dorothy

Who told me, “If something is impossible, it just takes longer.”

Chapter One

General Introduction

The mechanics of development

An enduring goal of biology is to understand the emergence of morphologies during development. The last decades have seen enormous progress in understanding this process in various settings, with a focus on the critical role of morphogenic signals, tissue interactions, and transcriptional networks in patterning early fields of naive progenitors. However, lasting gaps in our understanding of how tissues take their shape suggest that the dominant approaches of the last several decades may not provide us with a compete tool set with which to address questions of morphogenesis. In fact, a century ago, a mechanical view of how shapes and structures form in the embryo prevailed: In his seminal 1907 work, *On Growth and Form*, D'Arcy Thompson provide an apt description of biological patterns as "diagrams of underlying forces". Indeed, the last decade has seen a renewed interest in how mechanical forces shape biological structures, with a focus on combining molecular insights with biomechanical investigation of how the embryo takes its shape.

Studies at the intersection of physics and biology have highlighted the role of mechanical forces in development on molecular, cellular, and tissue levels (Davidson 2011). At the molecular level, forces are translated into chemical cues within the cell, instigating gene expression and downstream cellular behaviors such as proliferation or cell death (Farge 2011). The development of synovial joints provides an excellent example of a developmental setting where forces are translated at the molecular level. During development, progenitor cells differentiate into synovial joints just as the adjacent muscle is developing. While the role of musculature in joint formation has been long appreciated (Drachman and Sokoloff 1966), the molecular underpinnings are still under

investigation. More recent work demonstrates that β-catenin is mechanically activated in the forming joint by oscillation of the muscle during development (Kahn et al. 2009). In several different genetic mouse models that lack muscle or muscle contraction, β-catenin is not activated in joint progenitors and joints do not form in adults (Kahn et al. 2009). Therefore, in synovial joint formation, muscle-driven mechanical strain induces genetic changes necessary for proper development. Our understanding of this type of cellular mechanosensing is still evolving, but much of what is known involves focal adhesions, adherens junctions, and stretch-activated ion channels. These molecules change shape in response to force, prompting a cascade of biochemical events within the cell (Farge 2011).

Additionally, the study of epithelial behavior had benefitted from biomechanical exploration as, in developing tissues, epithelia both experience and exert mechanical forces as they move, bend, and fold into patterned structures (Davidson 2012). A recent study highlights the importance of force in epithelial movement during zebrafish gastrulation (Behrndt et al. 2012). The authors find a contracting actomyosin band acts as a purse string, inducing the spreading of an epithelial layer termed the enveloping cell layer (EVL) over the yolk cell (Behrndt et al. 2012). This is an important example of the developmental role of actin purse strings, however, the actomyosin band in zebrafish EVL spreading also exerts a friction-base pulling force, revealing a novel mechanical function for the actomyosin band. Such studies highlight the many ways mechanical forces contribute to epithelial movements.

Mechanical forces can also be exerted on the tissue-level, inducing organs to take their shape. The chick embryo has proved to be a valuable system for these type of

studies. Recent work demonstrates that the vesicles of the chick brain are shaped by variations in actomyosin contractility across an initially uniform tube, thus dividing the tube into segments (Filas et al. 2012a). An additional study extends these findings to zebrafish, artificially varying contractility patterns and in zebrafish to mimic those of *Xenopus* (Filas et al. 2012b). This study explores the idea that spatiotemporal patterns of tissue contractility are varied across species to produce a diversity of vesicle patterns.

The vertebrate gut as a model for mechanical studies of development

The midgut is a favorable system for starting to analyze how mechanical forces participate in morphogenic processes, as it is a relatively simple structure, initially forming as a linear tube running down the midline of the embryo and ultimately forming a twisted and coiled cylinder that maintains radial symmetry throughout its length.

The human intestine is approximately 20 feet long, a fact which immediately brings to mind concerns about space - how can we efficiently fit such a long structure into the small space it is allotted in the body. Perhaps its apt to draw a comparison to the well-studied phenomenon of how DNA is packed into the cell's nucleus. In both cases some sort of folding or looping must occur to accommodate space constraints. Although this organ may appear as a jumble of loops, the loops are actually patterned identically within a species meaning that every individual within a species will have the same size and number of loops. However, looping pattern varies significantly between species (Figure 1.1). In fact, these structures have had taxonomic value and were used in

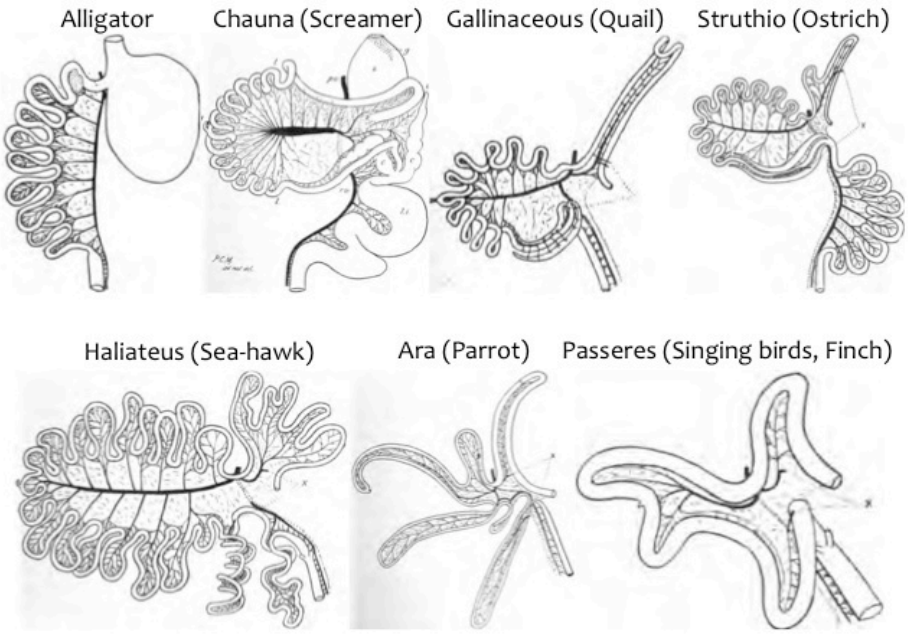

Figure 1.1. Variation in looping pattern across species. Looping patterns were believed to have taxonomic value and have been used to classify bird species. Adapted from *On the Intestinal Tract of Birds, Chalmers Mitchell, 1896*

the past to classify bird species (Beddard et al. 1898, Mitchell et al. 1896). It's tempting to speculate about the ways in which these variations are tied to differences in diet and energy needs between species.

While the looping pattern provides an artful mechanism for fitting a longer gut tube into the body, undoubtedly contributing to the luminal surface area necessary for optimal nutrient absorption, one can imagine alternative mechanisms to increase surface area such as altering the morphology of the luminal tissue. And in fact, the lumen of the intestine is covered with finger-like projections termed villi. And these villi indeed serve to dramatically increase the surface area of the intestine, allowing that of the human intestine to reach an astounding 200 square meters, roughly the size of a tennis court.

Again these patterns seem to vary widely between species suggesting villi shape and number may have to be adjusted in nature to fit the need of the species. The fact that looping and villi pattern are so freely modulated in nature makes the question of how they form even more enticing, and I investigate these open questions in Chapters Two and Three. My explorations of how villi form motivated an investigation of the process by which intestinal stem cells are ultimately localized to the base of each villus during development. In Chapter Four, I focus on how mechanically-driven morphogenesis of the gut epithelium drives proliferating progenitors to their presumptive niche. I'll begin with a summary of our current understanding of vertebrate gut development.

Initiating left-right asymmetry and looping in the vertebrate gut

Although the external body plan of vertebrate species displays almost perfect bilateral symmetry, the internal layout of various organs including the heart, gut,

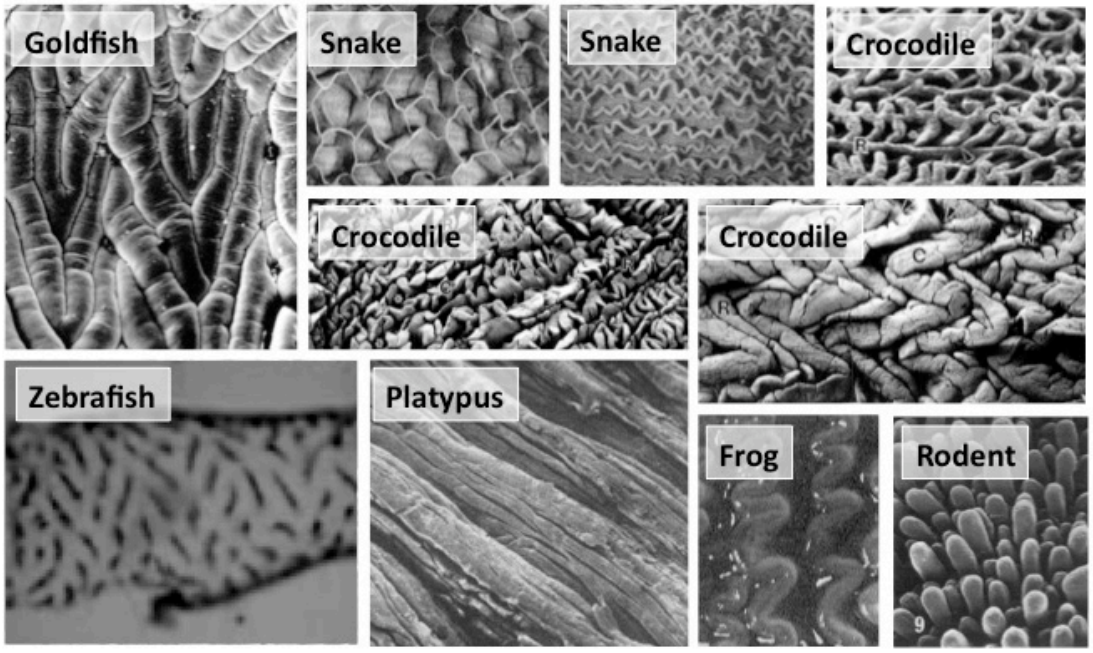

Figure 1.2. Variation in villi pattern across species. Shown are luminal morphologies from a variety of adult species. Note that different shapes provide more or less surface area. Adapted from Krause et al. 1974, Walker et al. 2004, Ferri et al. 1976, Kotze et al. 1995, Wang et al. 2010, McAvoy et al. 1978, Nakamura et al. 1983.

stomach, and liver is asymmetric. Intriguingly, this asymmetry is invariant, with each organ consistently biased to the same side within a species. Thus, the break in symmetry seen in internal organs is not a result of random phenomena or evidence of stochastic fluctuations (Levin et al 2004). Individuals with a condition known as *situs inversus* show complete reversal of the internal organs, but rarely suffer health consequences as a result of this abnormality (Levin et al. 2004). However, cases where some organs show left-right reversal while other organs do not, a condition termed *situs ambiguo*us or heterotaxia, can result in birth defects with serious medical consequence (Burn et al. 1991). Our understanding of the establishment of left-right asymmetry and the underlying causes when this process goes awry has grown dramatically over the past decade through investigation at the molecular and genetic level.

The development of left-right asymmetry can be thought of in four stages: the initial break in symmetry, establishment differential expression patterns around the embryonic organizer termed the node, propagation of this asymmetry to the lateral plate mesoderm, and the transfer of left-right cues to developing organs. Although much of this process is conserved between mouse and chick, the initial steps establishing left-right asymmetry differ between the species. The first asymmetric gene expression in chick is preceded by asymmetric cell rearrangement responsible for a leftward movement of cells around the node (Gros et al. 2009). In mouse, fluid flow caused by the leftward rotation of node cilia is thought to initiate differential gene expression (Nonaka et al. 1998). Starting within the first day of chick development, at HH (Hamburger and Hamilton 1951) stage 5, left-right patterning involves a complex cascade of genes from several classic developmental pathways that show dramatic unilateral expression patterns around

the node (Pagan-Westphal and Tabin et al. 1998). Nodal, a secreted factor and member of the TGFβ family shows early left-sided expression in both mouse and chick in the perinodal region and then later in the lateral plate mesoderm (Levin et al. 1995, Lowe et al. 1996). Pitx2 is directly regulated by Nodal and its expression is maintained during organogenesis, long after Nodal expression retracts. Downstream signaling and regulation of Pitx2 during asymmetric organ morphogenesis, such as during gut and heart development, is well conserved between mouse and chick (Schlueter et al. 2007).

The gut was arguably the first organ to bring about asymmetry in the multicellular organism (Boorman et al. 2002). Additionally, unlike the heart, which undergoes asymmetric growth and shape changes along with looping (Mannet 2000, 2009), the intestine in humans, mouse, and chick remains a single symmetrical tube throughout morphogenesis, allowing for a more straightforward examination of left-right development during the single process of directional coiling. Morphogenesis of the gut is thus a particularly desirable system for the investigation of asymmetric oranogenesis.

In amniotes, the gut forms as the endoderm folds from a sheet to a closed tube and brings with it a layer of splanchnopleural mesoderm, part of the lateral plate mesoderm that will become smooth muscle surrounding the gut (Roberts et al. 2000). During this process, a section of splanchnopleural mesoderm, termed the dorsal mesentery remains attached to the body wall suspending the primitive gut tube in the coelom (Davis et al. 2008). The gut is divided into the foregut, midgut, and hindgut along the anterior-posterior axis. The first break in symmetry in the gut occurs in the midgut region when the gut tube tilts as it forms the first hairpin loop. This loop moves out of the body cavity and undergoes counterclockwise rotation. Later in development, the loops retract back

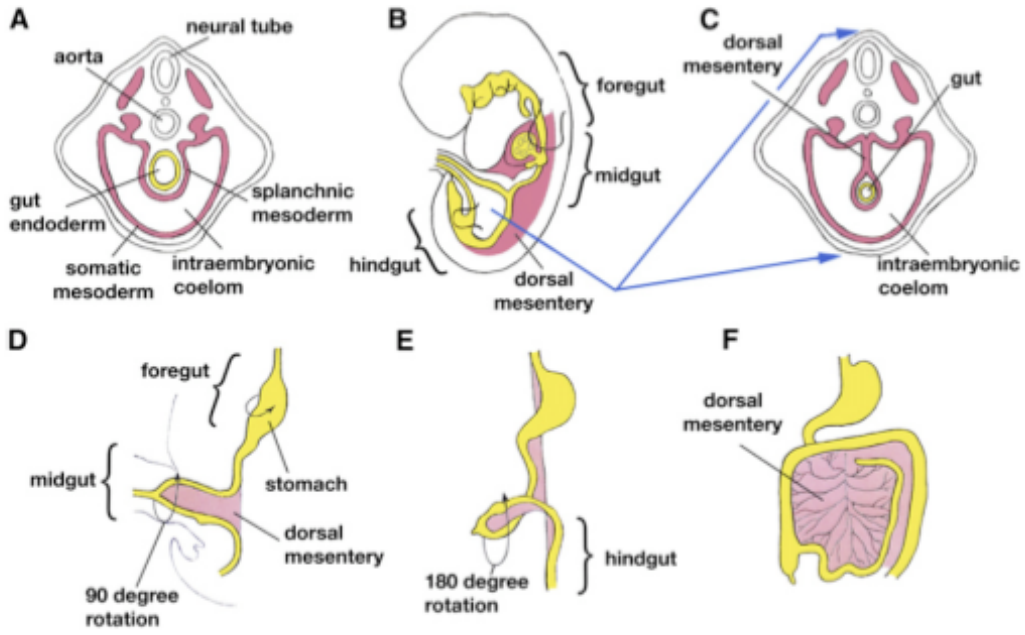

Figure 1.3. The formation and rotation of the gut tube. (A) A Cross-section during gut tube formation with the gut tube (endoderm) shown in yellow, and the mesoderm/mesentery shown in pink (B) Side view of the primitive gut tube. (C) Cross-section of the primitive gut tube, dorsal mesentery will break symmetry with a leftward tilt. (D) Primary intestinal loop moving into the umbilicus (in mammals) or yolk sac (in birds). (E) Gut tube retracting into the body cavity. (F) Final orientation of the midgut, full loop pattern not shown. From Davis et al. 2008.

into the body and continues to rotate counterclockwise until positioned properly with respect to other internal organs (Schematized in Figure 1.3, Davis et al. 2008). Malrotation of the midgut is a condition that often results in volvulus, blockage and loss of blood flow to the intestines, and occurs in about 1 in 500 live births, often with serious medical consequences (Strouse et al. 2004). Thus, it is essential that the first loop always form asymmetrically in the same direction, a process guided by the initial tilt of the midgut dorsal mesentery (Davis et al. 2008).

The midgut tilt forms as a result of differences in gene expression on the left and right sides of the dorsal mesentery, which lead to changes in cellular architecture, such as cell shape and density (Davis et al. 2008). Specifically, Pitx2 and downstream signals direct cells in the left mesenchyme of the mesentery to condense and cells of the right mesentery to adopt a dispersed appearance changing the mesentery shape from a rectangle to a trapezoid in cross section. This relatively small asymmetry tilts the midgut and provides a bias for subsequent gut rotation (Davis et al .2008, Kurpios et al. 2008).

These studies provide an understanding of the process by which asymmetry is established, however, the gut rotation alone is insufficient to pack the entire small intestine into the body cavity, and additional loops are formed as the tube elongates. Although gut looping is seemingly a simpler, and more accessible process than heart looping, there have been virtually no investigations of how loops form in the mammalian or avian gut, however, several studies have investigated heart looping. In fact, these studies have developed mechanical hypotheses for heart loop formation, postulating that membranes around the heart create torsion leading to looping (Taber et al. 1995, 2006,

2010). These investigations of heart looping inspire similar biomechanical studies of looping and morphogenesis in other developing organs.

Intestinal epithelial development, reorganization, and villi initiation

The intestinal epithelium arises from the endoderm, one of the three primary germ layers derived during gastrulation. The endoderm remains an undifferentiated layer of pseudostratified, cuboidal cells throughout the embryonic gut until about mid-gestation when instructive and permissive developmental cues from the neighboring mesenchyme direct pattering of the organ-specific endoderm (Reviewed in Noah et al. 2011). The intestinal epithelium undergoes a transition into columnar cells accompanied by the formation of small outgrowths, first composed of only epithelium, and then encompassing both the epithelium and mesenchyme as they grow out. These outgrowths represent the beginnings of intestinal villi and form in an anterior to posterior wave along the gut (Reviewed in Spense et al. 2011).

Work from the past several decades purports that secondary lumina form within the epithelium and meet the central lumen to form villi, however this hypothesis has not been deeply explored (Reviewed in Noah et al. 2011). Recently, an alternative view of mouse villus formation was put forward; postulating a potential inductive role of the epithelial derived signal Sonic Hedgehog (Shh) in triggering a morphogenetic cascade directing villus outgrowth (Walton et al. 2012). The key results that led in this direction were the failure of villus formation when Shh activity was pharmacologically blocked with the Shh antagonist cyclopamine and the increased size of the villi when guts were provided with excess Shh signal. These results reveal Shh signaling is necessary for villi

initiation, however because Shh directs many cellular processes during radial patterning of the gut, coordinating mesenchymal proliferation and smooth muscle differentiation, it is difficult to interpret the phenotype when Shh signal is perturbed before villi form (Sukegawa et al. 2000, Ramalho-Santos et al. 2000, Mao et al. 2010). Therefore the mechanism underlying villi initiation during intestinal development remain unknown.

Although the mechanisms driving the formation of villi have not been clearly illustrated, several studies from the mid-twentieth century provide careful descriptions of intestinal morphometry and morphology as villi form. Coulombre and Coulombre in 1958 review the striking changes in geometric form that arise as villi develop in the chick, describing the luminal topographies that arise before villi. In most avian species studied, the luminal surface of the intestine is first folded into longitudinal ridges which buckle into zigzags and then give way to true villi (Figure 1.4). Quantitative observations of geometry and growth as villi form in chick date even farther back to the turn of the century (Hilton 1902) and this body of observational work allows for spatial and temporal correlations to be made and testable hypotheses to be put forth.

Early studies of intestinal villi morphogenesis in mouse confirm that rodent villi do not initiate ridge-like folds but rather form direct epithelial elevations from the smooth luminal surface (Sbarbati et al. 1981, Figure 1.4). These studies and others (Burgess 1975) supposed that dynamic growth of the gut tube might contribute to the formation of villi, however these hypotheses have not been further probed in a biological setting.

Epithelial-mesenchymal signaling in the developing villus

Studies of mutant mice with intestinal phenotypes highlight the importance of a

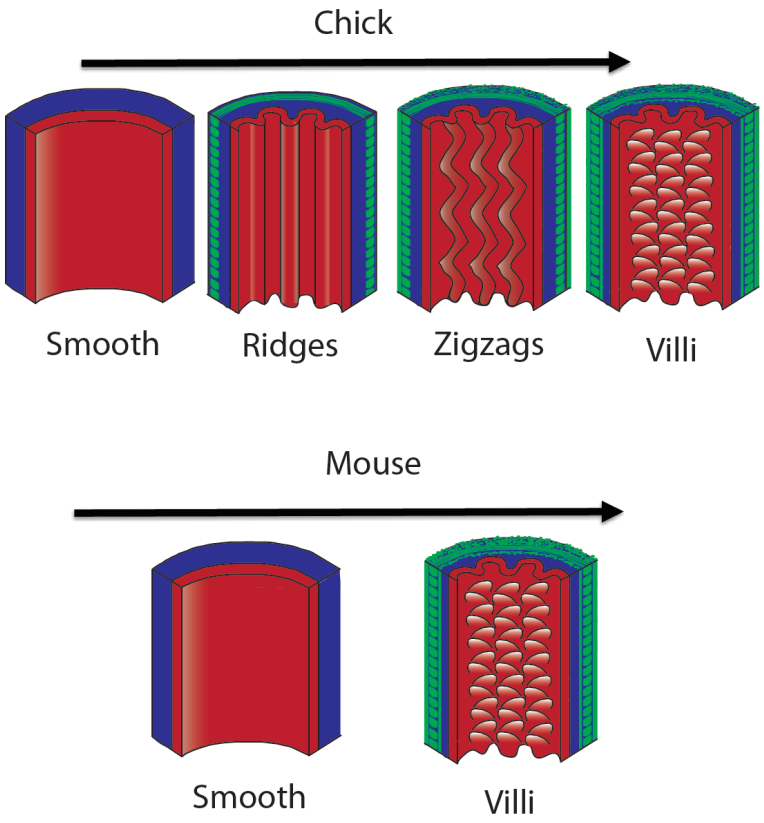

Figure 1.4. Villi formation in chick and mouse. Schematized luminal views of the developing intestine based on observational studies of villi development from the last century. The longitudinal axis on the intestine runs top to bottom. Top, During villi formation in chick, the luminal surface of the intestine is first folded into longitudinal ridges which buckle into zigzags and then give way to true villi. In mouse, ridges and zigzags do not form and villi form directly from a smooth surface. Adapted from Coulobre and Coulombre et al. 1958.

number of key developmental genes in proper villi formation. Bmps in the mesenchyme are downstream of epithelial Shh signal and serve to communicate reciprocally back to the epithelium (Ramalho-Santos et al. 2000). Loss of Foxf1 and Foxf2, transcription factors downstream of Shh and Bmps, results in misshapen villi (Ormestad et al. 2006). Similarly mice lacking either the PDGF-A ligand or the PDGF receptor alpha (PDGFRα) have impaired villi development (Karlsson et al. 2000). Additionally, epithelial Ezrin, involved in linkage between membrane proteins and the cytoskeleton, is necessary for proper villi formation (Saotome et al. 2004).

As villi form, mesenchymal factors Bmp4, PDGFRα, and Foxf1/2 are all expressed specifically in the mesenchyme directly under the growing tip of the villus, a region termed the villus cluster (Karlsson et al. 2000, Ormestad et al. 2006). It has been recently shown that Shh signal from the epithelium is upstream of these mesenchymal expression patterns, however how such a localized pattern expression forms in the mesenchyme as a result of uniform epithelial Shh is not known (Walton et al. 2012). In fact, the function of the villus cluster is still under investigation.

Proliferation, Wnt and the intervillous zone

The cluster does not serve as a zone of proliferation, and in fact is devoid of mitotic cells (Karlsson et al. 2000, Madison et al. 2012). Further, the epithelial cells adjacent to the cluster also lack markers of proliferation, suggesting cluster signals inhibit proliferation. These results are perhaps surprising as one might expect the region near the elongating villus tip to encourage local outgrowth. Instead, as villi form, proliferation transitions from being uniform throughout the epithelium to restricted to the space

between growing villi. (Reviewed in Noah et al. 2011) Proliferation in the adult intestine is directed by canonical Wnt signal, as is the case in many embryonic and adult contexts (Pinto et al. 2003, 2005). Similarly Wnt is important for proliferation in the embryonic epithelium, however its role in the embryonic gut may be more complex (Reviewed in Spense et al. 2011). Still, Tcf4, a main effector of the canonical Wnt pathway is required for proliferation to be maintained in the intervillous region as villi form (Korinek et al. 1998). Additionally, Wnt target genes such as CD44 share an embryonic expression pattern with proliferation, becoming restricted to the region between villi as they form (Kim et al 2007, Madison et al. 2005). Axin2, a reporter of canonical Wnt signal, is expressed in a manner similar to proliferation and CD44 (Jho et al. 2002). However, the localization of β-catenin, a central player in the Wnt pathway may not align with proliferation during gut development, pointing to additional roles for Wnt, outside of proliferation, as villi form (Kim et al 2007).

Intestinal stem cells in the adult and embryo

In the adult intestine, proliferation is restricted to the crypt, the intestinal stem cell niche. Adult intestinal stem cells (ISCs) are long-lived, multipotent cells that serve to replenish the mucosal surface of the intestine during homeostasis (Umar 2010). The discovery of a number of putative ISC markers has aided in our understanding of how ISCs contribute to homeostasis and disease. One such gene, Lgr5 is specifically expressed in the cycling crypt basal cells (CBCs) of the crypt (Barker et al. 2007). Lineage tracing and transplantation studies demonstrating that Lgr5-positive cells are multipotent and long-lived have established Lgr5 as a bone fide intestinal stem cell marker (Barker et al. 2007). Impressively, a single Lgr5-positive cell can form a self-

renewing, long-lived, gut-like organoid in culture (Sato et al. 2009).

As Lgr5 faithfully marks the ISC population, tracing its expression back through embryogenesis could reveal the origin of this cell type, however, only a very limited number of studies have set out to trace ISC markers, such as Lgr5, back to their embryonic origin. Preliminary evidence that ISC markers are not embryonically expressed as well as data supporting embryonic expression has been put forth (Kim et al. 2012, Garcia et al. 2009). The earliest established expression of the ISC marker Lgr5 is found at P0 and just after in the intervillous region before crypts form (Kim et al. 2012, Itzkovitz et al 2012), however, Lgr5 is expressed embryonically in several other tissues (Barker et al. 2012). Additionally, the Lgr5 null mice do display a gastrointestinal phenotype, suggesting the gene may be expressed in the embryonic intestine (Morita et al. 2004).

Summary of thesis

In this dissertation, I first examine the mechanism behind the formation of intestinal loops. I demonstrate that looping morphogenesis is driven by mechanical forces that arise from differential growth between the gut tube and the anchoring dorsal mesenteric sheet. A computational model based on measured parameters not only quantitatively predicts the looping pattern in chick, verifying that these physical forces are sufficient to explain the process, but also accounts for the variation in the gut looping patterns seen in other species.

I then explore the formation of intestinal villi in chick. I find that intestinal villi form in a stepwise process as a result of physical forces generated as proliferating

endodermal and mesenchymal tissues are constrained by sequentially differentiating layers of smooth muscle. A computational model incorporating measured differential growth and the geometric and physical properties of the developing chick gut recapitulates the morphological patterns seen during chick villi formation. I also demonstrate that the same basic biophysical processes underlie the formation of intestinal folds in frog and villi in mice.

Finally, I focus on the process by which intestinal stem cells are ultimately localized to the base of each villus. As the luminal surface of the gut is deformed during villus formation, there are resulting local maxima of Shh response in the mesenchyme. This results, at high threshold, in the induction of a new signaling center under the villus tip termed the villus cluster. This, in turn, feeds back to restrict proliferating progenitors in the endoderm, the presumptive precursors of the stem cells, to the base of each villus. We assay for expression of ISC markers in the embryonic gut and find that embryonic progenitors resemble adult ISCs, suggesting ISCs may be remnants of this pool of embryonic progenitors.

References

Barker, N. *et al*. Lgr5(+ve) stem/progenitor cells contribute to nephron formation during kidney development. *Cell. Rep.* **2**, 540-552 (2012).

Barker, N. *et al*. Identification of stem cells in small intestine and colon by marker gene Lgr5. *Nature* **449**, 1003-1007 (2007).

Beddard, F. E. *The Structure and Classification of Birds.* Longmans, Green, and co. London New York [etc.] (1898).

Behrndt, M. *et al*. Forces driving epithelial spreading in zebrafish gastrulation. *Science* **338**, 257-260 (2012).

Boorman CJ, Shimeld SM. The evolution of left-right asymmetry in chordates. Bioessays 24: 1004–101 (2002).

Burgess, D. R. Morphogenesis of intestinal villi. II. Mechanism of formation of previllous ridges. J. Embryol. Exp. Morph. 34, 723-740 (1975).

Burn, J. Disturbance of morphological laterality in humans. *Ciba Found. Symp.* **162**, 282-96; discussion 296-9 (1991).

A. J. Coulombre, J. L. Coulombre, Intestinal development. I. Morphogenesis of the villi and musculature. *J. Embryol. Exp. Morphol.* **6**, 403-411 (1958).

Davidson, L. A. Epithelial machines that shape the embryo. *Trends Cell Biol.* **22**, 82-87 (2012).

Davidson, L. A. Embryo mechanics: balancing force production with elastic resistance during morphogenesis. *Curr. Top. Dev. Biol.* **95**, 215-241 (2011).

Davis, N. M. *et al*. The chirality of gut rotation derives from left-right asymmetric changes in the architecture of the dorsal mesentery. *Dev. Cell.* **15**, 134-145 (2008).

Drachman, D., and Sokoloff, L. The role of movement in embryonic joint development. Dev. Biol. 14, 401–420 (1966).

Farge, E. Mechanotransduction in development. *Curr. Top. Dev. Biol.* **95**, 243-265 (2011).

Ferri, S., Junqueira, L. C., Medeiros, L. F. & Mederios, L. O. Gross, microscopic and ultrastructural study of the intestinal tube of Xenodon merremii Wagler, 1824 (Ophidia). *J. Anat.* **121**, 291-301 (1976).

Filas, B. A. *et al*. A potential role for differential contractility in early brain development and evolution. *Biomech. Model. Mechanobiol* **11**, 1251-1262 (2012).

Filas, B. A. *et al*. Regional differences in actomyosin contraction shape the primary vesicles in the embryonic chicken brain. *Phys. Biol.* **9**, 066007-3975/9/6/066007. Epub 2012 Nov 16 (2012).

Gros, J., Feistel, K., Viebahn, C., Blum, M. & Tabin, C. J. Cell movements at Hensen's node establish left/right asymmetric gene expression in the chick. *Science* **324**, 941-944 (2009).

W. A. Hilton. The morphology and development of intestinal folds and villi in vertebrates. American Journal of Anatomy 1, 459-505 (1902).

Jho, E. H. *et al*. Wnt/beta-catenin/Tcf signaling induces the transcription of Axin2, a negative regulator of the signaling pathway. *Mol. Cell. Biol.* **22**, 1172-1183 (2002).

Kahn, J. *et al*. Muscle contraction is necessary to maintain joint progenitor cell fate. *Dev. Cell.* **16**, 734-743 (2009).

Karlsson, L., Lindahl, P., Heath, J. K. & Betsholtz, C. Abnormal gastrointestinal development in PDGF-A and PDGFR-(alpha) deficient mice implicates a novel mesenchymal structure with putative instructive properties in villus morphogenesis. *Development* **127**, 3457-3466 (2000).

Kim, B. M., Mao, J., Taketo, M. M. & Shivdasani, R. A. Phases of canonical Wnt signaling during the development of mouse intestinal epithelium. *Gastroenterology* **133**, 529-538 (2007).

Kim, T. H., Escudero, S. & Shivdasani, R. A. Intact function of Lgr5 receptor-expressing intestinal stem cells in the absence of Paneth cells. *Proc. Natl. Acad. Sci. U. S. A.* **109**, 3932-3937 (2012).

Kotze, S. H., Van der Merwe, N. J., Van Aswegen, G. & Smith, G. A. A light microscopical study of the intestinal tract of the Nile crocodile (Crocodylus niloticus, Laurenti 1768). *Onderstepoort J. Vet. Res.* **59**, 249-252 (1992).

Krause, W. J. Ultrastructure of the platypus and echidna mandibular glands. *Anat. Histol. Embryol.* **40**, 352-359 (2011).

Levin, M. Left-right asymmetry in embryonic development: a comprehensive review. *Mech. Dev.* **122**, 3-25 (2005).

Levin, M. The embryonic origins of left-right asymmetry. *Crit. Rev. Oral Biol. Med.* **15**, 197-206 (2004).

Levin, M. Left-right asymmetry and the chick embryo. *Semin. Cell Dev. Biol.* **9**, 67-76 (1998).

Logan, M., Pagan-Westphal, S. M., Smith, D. M., Paganessi, L. & Tabin, C. J. The transcription factor Pitx2 mediates situs-specific morphogenesis in response to left-right asymmetric signals. *Cell* **94**, 307-317 (1998).

Lowe, L. A. *et al*. Conserved left-right asymmetry of nodal expression and alterations in murine situs inversus. *Nature* **381**, 158-161 (1996).

Madison, B. B. *et al*. Epithelial hedgehog signals pattern the intestinal crypt-villus axis. *Development* **132**, 279-289 (2005).

Manner, J. The anatomy of cardiac looping: a step towards the understanding of the morphogenesis of several forms of congenital cardiac malformations. *Clin. Anat.* **22**, 21-35 (2009).

Manner, J. Cardiac looping in the chick embryo: a morphological review with special reference to terminological and biomechanical aspects of the looping process. *Anat. Rec.* **259**, 248-262 (2000).

Mao, J., Kim, B. M., Rajurkar, M., Shivdasani, R. A. & McMahon, A. P. Hedgehog signaling controls mesenchymal growth in the developing mammalian digestive tract. *Development* **137**, 1721-1729 (2010).

McAvoy, J. W. & Dixon, K. E. Cell specialization in the small intestinal epithelium of adult Xenopus laevis: structural aspects. *J. Anat.* **125**, 155-169 (1978).

Mitchell, C. P. On the intestinal tract of birds. *Proc. Zool. Soc. London* **64**, 136-159 (1896).

Morita, H. *et al*. Neonatal lethality of LGR5 null mice is associated with ankyloglossia and gastrointestinal distension. *Mol. Cell. Biol.* **24**, 9736-9743 (2004).

Nakamura, K. & Komuro, T. A three-dimensional study of the embryonic development and postnatal maturation of rat duodenal villi. *J. Electron. Microsc. (Tokyo)* **32**, 338-347 (1983).

Noah, T. K., Donahue, B. & Shroyer, N. F. Intestinal development and differentiation. *Exp. Cell Res.* **317**, 2702-2710 (2011).

Nonaka, S. *et al*. Randomization of left-right asymmetry due to loss of nodal cilia generating leftward flow of extraembryonic fluid in mice lacking KIF3B motor protein. *Cell* **95**, 829-837 (1998).

Ormestad, M. *et al*. Foxf1 and Foxf2 control murine gut development by limiting mesenchymal Wnt signaling and promoting extracellular matrix production. *Development* **133**, 833-843 (2006).

Pagan-Westphal, S. M. & Tabin, C. J. The transfer of left-right positional information during chick embryogenesis. *Cell* **93**, 25-35 (1998).

Pinto, D. & Clevers, H. Wnt, stem cells and cancer in the intestine. *Biol. Cell.* **97**, 185-196 (2005).

Pinto, D. & Clevers, H. Wnt control of stem cells and differentiation in the intestinal epithelium. *Exp. Cell Res.* **306**, 357-363 (2005).

Pinto, D., Gregorieff, A., Begthel, H. & Clevers, H. Canonical Wnt signals are essential for homeostasis of the intestinal epithelium. *Genes Dev.* **17**, 1709-1713 (2003).

Ramalho-Santos, M., Melton, D. A. & McMahon, A. P. Hedgehog signals regulate multiple aspects of gastrointestinal development. *Development* **127**, 2763-2772 (2000).

Saotome, I., Curto, M. & McClatchey, A. I. Ezrin is essential for epithelial organization and villus morphogenesis in the developing intestine. *Dev. Cell.* **6**, 855-864 (2004).

Sato, T. *et al*. Single Lgr5 stem cells build crypt-villus structures in vitro without a mesenchymal niche. *Nature* **459**, 262-265 (2009).

Sbarbati, R. Morphogenesis of the intestinal villi of the mouse embryo: chance and spatial necessity. *J. Anat.* **135**, 477-499 (1982).

Schlueter, J. & Brand, T. Left-right axis development: examples of similar and divergent strategies to generate asymmetric morphogenesis in chick and mouse embryos. *Cytogenet. Genome Res.* **117**, 256-267 (2007).

Spence, J. R., Lauf, R. & Shroyer, N. F. Vertebrate intestinal endoderm development. *Dev. Dyn.* **240**, 501-520 (2011).

Strouse, P. J. Disorders of intestinal rotation and fixation ("malrotation"). *Pediatr. Radiol.* **34**, 837-851 (2004).

Sukegawa, A. *et al*. The concentric structure of the developing gut is regulated by Sonic hedgehog derived from endodermal epithelium. *Development* **127**, 1971-1980 (2000).

Taber, L. A. Biophysical mechanisms of cardiac looping. *Int. J. Dev. Biol.* **50**, 323-332 (2006).

Taber, L. A., Lin, I. E. & Clark, E. B. Mechanics of cardiac looping. *Dev. Dyn.* **203**, 42-50 (1995).

Taber, L. A., Voronov, D. A. & Ramasubramanian, A. The role of mechanical forces in the torsional component of cardiac looping. *Ann. N. Y. Acad. Sci.* **1188**, 103-110 (2010).

Thompson, D. W. *On Growth and Form.* Cambridge University Press, Cambridge (1917).

Umar, S. Intestinal stem cells. *Curr. Gastroenterol. Rep.* **12**, 340-348 (2010).

R.L. Walker, A.G. Buret, C.L. Jackson, K.G.-E. Scott, R. Bajwa, and H.R. Habibi, Effects of growth hormone on leucine absorption, intestinal morphology, and ultrastructure of the goldfish intestine. Can. J. Physiol. Pharmacol. **82**: 951–959 (2004)

Walton, K. D. *et al*. Hedgehog-responsive mesenchymal clusters direct patterning and emergence of intestinal villi. *Proc. Natl. Acad. Sci. U. S. A.* **109**, 15817-15822 (2012).

Wang, Z. *et al*. Morphological and molecular evidence for functional organization along the rostrocaudal axis of the adult zebrafish intestine. *BMC Genomics* **11**, 392-2164-11-392 (2010).

Yasuda, H. & de Crombrugghe, B. Joint formation requires muscle formation and contraction. *Dev. Cell.* **16**, 625-626 (2009).

Chapter Two

On the Growth and Form of the Gut

On the Growth and Form of the Gut

Thierry Savin,[1*] Natasza A. Kurpios,[2*], Amy E.Shyer,[2*] Patricia Florescu,[1] Haiyi Liang,[1], L. Mahadevan[1,3,4,5,6] and Clifford J. Tabin[2]

[1] *School of Engineering and Applied Sciences, Harvard University, Cambridge MA 02138*

[2] *Department of Genetics, Harvard Medical School, Boston MA 02115*

Boston, MA 02115

[3] *Department of Organismic and Evolutionary Biology, Harvard University, Cambridge MA 02138*

[4] *Department of Physics, Harvard University, Cambridge, MA 02138*

[5] *Wyss Institute for Biologically Inspired Engineering, Harvard University, Cambridge MA 02138*

[6] *Kavli Institute for Nanobio Science and Technology, Harvard University, Cambridge MA 02138*

**These authors contributed equally to this work*

This chapter contains the manuscript titled "On the Growth and Form of the Gut", originally published in Nature, August 4, 2011; 476(7358):57-62. It is modified to better fit the style of this dissertation. A. E. Shyer was co-first author on this manuscript. C.J.T., N.A.K. and L.M. designed the project with additional contributions from T.S. and A.E.S.; T.S. (biophysical and computational experiments, data analysis), N.A.K. (biological experiments), A.E.S. (biological and biophysical experiments) and L.M. (physical mechanism, physical/mathematical model, scaling theory) did the research; P.F. (stitched physical model) and H.L. (built computational model) contributed tools; and T.S., N.A.K., L.M. and C.J.T. wrote the paper.

Summary

The developing vertebrate gut tube forms a reproducible looped pattern as it grows into the body cavity. Here we use developmental experiments to eliminate alternative models and show that gut looping morphogenesis is driven by the homogeneous and isotropic forces that arise from the relative growth between the gut tube and the anchoring dorsal mesenteric sheet, tissues that grow at different rates. A simple physical mimic, using a differentially strained composite of a pliable rubber tube and a soft latex sheet is consistent with this mechanism and produces similar patterns. We devise a mathematical theory and a computational model for the number, size and shape of intestinal loops based solely on the measurable geometry, elasticity and relative growth of the tissues. The predictions of our theory are quantitatively consistent with observations of intestinal loops at different stages of development in the chick embryo. Our model also accounts for the qualitative and quantitative variation in the distinct gut looping patterns seen in a variety of species including the quail, finch and mouse illuminating how the simple macroscopic mechanics of differential growth drives the morphology of the developing gut.

Introduction

Understanding morphogenesis, the origin of shape in anatomical structures, organs, and organisms, has been a central goal of developmental biology since its origins. Historically, the subject focused on the morphology and dynamics of embryonic growth[1] with many analogies to observable physical phenomena. This metaphoric approach to

biological shape is epitomized in D'Arcy Thompson's *On Growth and Form*[2], with its focus on a mathematical and physical approach to the subject, emphasizing the role of differential growth in determining form. However, with the modern revolution in molecular biology, the field focused on a framework built around gene regulation, signaling molecules and transcription factors. This has led to much insight into the logic of the developmental networks controlling processes as diverse as the patterning of the limb skeleton[3] and the branching morphogenesis of the lung[4]. More recently, however, there has been a renewed appreciation for the fact that to understand morphogenesis in three dimensions, one must combine the molecular insights (genes and morphogens) with the knowledge of physical processes (transport, deformation and flow) generated by growing tissues.

In this context, there has been only recent, limited exploration of the role of tissue-scale mechanical forces in organogenesis[5-10]. Such large-scale forces can become important when the shape of an organ is remodeled after its initial structure has been formed. An important example of this hierarchy is the looping morphogenesis of the gut[11]. The midgut forms as a simple linear tube of circular cross-section running down the midline of the embryo, and grows at a faster rate than the surrounding tissue to eventually become significantly longer than the trunk. As the size of the developing mid- and hindgut exceeds the capacity of the embryonic body cavity, a primary loop is forced ventrally into the umbilicus (in mammals) or yolk stalk (in birds). This loop first rotates by 90^0 counterclockwise, followed by another 180^0 during the subsequent retraction into the body cavity. Eventually, the rostral half of the loop forms the midgut (small intestine) while the caudal half forms the upper half of the hindgut (the ascending colon).

The chirality of this gut rotation is directed by left-right asymmetries in cellular architecture that arise within the dorsal mesentery[12-14], an initially thick and short structure along the dorsal-ventral axis through which the tube is attached to the abdominal wall. This leads the mesentery to tilt the gut tube leftward with a resulting counterclockwise corkscrewing of the gut as it herniates[12-13]. However, the gut rotation is insufficient to pack the entire small intestine into the body cavity, and additional loops are formed as the intestine bends and twists even as it elongates. Once the gut attains its final form, which is highly stereotypical in a given species, the loops retract into the body cavity. During further growth of the juvenile, no additional loops are formed[15] as they are tacked down by fascia, which restrict movement and additional morphogenesis without inhibiting globally uniform growth.

Results

Relative growth between gut and attached mesentery drives looping

Throughout development, the gut tube remains attached to the body wall along its entire length by the dorsal mesentery, and is fixed at both its rostral and caudal ends to the mouth and anus, respectively, and thus preserves its connectivity and chirality during growth. The resulting number, shape and size of loops are also conserved in any given species, as shown in Figure 2.1a at embryonic day 16 (E16) for the chick.

In principle, this regularity of looping could result from either the intrinsic properties of the gut tube and mesentery, or from external spatial packing constraints. However, surgical dissection of the gut and mesentery from the rest of the embryonic tissues shows that all the loops remain intact and identical to their *in ovo* structure at

various stages of development (Figure 2.1a), ruling out any role for body-cavity-induced constraints. Another possible mechanism for the reproducible looping is an increased asymmetric proliferation of cells in the gut tube at the location of the bends. To test this we counted the numbers of mitotic cells in the entire midgut section during the formation of the first loop at E5 (Figure 2.1b) and later when there were 9 loops (E12) (Figure 2.1b). We observed consistently uniform proliferation with no significant differences along the rostro-caudal axis of the gut tube, including at loop formation locations, and in between loops, as well as no observable azimuthal or radial differences in proliferation rates at different cross-sections (Appendix I), consistent with observations that the embryonic gut tube cross-section remains circular along its length.

Since spatial constraints from the body cavity and the gut tube alone cannot explain the reproducible looping, we turned to the dorsal mesentery, the webbed tissue that attaches the gut tube to the embryo throughout its length. As looping morphogenesis is initiated, the dorsal mesentery changes from a thick, asymmetric multilayer structure to a thin double-epithelial sheet with no observable left-right asymmetry (Appendix I).

To test whether the dorsal mesentery is integral to the intestinal loops, we separated it from the gut surgically or enzymatically and find that the intestine uncoils into a straight tube, indicating that it was under compression. Simultaneously, the unconstrained dorsal mesentery when freed from the gut tube contracts (Figure 2.1c), indicating that this tissue is under tension. Thus the mesentery-gut composite is required to maintain the mature loops in the gut.

Figure 2.1. Morphology of loops in the chick gut. **a,** Chick gut at day 5 (E5), E8, E12, E16 shows stereotypical looping pattern. **b,** Proliferation in the E5 (left) and E12 (right) gut tube (above in blue) and mesentery (below in red). Each blue bar represents the average number of phospho-H3 positive cells per unit surface in 40 (E5) or 50 (E12) 10mm sections. For the mesentery, each red bar represents the average number of phospho-H3 positive cells per unit surface over 6 10mm sections (E5), or in specific regions demarcated by vasculature along the mesentery (E12). The inset images of the chick guts align the proliferation data with the location of loops (all measurements were done in 3 or more chick samples). **c,** The gut and mesentery before and after surgical separation at E14 show that the mesentery shrinks while the gut tube straightens out almost completely. **d,** The E12 chicken gut under normal development (left) and after *in ovo* surgical separation of the mesentery at E4 (right). Note the gut and mesentery repair their attachment, leading to some regions of normal looping (highlighted in green). However a portion of the gut lacks normal loops as a result of disrupting the gut-mesentery interaction over the time these loops would have otherwise developed.

Figure 2.1 (Continued)

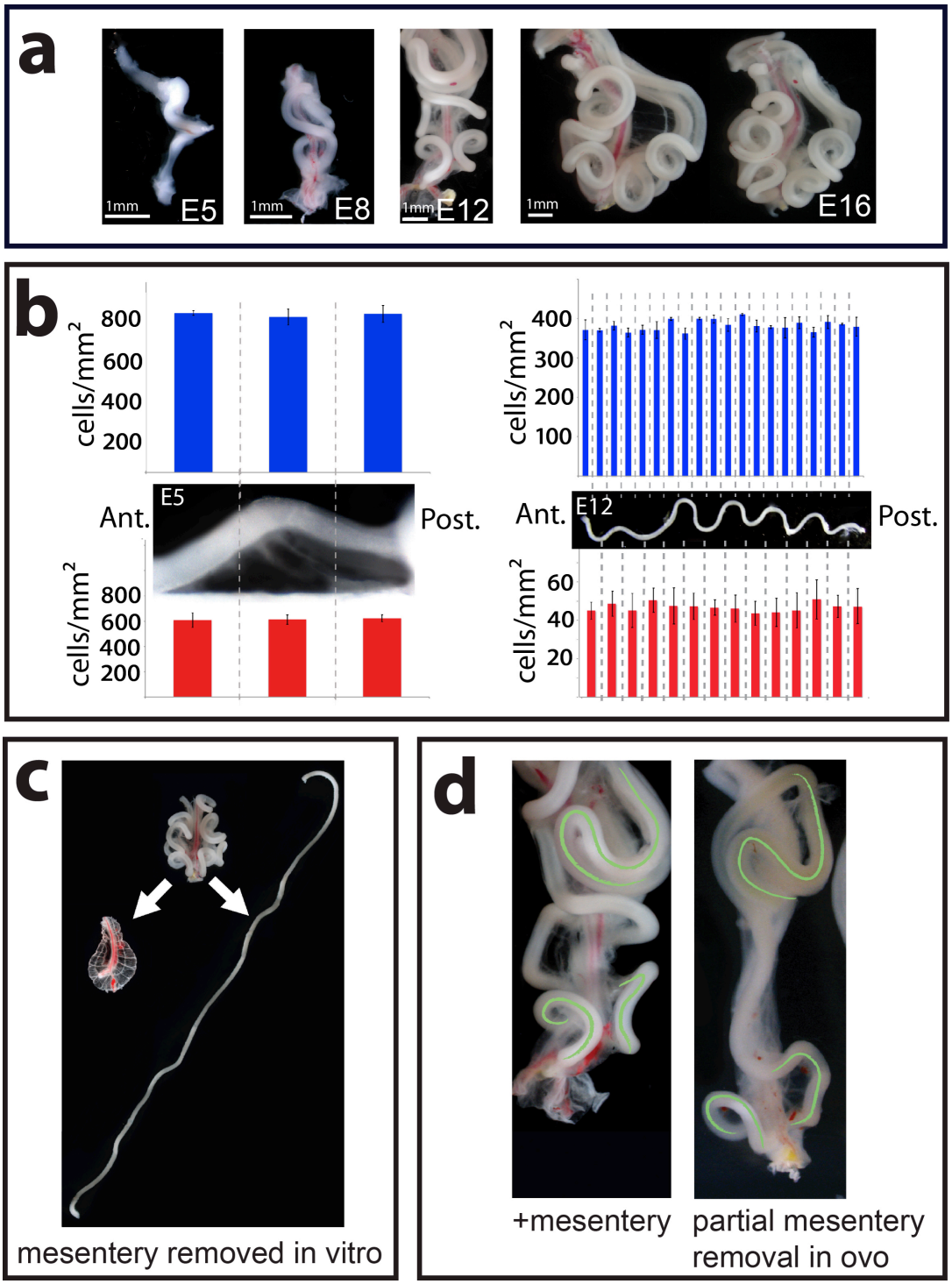

To find out if the dorsal mesentery is also required for the formation of the loops, we surgically separated a portion of the dorsal mesentery from the gut *in ovo,* beginning immediately caudal to the cranial (superior) mesenteric artery (SMA), at day E4, prior to looping. Strikingly, where the mesentery and gut were separated, the intestinal loops fail to form (Figure 2.1d) even as normal loops form in locations rostral and caudal to it (green lines, Figure 2.1d). Although we were unable to cut the dorsal SMA *in ovo* during gut loop development, once the loops had matured (E12), surgical dissection of the SMA leaves the loops intact and in fact highlights their periodic structure (Figure 2.1c). This rules out any possible requirement for the SMA in directing loop structure, and for the vasculature as well, since secondary vessels develop only after the loops themselves have formed.

Although the gut grows uniformly, to investigate if the mesentery might grow inhomogeneously and thus force the gut to loop at precise locations, analogous to a master puppeteer, we examined the proliferation rate of the mesentery at E5 and at E12. There were no observed differences along the rostro-caudal axis (Figure 2.1b), suggesting that the growing mesentery exerts a uniform compression along the length of the gut, countered by an equal and opposite tensile reaction on it from the gut.

Taken together, our observations suggest that uniform differential growth between the gut and the mesentery could be at the origin of loop formation. Since the gut tube is slender, with a length that is much larger than its radius, it responds physically to the differential strain-induced compression from the attached mesentery by bending and

looping, while remaining attached to the embryo rostro-caudally. Most importantly, the fact that the gut relaxes to a straight configuration while the mesentery relaxes to an almost flat configuration implies that the tissues behave elastically, a fact that will allow us to quantify the process simply.

A physical model of gut looping

To investigate the physical origins of this looping pattern, we developed a simple simulacrum of the gut-mesentery composite using a silicone rubber tube and a thin latex sheet (see Appendix I). The differential strain induced by relative growth between the gut and the mesentery is simulated by extending the latex sheet (the mesentery) along its length, and stitching it to the wall of the naturally straight, unstretched rubber tube (the gut) along the edge parallel to the direction of membrane stretching (Figure 2.2a). Upon removing all external loads from the composite system, we observe the spontaneous formation of loops in the tube very similar in shape to the looping patterns seen *in ovo* (Figure 2.2b). Varying the differential strain, the thickness of the latex sheet, the radius of the rubber tube and their material properties (Supplementary Information) shows that the wavelength and amplitude of the repeating loops depends only on these measurable parameters.

Scaling laws for loop period, radius and number

We now quantify the simple physical picture for looping sketched above to derive expressions for the size of a loop characterized by the contour length l and mean radius of curvature *R* of a single period (see Figure 2.3a). The geometry of the growing gut is characterized by its inner and outer radii r_i and r_o, much smaller than its evolving length,

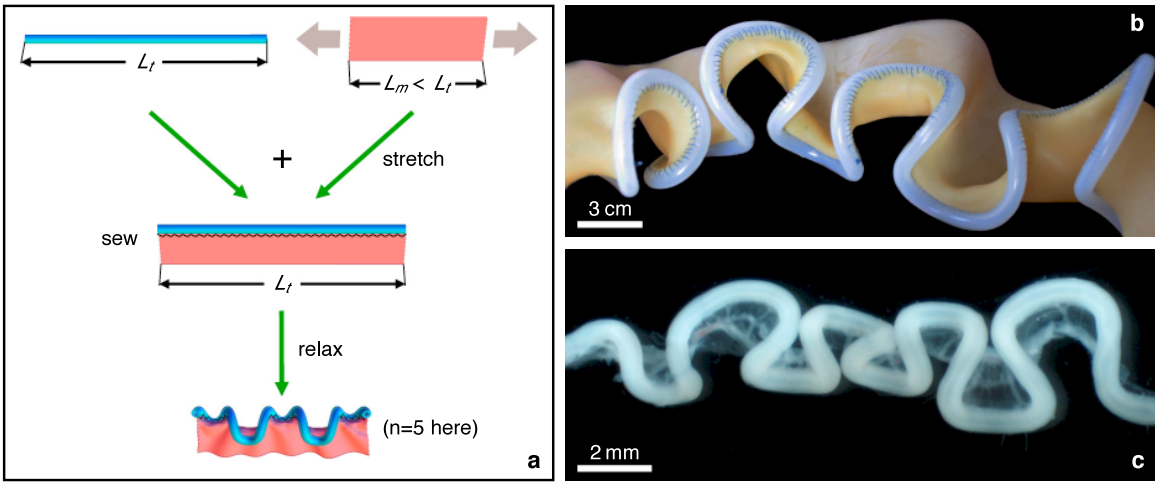

Figure 2.2 Rubber simulacrum of gut looping morphogenesis. **a**, To construct the rubber model of looping, a thin rubber sheet (mesentery) is stretched uniformly along its length and then stitched to a straight unstretched rubber tube (gut) along its boundary; the differential strain mimics the differential growth of the two tissues. The system is then allowed to relax, free of any external forces. **b**, On relaxation, the composite rubber model deforms into a structure very similar to the chick gut (here, the thickness of the sheet is 1.3mm and its Young's modulus is 1.3MPa, the radius of the tube is 4.8mm its thickness is 2.4mm, and its Young's modulus is 1.1MPa, see Supplementary Information for details). **c**, Chick gut at E12. The superior mesenteric artery has been cut out (but not the mesentery), allowing the gut to be displayed aligned without altering its loop pattern.

while that of the mesentery is described by its homogeneous thickness *h,* which is much smaller than its other two dimensions. Since the tube and mesentery relax to nearly straight flat states once surgically separated, we can model the gut as a one-dimensional elastic filament growing relative to a thin two-dimensional elastic sheet (mesentery). As the gut length becomes longer than the perimeter of the mesentery to which it is attached, there is a differential strain ε that compresses the tube axially while extending the periphery of the sheet. When the growth strain is larger than a critical value ε_*, the tube buckles out of the line to take on a wavy shape of characteristic amplitude A and period $\lambda \gg A$. At the onset of buckling, the extensional strain energy of the sheet $U_m \propto E_m \varepsilon_*^2 h \lambda^2$, where E_m is the Young's modulus of the mesentery. The bending energy of the tube $U_t \propto E_t I_t \kappa^2 \lambda$ where $\kappa \propto A / \lambda^2$ is the tube curvature, $I_t \propto r_o^4 - r_i^4$ is the moment of inertia of the tube, and E_t is the Young's modulus of the gut tube. Using the condition that the in-plane strain in the sheet $\varepsilon_* \propto A / \lambda$ and minimizing the sum of the two energies with respect to λ then yields a scaling law for the wavelength of the loop

$$\lambda \propto \left(\frac{E_t I_t}{E_m h}\right)^{1/3} \qquad (1)$$

The above theory is valid only at the onset of looping and cannot predict the amplitude or radius of a loop. Far from the onset of the instability, at a strain $\varepsilon = \varepsilon_o \gg \varepsilon_*$, we use a torque balance argument to determine the finite radius of the loop. To deform the gut into a loop of radius *R,* the elastic torque required is $T_t \propto E_t I_t / R$ and must balance the torque exerted by the membrane with strain ε_o over a width w and length R, $T_m \propto E_m h w \varepsilon_o R$.

The width of this strip is the radial distance from the tube over which the peripheral membrane stretching strain is relaxed, and determined by the relation $\varepsilon_o \propto w/(R\text{-}w)$. Writing $T_t \propto T_m$ and assuming $\varepsilon_0 < 1$ yields the scaling law

$$R \propto \left(\frac{E_t I_t}{E_m h \varepsilon_0^2}\right)^{1/3} \tag{2}$$

Quantitative geometry and biomechanics of chick gut looping

A comparison of the results of our predictions with quantitative experiments requires the measurement of the geometry of the tissues, their elastic properties and the relative strain mismatch at different stages of chick gut development; we chose three stages E8, E12, and E16 (Figure 2.3). The mesentery has a time-varying thickness *h*, which is evaluated from histological cross-section (Appendix I), while the inner/outer radii of the gut tube were extracted from DAPI-stained tube cross-sections (Figure 2.3b and insets). The length of the gut tube L_t was measured on the dissected gut. The natural rest length of the periphery of mesentery L_m was measured by cutting out thin strips along the junction with the gut and aligning them unstretched with a ruler (Figure 2.3c). The bending stiffness of the gut tube and the stretching stiffness of the mesentery was measured using *in vitro* uniaxial low-rate tensile tests, where the load was generated by a magnet applying a calibrated force on a millimeter size steel ball, attached on one end of a tissue sample which was pinned at the other end. The extension of the sample under load was tracked using videomicroscopy to extract its stress *s* vs. strain *e* response curve (see insets of Figure 2.3d,e and Methods/Appendix I).

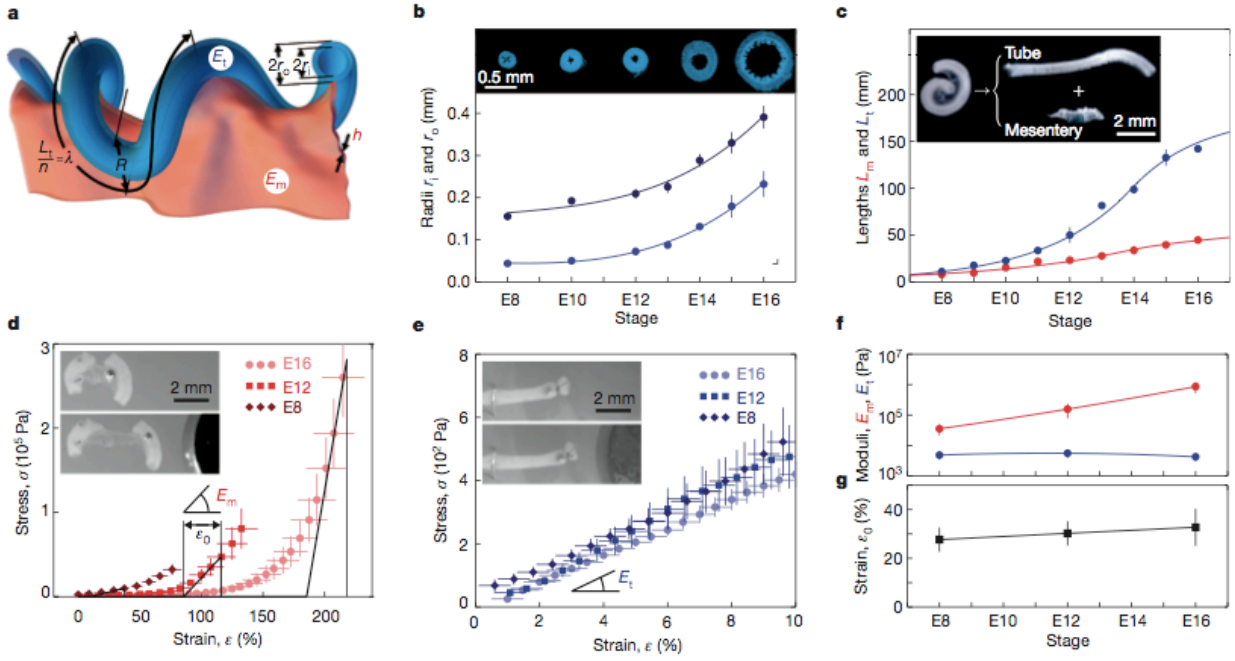

Figure 2.3. Geometric and mechanical measurements of chick gut. a, Schematic summarizing the parameters involved in the physical model. **b**, inner and outer tube diameter. Measurements are extracted from DAPI stained tube cross section shown in insets. **c**, Tube and mesentery differential growth. Inset shows the length measurement on one isolated loop. **d**, Stress vs. extension for the mesentery at E8, E12 and E16. The curves are linearized at a characteristic strain corresponding to the physiological strain, as shown by the black lines, to extract the effective Young modulus E_m and the effective strain e_0. **e**, Stress vs. strain curves for the gut tube at E8, E12 and E16. **f**, Mesentery and tube Young's modulii E_m, E_t as a function of time, E8, E12, E16. **g**, effective differential growth strain ε_0 as a function of time, E8, E12, E16.

For the mesentery, we observe a non-linear response curve with a sharp break at a strain $\varepsilon \le \varepsilon_p$, where $e_p=L_t/L_m-1$ is the physiological strain mismatch, typical of the strain-stiffening seen in biological soft tissues[16]. We define an effective modulus E_m and strain ε_o by locally linearizing the response (see Fig. 3d): $E_m = (\frac{d\sigma}{d\varepsilon})_{\varepsilon=\varepsilon_p}$ and $\varepsilon_0 = (\frac{1}{\sigma}\frac{d\sigma}{d\varepsilon})^{-1}_{\varepsilon=\varepsilon_p}$, noting that the membrane has negligible stiffness when $0 < \varepsilon < \varepsilon_p - \varepsilon_0$. For the gut, we measured the modulus $E_t=s/e$ from the linear low-strain response curve (ε *<10%,* Fig. 3e). In Fig. 3f,g we summarize the variation of E_m, E_t, and ε_o as a function of developmental time. Measurements of the mesentery stiffness at various locations and in various directions did not exhibit significant differences (Appendix I). This indeed allows us to model the mesentery and the gut as isotropic, homogeneous material.

The measured biophysical parameters allowed us to create a detailed numerical simulation of gut looping. Since the gut and mesentery grow slowly, inertial forces are unimportant, and the composite system is always in mechanical equilibrium. This configuration was calculated as follows: the mesentery was modeled as a discrete elastic membrane consisting of a hexagonal lattice of springs with a discrete energy associated with in-plane stretching/shearing deformations as well as out-of-plane bending deformations[17], relative to the rest length of the springs. The gut was modeled as an equivalent membrane strip (that is two elements wide) with a discretized energy associated with bending and stretching deformations, and elastic stiffnesses different from those of the membrane . The geometry, mechanical properties and relative growth of the tissues parameterized by $h, I_t, E_m, E_t, \varepsilon_0$ are all experimentally measured at different time points during development. Given these input parameters, energy

minimization for different relative growth strains ε_0 yields predictions for the looping morphology of the gut (see Methods, Appendix I).

In Figure 2.4a, we compare the results of our observation at E16 with numerical simulations, and in Figure 2.4b,c we compare our quantitative measurements of the wavelength and radius of curvature of the chick gut at the different measured stages of development (see also Appendix I) with those of both the rubber simulacrum and numerical simulations, as a function of the geometry and elastic moduli of the tube and sheet. Over the range of strain $\varepsilon_0 \in [0,1]$ in the simulation and $\varepsilon_0 \in [0.5,1]$ for the various rubber models, we plot the wavelength λ and radius *R* of the loop in Fig. 4b,c, and find that they follow the relations

$$\lambda \simeq 36\left(\frac{E_t I_t}{E_m h}\right)^{1/3} \text{ and } R \simeq 4\left(\frac{E_t I_t}{E_m h \varepsilon_0^2}\right)^{1/3} \qquad (3)$$

in accord with the our simple scaling laws (1)- (2). Table 2.1 compares the values of these parameters for the chick gut with the expressions given in (3), and confirms that our model strikingly captures the salient properties of the looping patterns with no adjustable parameters, strongly suggesting that the main features of the chick gut looping pattern are established by the simple balance of forces induced by the relative growth between the gut and the mesentery.

Comparative study of gut looping across species

To test our theory beyond the development of the chick gut, we took advantage of the distinct gut looping patterns observed in different avian taxa, which have served as

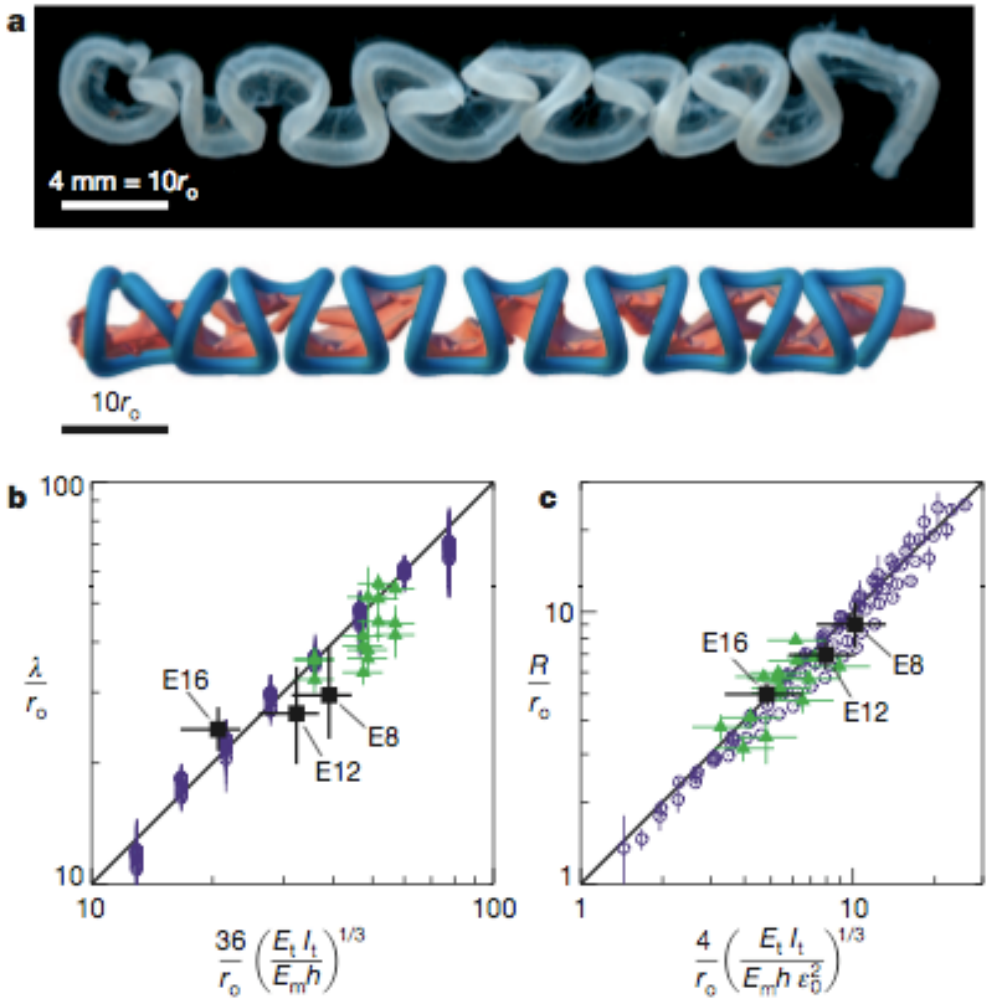

Figure 2.4. Predictions for loop shape, size and number at 3 stages in chick gut development. **a**, Comparisons of the chicken gut E16 (top) with its simulated counterpart (bottom). **b**, Scaled loop contour length *l*/*r*0 plotted vs. eq. (3a) for the chick gut (black squares), the rubber model (green triangles), and numerical simulations (purple circles), are consistent with the scaling law (1). **c,** Scaled loop radius *R*/*r*0, plotted vs. eq. (3b), for the chick gut, the rubber model, and numerical simulations, are consistent with the scaling law (2). Symbols are as in **b**.

Table 2.1

Chicken		n	λ (mm)	R (mm)
E8	Experimental observation	2.4 ± 0.4	4.6 ± 1.0	1.4 ± 0.2
	Computational model*	1.8 ± 0.3	6.1 ± 1.5	1.6 ± 0.3
E12	Experimental observation	9.0 ± 0.5	5.6 ± 1.2	1.5 ± 0.1
	Computational model†	7.3 ± 1.6	6.8 ± 1.6	1.7 ± 0.3
E16	Experimental observation	15.0 ± 0.5	9.5 ± 0.5	1.9 ± 0.1
	Computational model‡	17.5 ± 2.4	8.1 ± 1.9	1.9 ± 0.5

* L_t = 11.0±0.5 mm, h = 13.0±1.5 μm, r_o = 155±8 μm, r_i = 44±5 μm, E_m = 35±14 kPa, E_t = 4.8±1.4 kPa, ε_p = 38±7 %, and ε_0 = 28±5 %.

† L_t = 50.0±8.3 mm, h = 8.0±1.5 μm, r_o = 209±12 μm, r_i = 72±9 μm, E_m = 156±78 kPa, E_t = 5.6±1.7 kPa, ε_p = 116±19 %, and ε_0 = 30±5 %.

‡ L_t = 142.1±3.3 mm, h = 7.1±1.4 μm, r_o = 391±27 μm, r_i = 232±31 μm, E_m = 861±344 kPa, E_t = 4.2±1.3 kPa, ε_p = 218±15 %, and ε_0 = 33±8 %.

Table 2.1. Summary of the observed number of loops, loop wavelength and radius for the chick for different stages of gut development and given geometrical and physical parameters associated with the gut and the mesentery show that the model predictions are quantitatively consistent with observations.

criteria for phylogenetic classification, and are thought of as having adaptive significance, independent of bird size.

We compared the gut looping patterns of the chick with the closely related (but differently sized) quail and that of a songbird, the zebra finch. In Figure 2.5a, we see that, as previously described[18,19] the gut of the chick and quail are organized almost identically but on different scales, while the digestive tracts of songbirds and chickens are markedly different. To make the comparison quantitative, we repeated the morphometric and mechanical measurements (Appendix I) and used these to generate predictions from our scaling theory and computational model. In all cases, the predicted values of λ, R and n are again in excellent agreement with those observed in embryonic guts of the appropriate species (Figure 2.5b,c, Table 2.2). For instance, we find that, although growth strains e_p are similar between the chick and quail, the quail mesentery has a tension $E_m h\varepsilon_0$ approximately five times that in the chick mesentery. Qualitatively, this greater elastic force produces a smaller loop, hence inducing more loops per length and thus the same number of loops in the smaller bird. In contrast, most of the geometrical and physical parameters characterizing the developing gut and mesentery in the chick and zebra finch are different and lead to different looping parameters.

Finally, to challenge our theoretical model with a non-avian example, we performed a similar set of measurements throughout the course of gut development in mouse embryos. In agreement with our findings from birds, the geometrical and biophysical properties of the developing gut and dorsal mesentery suffice to accurately predict the stereotypical patterns of the mature intestinal loops in mouse embryos (Figure 2.5, Table 2.2). The latter are notably characterized by softer tissues and higher mismatch

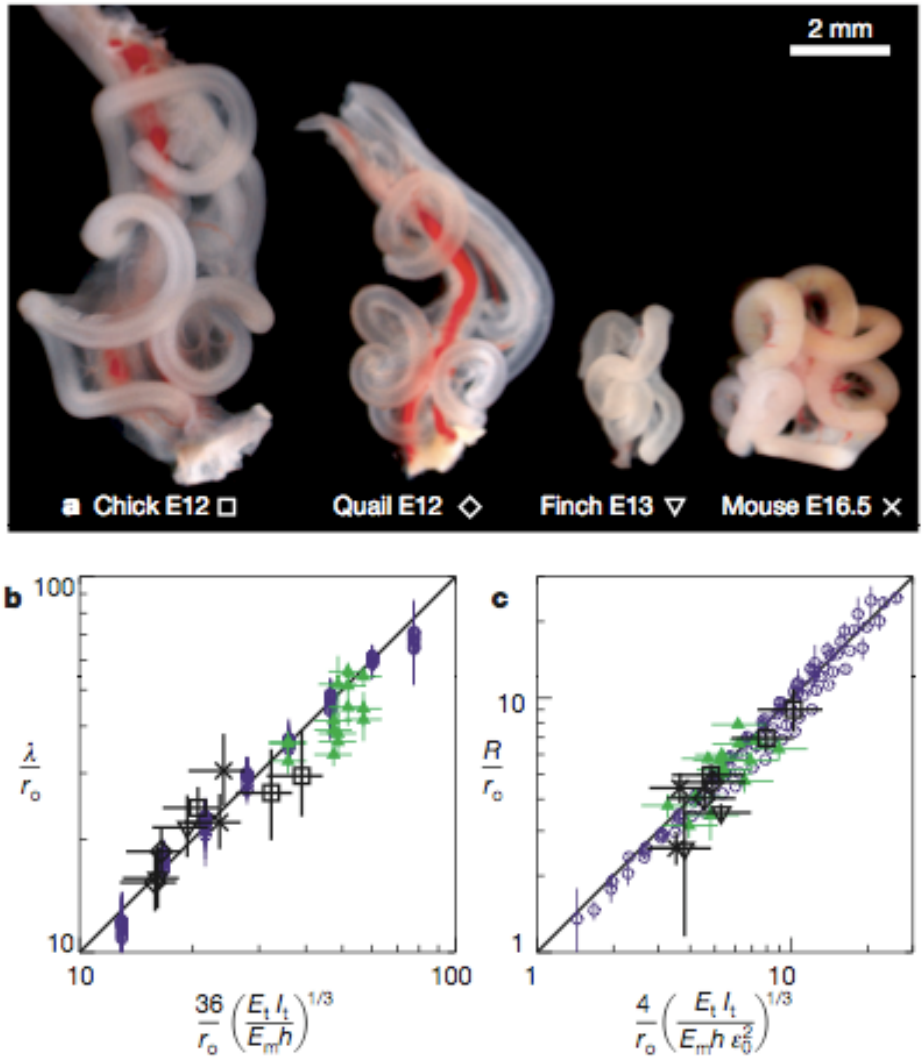

Figure 2.5. Comparative predictions for looping parameters across species. a, Gut looping patterns in the chick, quail, finch and mouse, to scale show qualitative similarities in the shape of the loops, although the size and number of loops vary substantially. **b**, Comparison of the scaled contour length ë/*r*0 vs. eq. (3a) are consistent with the scaling law (1) for the different species. Black symbols are for the animals shown in (a), other symbols are the same as in fig. 4b. **c**, Comparison of the scaled loop radius *R*/*r*0 vs. eq. (3b) are consistent with the scaling law (2) for the different species. Symbols are as in **b**. In **b** and **c**, points are reported for chick E8-12-16, quail E12-15, finch E10-13 and mouse E14.5-16.5.

Table 2.2

Species		n	λ (mm)	R (mm)
Quail E12	Experimental observation	9.0 ± 0.7	4.6 ± 0.4	1.2 ± 0.1
	Computational model*	10.0 ± 1.3	4.1 ± 1.0	1.2 ± 0.3
Finch E13	Experimental observation	5.5 ± 0.5	3.6 ± 0.5	0.6 ± 0.3
	Computational model†	5.3 ± 0.8	3.7 ± 0.9	0.9 ± 0.2
Mouse E16.5	Experimental observation	6.0 ± 0.5	6.0 ± 0.7	0.7 ± 0.1
	Computational model‡	5.6 ± 0.8	6.4 ± 1.5	1.0 ± 0.1

* L_t = 41.3±0.4 mm, h = 14.9±1.6 μm, r_o = 248±13 μm, r_i = 154±12 μm, E_m = 515±206 kPa, E_t = 4.4±1.3 kPa, ε_p = 110±13 %, and ε_0 = 23±5 %.

† L_t = 19.7±0.8 mm, h = 6.0±0.6 μm, ro = 227±14 μm, ri = 120±13 μm, E_m = 802±321 kPa, E_t = 2.6±0.8 kPa, ε_p = 110±11 %, and ε_0 = 32±5 %.

‡ L_t = 35.9±0.9 mm, h = 12.3±1.6 μm, r_o = 270±16 μm, r_i = 178±14 μm, E_m = 94±37 kPa, E_t = 1.9±0.9 kPa, ε_p = 200±13 %, and ε_0 = 64±5 %.

Table 2.2. Summary of the observed number of loops, loop wavelength and radius for the quail, finch and mouse given the geometrical and physical parameters associated with the gut and the mesentery show that the model predictions are quantitatively consistent with observations.

strain, producing tightly coiled loops, as seen in Figure 2.5a. Interestingly the physiological stresses in the mesentery fall in the same range (see Supplementary Information) for all the species investigated in this study, suggesting that both growth and properties of tissues might be regulated by mechanical feedback.

Discussion

The developing intestine is a simple elongated tubular structure that is stereotypically and reproducibly folded into a compact organ through the process of looping morphogenesis. Our study has shown that the associated looping patterns are quantitatively determined by the differential growth between the gut tube and dorsal mesentery and their geometric and elastic properties, both in an organism and across species using a combination of quantitative experiments, computations and scaling arguments. We thus bring a quantitative biomechanical perspective to the mostly metaphoric arguments in *On Growth and Form*[2].

The simplicity of the mechanical origin in the diversity in gut looping patterns, long associated with the adaptive significance of the distinct diets and residence times in different animals[18] also suggests that since it is sufficient to modulate the uniform tissue growth rates, tissue geometry and elasticity of the gut-mesentery system to change these patterns, these are the minimal properties upon which selection has acted to achieve the looping patterns found in nature.

Identification of the relevant cellular parameters influencing gut morphogenesis opens the door to future studies of the genes involved in controlling cell proliferation and matrix formation in space and time, and sets the stage to understand the processes by

which biochemical and biophysical events across scales conspire to drive the developmental regulation of growing tissues.

Materials and Methods

Embryos. Fertile chicken eggs (White Leghorn eggs) were obtained from commercial sources. Fertile zebra finch eggs were provided by the lab of Tim Gardner at Boston University. Fertile Japanese quail eggs were obtained from Strikland Game Bird. All eggs were incubated at 37.5°C and staged according to Hamburger and Hamilton[20] (HH). Mouse embryos were collected from stage pregnant females (Charles River Laboratories).

Immunohistochemistry and histology. Small intestines were collected from chick embryos at desired stages and fixed in 4% paraformaldehyde in PBS and embedded in paraffin wax, allowing for 10mm transverse sections of the gut tube. Fast green staining was performed as described in ref. 20. Immunohistochemistry was performed with rabbit polyclonal anti-phospho-H3 (1:100) (Millipore) overnight at 4 degrees in PBS containing 3% goat serum and 0.1% Triton X-100. Sections were next incubated with Alexa Fluor 594 goat-anti-rabbit secondary antibody (Molecular Probes) (1:300) for 1 hour at room temperature. DAPI (Molecular Probes) was used as a nuclear counter stain and to determine the size of the inner and outer radii of the gut tube.

***In ovo* gut surgeries.** The gut tube and the dorsal mesentery were separated *in ovo* at HH stage 23-25 by using a pulled glass needle to cut the connection between the two tissues. Most, but not all, of the connection was ablated as care was taken to avoid puncturing the dorsal aorta which runs over the gut tube and dorsal mesentery at this stage. Embryos were re-incubated until E12 when they were collected to examine the resulting looping pattern.

Physical simulacrum using rubber. We cut a wide strip of elastic rubber sheet (McMaster-Carr) of various thicknesses. The sheet was held stretched in one direction at the desired extension using clamps, and a silicon rubber tubes (NewAge Industries, inc.), was stitched to the sheet using sewing thread (further details, see Supplementary Information).

Calibration of the magnetic force. The attractive interaction between a permanent disc magnet (commercial grade, axially magnetized, neodymium Nd-Fe-B; The Magnet Source) and high precision ball bearings' steel balls (AISI 440C stainless steel, radii r_b=0.122, 0.253 and 0.398 mm; New England Miniature Ball Corp.) was calibrated using a "falling ball viscometer" geometry: immersed in a tube filled with pure glycerol, the magnet is approached atop the ball that consequently rises (we ensured that all materials used to manipulate the beads and the magnet during the measurements, calibration and tensile tests, had no magnetic susceptibility). The force exerted by the magnet is balanced by gravity, drag and inertia. At low Reynolds number, drag force and inertia can be measured from the ball trajectory that is extracted using video tracking (see details in Appendix I). We can then calculate the attractive force *F(d)* between the magnet and the ball as a function of their separation distance *d*. We report our results in Fig. S3 and Table S1 (Appendix I). Notably, for distances $2<d<8$ mm used in the tissue tensile test described thereafter, the force ranges from 1mN to 1mN.

Measurements of tissue mechanical properties. We surgically dissected fragments of the mesentery and of the gut tube from live embryos. Samples of the mesentery were cut out to leave a well-defined, constant millimeter-width stripe with principal axis either perpendicular to the tube (radial measurement) or parallel to the tube pathway (tangential

measurement). For mesentery fragments, the steel beads were glued using synthetic glue (Instant Krazy Glue) at one end of the tissue stripe. The other end was pinned to an agarose gel layer. During the dissection of the sample, we kept sections of the tube or of the superior mesenteric artery to provide convenient handles to attach the bead (see Figure 2.3d and Appendix I, where sections of the tube are clearly visible). For gut tube fragments, the steel beads were inserted into the tube and secured by tying the lumen using a hair with an overhand knot. The other end of the tube was held on the agarose gel using a horseshoe pin (Figure 2.3e & Appendix I). All dissections, manipulations and tensile tests were performed in Ringer buffer (Sigma Aldrich), and the measurements occurred within a few hours after the dissection. The magnet was attached to a plastic arm held on a micrometric translation stage, and approached to the sample on the agarose gel (Appendix I). The magnet attracts the steel bead and stretches the sample in a controlled fashion. The tensile tests were video-recorded to track the extension L of the sample and the distance bead-magnet d, and were ran the following way: the sample was first pre-conditioned by stretching it once to an extension ratio greater than 1, after which the magnet was removed to let the sample relax to its rest length L_0, at which stage we visually extracted the rest width w_0 of mesentery samples. The magnet was then moved back towards the sample in a step piecewise motion. At each step, the sample stretches and we perform the next step approach of the magnet only after a visual equilibrium extension of the sample is reached. We thus effectively measured the static elasticity of the tissue, by mean of the nominal stress $F(d)/A_0$ response to a nominal strain $e=L/L_0-1$; here A_0 is the cross section of the sample at rest: $A_0=w_0(1+\varepsilon_p)^{1/2}h$ for the mesentery by virtue of material incompressibility, and $A_0=p(r_o^2-r_i^2)$ for the tube. We further verified

that this method returns reproducible results, with same-sample variations below sample-to-sample variations that we measured at about 50%. Several stress-strain response curves, corresponding to samples of mesentery and gut tubes extracted from different Chicken E16 embryos are shown in Appendix I to appreciate the level of reproducibility.

Computational model. The mesentery is modeled as a hexagonal lattice of linear springs with rest length a_m, whose discrete energy $F_m = \frac{\sqrt{3}E_m h}{4}\sum_{ij}(r_{ij}-a_m)^2 + \frac{E_m h^3}{12\sqrt{3}}\sum_{\alpha\beta}(\mathbf{n}_\alpha - \mathbf{n}_\beta)^2$ accounts for in-plane stretching (first term, where r_{ij} is the spring length between nodes *i* and *j*) and out-of-plane bending (second term, where $\mathbf{n}_\alpha$ is the unit normal vector to the triangular facet) such that it tends to the energy of an elastic membrane of thickness *h* and modulus E_m as $a_m \to 0$ [17]. The gut tube is modeled with a similar 2-element width lattice of springs with rest length a_t. The discrete energy $F_t = \frac{5.6\sqrt{3}E_t I_t}{8r_o^3}\sum_{ij}(r_{ij}-a_t)^2 + \frac{E_t I_t}{2r_o\sqrt{3}}\sum_{\alpha\beta}(\mathbf{n}_\alpha - \mathbf{n}_\beta)^2$ of this strip contains also in- and out-of-plane deformations terms (first and second term respectively), which are chosen such that the in- and out-of-plane bending stiffness converge both to $E_t I_t$ for a tube of outer radius r_o (see details in Appendix I). At various time points in the development of the gut (E8, E12, E16), the parameters by $h, I_t, E_m, E_t, \varepsilon_0$ are all experimentally measured and input into the energy, with the relative growth $\varepsilon_0 = a_m / a_t - 1$ imposing the mismatch strain between the membrane and the tube attached to it. Then the energy $F_m + F_t$ is minimized by a damped molecular dynamics algorithm[17], to yield the equilibrium configuration of the gut-mesentery composite system.

References

1. His, W. *Anatomie Menschlicher Embryonen.* Leipzig, Germany, Verlag von F.C.W. Vogel (1880).

2. Thompson, D. W. *On Growth and Form.* Cambridge University Press, Cambridge (1917).

3. Johnson, R. L. & Tabin, C. J. Molecular models for vertebrate limb development. *Cell* **90**, 979-990 (1997).

4. Metzger, R. J. & Krasnow, M. A. Genetic control of branching morphogenesis. *Science* **284**, 1635-1639 (1999).

5. Hufnagel, L. *et al*. On the mechanism of wing size determination in fly development. *Proc. Natl. Acad. Sci. U. S. A.* **104**, 3835-3840 (2007).

6. Beloussov, L. V. *et al.* Mechanical stresses in embryonic tissues: patterns, morphogenetic role, and involvement in regulatory feedback. *Int. Rev. Cyt.*, **150**,1-34 (1994).

7. Taber, L. A. Biomechanics of cardiovascular development. *Annu. Rev. Biomed. Eng.* **3**,1-25 (2001).

8. Salazar-Ciudad, I. & Jernvall, J A computational model of teeth and the developmental origins of morphological variation. *Nature*, **464**: 583-86 (2010).

9. Hamant *et al.* Developmental patterning by mechanical signals in *Arabidopsis*. *Science* **322**: 1650-55 (2008).

10. Forgacs, G. and Newman, S. *Biological physics of the developing embryo*. Cambridge University Press (2005).

11. Schoenwolf, G. *et al. Larsen's Human Embryology.* Elsevier Health Sciences, United Kingdom (2008).

12. Kurpios, N. A. *et al*. The direction of gut looping is established by changes in the extracellular matrix and in cell:cell adhesion. *Proc. Natl. Acad. Sci. U. S. A.* **105**, 8499-8506 (2008).

13. Davis, N. M. *et al*. The chirality of gut rotation derives from left-right asymmetric changes in the architecture of the dorsal mesentery. *Dev. Cell.* **15**, 134-145 (2008).

14. Hecksher-Sorensen, J. *et al*. The splanchnic mesodermal plate directs spleen and pancreatic laterality, and is regulated by Bapx1/Nkx3.2. *Development* **131**, 4665-4675 (2004).

15. Kleinman, R. E. *et al. Walker's Pediatric Gastrointestinal Disease*. B.C. Decker, Ontario (2008).

16. Fung, Y. C. *Biomechanics: Mechanical Properties of Living Tissues.* Springer-Verlag, New York (1993).

17. Liang, H. & Mahadevan, L. The shape of a long leaf. *Proc. Natl. Acad. Sci. U. S. A.* **106**, 22049-22054 (2009).

18. Beddard, F. E. *The Structure and Classification of Birds.* Longmans, Green, and co. London New York [etc.] (1898).

19. Mitchell, C. P. On the intestinal tract of birds. *Proc. Zool. Soc. London* **64**, 136-159 (1896).

20. Hamburger, H. & Hamilton, H. L. A series of normal stages in the development of the chick embryo. *J. Exp. Morphol.* **88**, 49-92 (1951).

Chapter Three

Villification

Villification

Amy E. Shyer[1*], Tuomas Tallinen[2,3*], Nandan L. Nerurkar[1], Zhiyan Wei[2], Eun Seok Gil[4], David L. Kaplan[4], Clifford J. Tabin[1^], L. Mahadevan[2,5,6,7,8,9^]

[1] Department of Genetics, Harvard Medical School, Boston MA 02115

[2] School of Engineering and Applied Sciences, Harvard University, Cambridge MA 02138

[3] Department of Physics, University of Jyväskylä, P.O. Box 35, FI-40014 Jyväskylä, Finland

[4] Department of Biomedical Engineering, Tufts University, Medford MA 02155

[5] Department of Organismic and Evolutionary Biology, Harvard University, Cambridge MA 02138

[6] Department of Physics, Harvard University, Cambridge, MA 02138

[7] Department of Systems Biology, Harvard Medical School, Boston MA 02115

[8] Wyss Institute for Biologically Inspired Engineering, Harvard University, Cambridge MA 02138

[9] Kavli Institute for Nanobio Science and Technology, Harvard University, Cambridge MA 02138

**These authors contributed equally to this work*

This chapter contains the manuscript titled "Villification", in preparation for submission to Science. It is modified to better fit the style of this dissertation. A. E. Shyer is co-first author on this manuscript. C.J.T., A.E.S., L.M. and T.T designed the research; A.E.S. (biological and biophysical experiments), T.T. (biophysical and computational experiments, data analysis) conducted the research; N.L.N. (contributed to design of modulus measurement apparatus), Z.W. (built computational model for calculating moduli), E.S.G. and D.L.K. (designed and constructed silk tubes) contributed essential tools; and A.E.S., T.T., L.M. and C.J.T. wrote the paper.

Summary:

The intestinal villi are critical elaborations of the lining of the gut, essential for providing sufficient surface area for nutrient absorption. In both the developing human and chick gut, the villi are formed in a step-wise progression, wherein the mesenchyme and attached epithelium are together first folded into longitudinal ridges, then a zigzag pattern, and finally individual villi. We find that these steps of villification are tightly correlated with the differentiation of radially organized smooth muscle layers of the gut. Experimental manipulations where smooth muscle differentiation is specifically blocked during gut morphogenesis, or where artificial non-muscle barriers are introduced in the system, demonstrate that formation of the smooth muscle layers is necessary for each sequential step of villification to occur. The muscle acts to restrict the expansion of the proliferating and growing endoderm and mesenchyme; this generates compressive stresses that lead to the buckling and folding of these tissues. The final step in which the villi emerge additionally depends upon a shift from uniform endodermal and mesenchymal proliferation to a pattern where cell division is restricted from the most luminal aspect of the folded tissue. A quantitative computational model incorporating measured differential growth and the geometric and physical properties of the developing chick gut recapitulates the morphological patterns seen during chick villification. From a comparative perspective, in spite of the conservation of the progression of villi development between certain avian and mammalian species, there is a great diversity in the structures lining the gut in different taxa, and in their morphological progression. By examining the timing and requirement for smooth muscle formation in other

species as well by tuning our model to accommodate measured species-specific modes of differential growth, as well as their geometric and physical properties, we find that a subset of the same basic biophysical processes underlie the formation of intestinal folds in frog (which do not form villi) and the villi in mice (which form villi without going through ridge and zigzag intermediates).

Introduction:

The intestinal villi are critical structures, dramatically increasing the epithelial surface area through which nutrients can be absorbed. The rapidly renewing epithelial surface of the villi is maintained by stem cell populations located at their base, and is of particular importance as it is a major target of human carcinogenesis. However, the morphogenesis of intestinal villi during embryogenesis remains very poorly understood.

In descriptive terms, the primitive midgut is established as a cylinder with an outer layer of mesenchyme and inner, luminal lining of endoderm. As development proceeds, distinct radial layers of smooth muscle differentiate. In parallel, the luminal surface of the gut transforms from a smooth surface to a much more complex, convoluted morphology. In humans, as well as in mice and birds, this takes the form of an organized array of finger-like projections termed intestinal villi (Reviewed in McLin et al. 2009 and Noah et al. 2011). There are, however, a wide array of luminal morphologies found in the midgut of other species, from honeycomb-like patterns in some snakes (Ferri et al. 1976) to parallel ridges in goldfish and some mammals such as the platypus (Walker et al. 2004, Krause 1974), to zigzag ridges in frogs (McAvoy et al. 1978). Moreover, even among species that do form villi, the gut does not appear to undergo the same morpogenesis. Human, cattle, and chick villi have all been reported to form through a

sequential process involving formation of longitudinal ridges, zigzags, and then villi (Bell et al. 1980, Lacroix et al. 1984, Hilton 1902, Winkler et al. 1998, Coulombre et al. 1958). In contrast rodent villi do not initiate ridge-like folds but rather form direct epithelial elevations from the smooth luminal surface (Sbarbati et al. 1982).

Regardless of the steps by which they form, the induction of intestinal villi requires crosstalk between tissue layers of the gut (Madison et al. 2004). Studies of tissue interactions during villi formation have focused on chemical communication, highlighting many molecular players required for proper villi formation (Karlsson et al. 2000, Ormestad et al. 2005, Walton et al. 2012). These studies, however, have not shed light on how intestinal villi grow and take their form during development. While early work (Burgess 1975) suggested there could be a mechanical underpinning of the formation of intestinal villi, and while a recent study puts forth a theoretical model of this process (Hannezo et al. 2012), there has been no systematic biological or physical study of this supposition.

Results:

Radial morphogenesis and differentiation of the chick midgut

During villus development in the chick, the gut proceeds through several stages of morphogenesis forming a series of distinct, striking patterns. Until embryonic day 7 (E7) the gut tube, comprised of an inner endodermally derived epithelium, and an outer layer of mesenchyme, maintains a smooth luminal surface (Figure 3.1A). However, at E8 as the first layer of circumferentially oriented smooth muscle begins to form, longitudinal ridges start to arise appearing as an inward buckling of the tube (Figure 3.1B), thus

breaking the azimuthal symmetry of the lumen. These ridges increase in number until E13 when the differentiation of this layer is complete. At this point, a second layer of muscle that is oriented longitudinally differentiates just exterior to the circular layer, and concurrently the folds shift into parallel zigzags (Figure 3.1C), thus breaking the axial symmetry of the lumen. Finally, at E16 a third muscle layer that is also longitudinally oriented differentiates just interior to the circular layer and coincides with the formation of bulges arising from the zigzag pattern, presaging the formation of definitive villi (Figure 3.1D). Because the emergence of luminal ridges, zigzags, and villi each coincides with the formation of a layer of smooth muscle, we hypothesized that development of each of these patterns requires the formation of a smooth muscle layer.

Intestinal ridges form due to muscle-constrained azimuthal growth of the endoderm and mesenchyme

The notion that differential growth of layered tissues can lead to their patterning via buckling is classical (His 1870), and has been evoked to understand epithelial buckling and ridge formation in biological contexts such as the trachea and esophagus (Wiggs et al. 1997, Yang et al. 2007), employing models of two or three layer tissues with disparate growth rates and properties (Moulton and Goriely 2011). However, investigations of mucosal buckling have typically been restricted to the study of adult tissue in both healthy and diseased states, rather than in developmental settings, where dramatic changes in morphology occur on the time scale of days.

In the gut, at the time that ridges form on the luminal surface, there are three layers: an external layer of newly differentiating, mesodermally derived smooth muscle, an adjacent layer of still undifferentiated mesodermally derived mesenchyme, and an

Figure 3.1. Formation of luminal patterns in chick corresponds with differentiation of smooth muscle layers. Left, Transverse sections of developing chick guts immunostained for nuclei (DAPI, blue) and smooth muscle actin (αSMA, green). Middle, close-up of left panel to view smooth muscle layers. Right, whole mount images of corresponding chick gut lumen pattern, longitudinal axis of gut tube runs top to bottom. (A) The chick lumen is smooth before muscle layers form. (B) Longitudinal ridges form just as a layer of circularly oriented smooth muscle differentiates (arrowhead). The number of folds increases as this muscle layer develops. (C) Just as zigzags form from ridges, a layer of longitudinal muscle develops exterior to the circular layer (arrowhead). Zigzags periodicity is maintained but zigzags become larger and more compact over time. (D) As villi emerge from zigzags, a second longitudinal layer forms, interior to the circular layer (arrowhead). Villi continue to elongate through hatching. (Scale bar = 100μm).

Figure 3.1 (Continued)

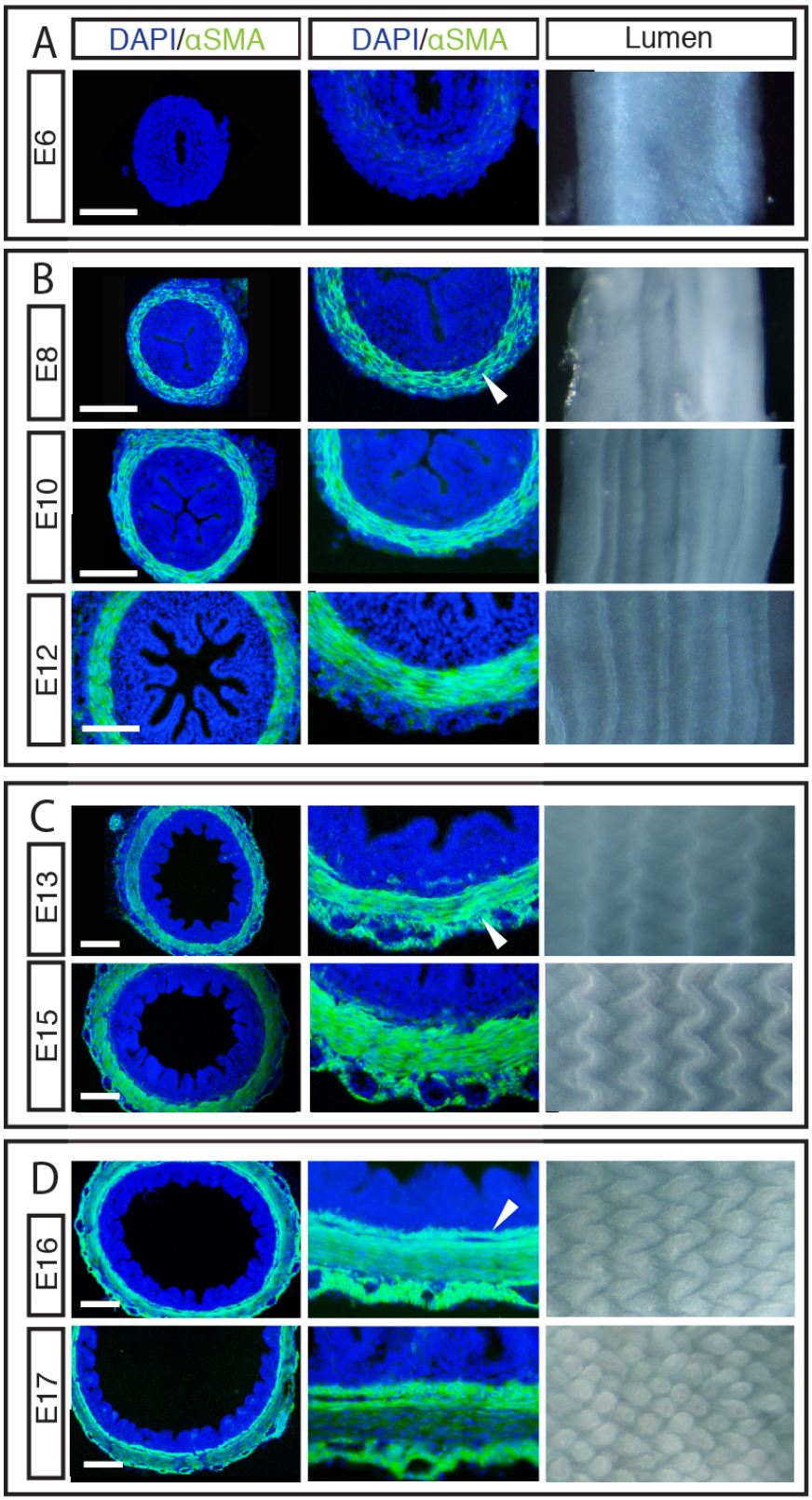

innermost layer of endodermally derived epithelium. In principle, the two mesodermal layers could act in concert forcing the buckling of the endoderm, or conversely, the mesenchyme and endoderm could form a functional composite buckling together in the context of the surrounding smooth muscle. To test these possibilities we manually separated these layers and observed the effects on their respective morphologies. We first assayed whether the circular layer of smooth muscle is integral to the ridge pattern by surgically separating it from the combined mesenchymal and epithelial layers. We performed these dissections at various stages: from E8, when the circular muscle layer has first formed, to E12 just before the following longitudinal muscle layer forms. In all these stages, we found that once separated the mesenchyme and attached epithelium unfold in a matter of a few seconds indicating that these layers were under reversible elastic compression when constrained within the muscle layer which acts to directs the folding seen at these stages (Figure 3.2A). In order to quantify this compression, we compared the outer circumference of the separated mesenchyme and endoderm to the inner circumference of the once attached muscle layer (Figure 3.2B). The ratio of the muscle circumference to that of the mesenchyme and endoderm, i.e. the circumferential stretch consistently averages to 0.55 across the stages measured; thus the mesenchyme and endoderm are compressed within the ring of smooth muscle by a factor of approximately two. These results demonstrate that the circular muscle layer is required for ridge maintenance. Conversely, however, the separation of the endoderm from the composite of mesenchyme and muscle does not abolish ridge pattern in the mesenchyme (Figure 3.2C), showing that this interaction is not required for maintenance of the ridges.

Taken together these results support a model where the muscle, once differentiated, forms a stiff constraint mechanically blocking the expansion of the mesenchyme and endoderm. Hence, with further growth of these tissues relative to the muscle layer, compressive forces are generated and buckling occurs. This leads to the prediction that in the absence of muscle differentiation, the gut tube would simply continue to expand radially and no ridges would form. To test this, we developed an explant culture system, which allows for in vitro growth of guts for up to 72 hours. When segments of E6 guts, which have smooth lumens and lack any smooth muscle, are cultured for 48 hours *in vitro*, they differentiate a ring of circumferential smooth muscle, and three parallel ridges, indistinguishable from guts allowed to develop to E8 in vivo (Figure 3.2D). E6 guts were then cultured in the presence of 10 μM AG1295 or FK506, drugs known to block the differentiation of smooth muscle, via two distinct mechanisms (Kurahashi et al. 2008 and Fukada et al. 1998). Guts segments cultured in the presence of either compound do not form a smooth muscle layer and do not form luminal folds (Figure 3.2D). Importantly, these compounds do not influence proliferation cell death when compared to guts grown with the vehicle alone (Appendix II). Further, we observed a significant increase in the outer circumference of guts lacking circular smooth muscle when compared to control gut samples, suggesting that blocking smooth muscle differentiation eliminates circumferential restriction of the outward expansion of the gut tube. To quantify the degree of constraint provided by the muscle, we compared geometry of the cultured tissues and find that the ratio of inner circumference of the muscle layer in the control samples to the outer circumference of the gut segments cultured with either compound to be on average 0.53. This result suggests when these

Figure 3.2. Differentiation of circularly oriented smooth muscle is necessary for maintenance and development of ridges. (A). Whole gut rings from E8, E10, E12 guts (left) are surgically separated at the junction of the mesenchyme and circular smooth muscle, (dotted line). The separated mesenchyme and attached endoderm unfold (middle) when detached from muscle (right). **(B)** Inner circumference of muscle layer (green line) compared with outer circumference of the separated mesenchyme and endoderm (blue line) over time. A measure of compression is obtained by taking the ratio of green line to the blue line (bar graph). **(C)** Surgical separation of endoderm from mesenchyme and muscle at E10 does not abolish ridge pattern in mesenchyme. **(D**) Top, Transverse sections of a fresh E8 gut or E6 guts cultured in vehicle alone (Dmso) or with either 10μm AG1295 or 10μm FK506 for 48 hours, immunolabeled with DAPI (blue) and SMA (green), experiment schematized bottom left. Bottom right, Quantification of compression from E8 muscle. Graph shows the ratio of the inner circumference of the circular muscle at E8 (green arrowhead) to the mesenchyme outer circumference after culture (blue arrowhead). **(E)** Transverse sections of guts labeled as in D, culturing E6 guts in the presence of either SNP or Motilin does not impact ridge formation. (**F)** Transverse sections of guts labeled as in D, cultured in silk tubes of 380μm inner diameter (top), 300μm inner diameter (middle), or cultured in 300μm and extracted before fixation (bottom). ($n<3$ for all culture experiments, error bars represent one stdev. Scale bar = 100μm)

Figure 3.2 (Continued)

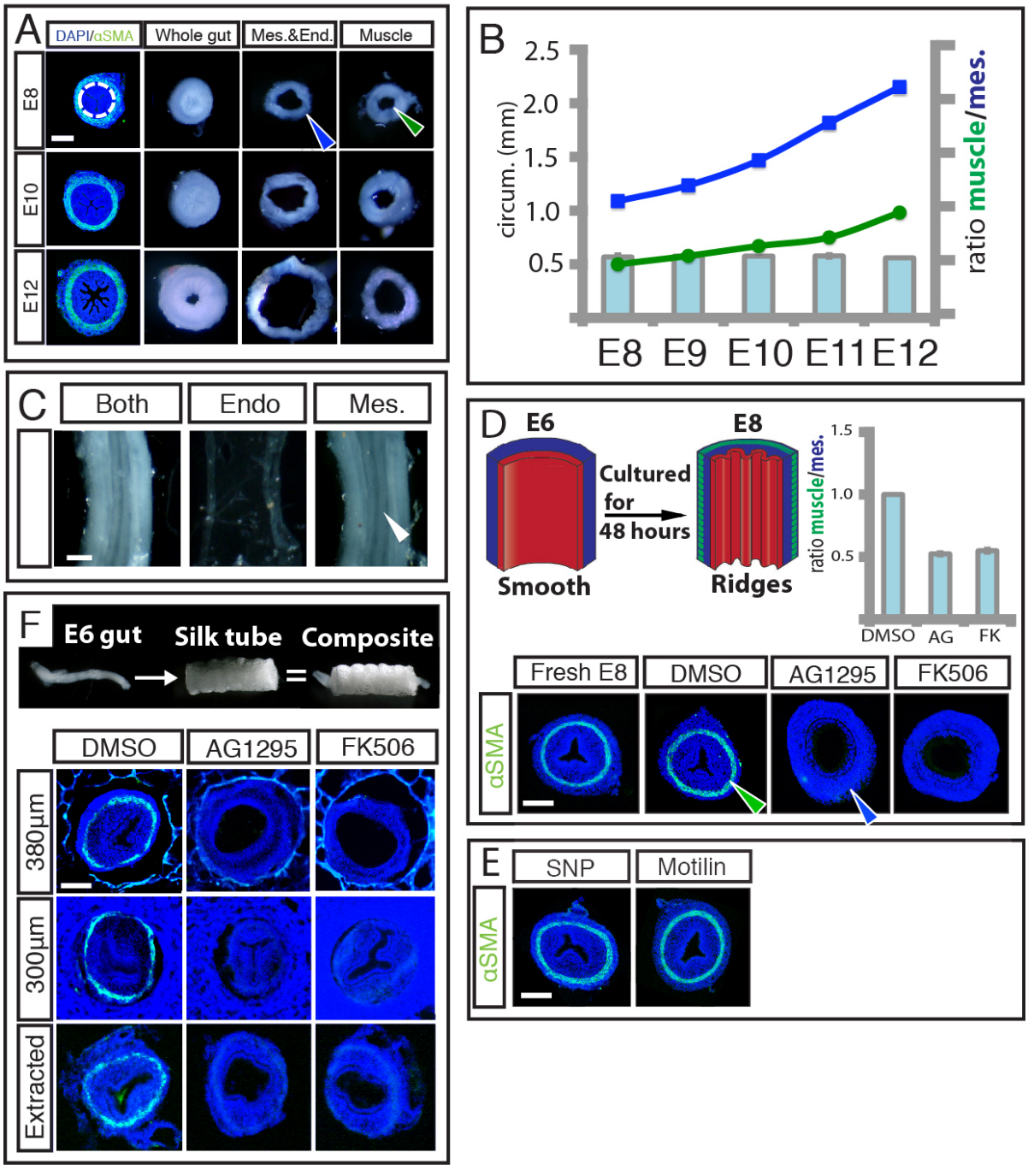

layers are attached in the E8 gut, the mesenchyme and attached epithelium are compressed by a factor of approximately two (Figure 3.2D). This ratio strikingly mirrors the stretch ratio obtained from surgical separation of the layers, indicating specifically that differentiation into smooth muscle accounts for nearly all of the circumferential constraint provided by the outer layer of gut tube.

Because the smooth muscle begins peristaltic compression as soon as it forms, in principle the contractile properties of the muscle could be critical in driving epithelial buckling in addition to, or instead of, its function as a physical barrier to expansion. To test whether this active contraction of the circular layer of smooth muscle contributes to ridge formation, we cultured E6 gut segments with either sodium nitroprusside (SNP), a compound shown to inhibit active smooth muscle contraction during peristalsis, or Motilin, known to increase the frequency and size of peristaltic smooth muscle contraction (Benabdallah et al. 2008, Harada et al. 1992). After 48 hours in culture, neither compound impacted the formation of ridges suggesting the spontaneous mechanical activity of smooth muscle is not required for epithelial buckling (Figure 3.2E). Rather, these data support the hypothesis that the circular smooth muscle acts a physical constraint to expansion of the mesenchyme and endoderm.

To assess whether the lack of expandability of the differentiated circular smooth muscle layer is sufficient to drive luminal folds, we sought to mimic its physical presence in samples where smooth muscle development was blocked and assess ridge formation. We utilized silk tubes, which can be manufactured to any distinct thickness, and hence stiffness, while permitting free diffusion due to their inherent porosity. We synthesized silk tubes by spinning silk fibroin around a reciprocating rotating mandrel with a

specified diameter, allowing us to mimic the inner diameter of the circular smooth muscle (Lovett et al. 2008). E6 gut segments were cultured inside of silk tubes in the presence of either AG1295 or FK506 or vehicle alone for 48 hours. Gut segments grown in vehicle alone develop a layer of circular smooth muscle and form luminal folds (Figure 3.2F). As shown above, the segments grown in AG1295 or FK506 do not form a muscle layer and when given sufficient room to expand in silk tubes of 380um inner diameter, still do not form luminal ridges (Figure 3.2F). Markedly, the segments grown in AG1295 and FK506 that are restricted by a tube of the requisite inner diameter of 300um do form ridges similar to those seen in control guts in spite of the lack of smooth muscle (Figure 3.2F). These results demonstrate that the mechanical barrier function of the circumferential smooth muscle is sufficient to cause luminal ridges. Moreover, upon removal from the confining silk tube, these ridges are quickly lost, much as they were from gut tubes upon surgical removal of the circumferential muscle layer (Figure 3.2F), supporting our previous finding that continued mechanical constraint is required for the maintenance of luminal ridges.

Zigzag intermediates in villus morphogenesis form in response to muscle-constrained bilateral compression

Previous work has shown that a thin layer atop an elastic substrate may take on a zigzag topography when it is compressed biaxially (Bowden et al., 1998, Mahadevan et al. 2005, Rizzieri et al. 2006). Therefore we hypothesized that the longitudinal layer of smooth muscle that forms at E13 may induce longitudinal compression that, in conjunction with the previously established circumferential muscle compresses the gut biaxially. To investigate whether the longitudinal layer combines with the circular layer

to form the zigzag pattern, we again performed surgical separations of the mesenchyme and attached endoderm from the muscle layers, measuring separated lengths along the longitudinal axis. When we perform this dissection at E12, before longitudinal muscle or zigzags have formed, the length of the separated mesenchyme and attached endoderm is approximately the same as the muscle to which it was attached (Figure 3.3A). Thus, as expected, before the longitudinal layer forms, the mesenchyme and endoderm are not under longitudinal compression. However, after the longitudinal layer and zigzags arise at E13, E14, and, E15, the ratio of the length of the separated muscle to mesenchyme and endoderm is approximately 0.75, 0.69, and 0.55 respectively (Figure 3.3A). This suggests that the mesenchyme and endoderm are under an increasing amount of longitudinal compression as the muscle layer forms. Conversely, separation of the endoderm from the mesenchyme and muscle at E14 does not abolish zigzag pattern, suggesting this interaction is not required for maintenance of the zigzags (Figure 3.3B).

To directly test whether the development of the outer longitudinal layer is required for the formation of zigzags, we returned to our *in vitro* culture system. When E12 gut segments, which have only a single, circumferential smooth muscle layer and contain parallel ridges but not zigzags, are cultured for 48 hours, they differentiate a longitudinal smooth muscle layer and undergo morphogenesis to form zigzags, indistinguishable from guts harvested at E14 (Figure 3.3C). We next repeated these cultures in the presence of one of the two muscle blocking compounds, AG1295 or FK506. Importantly, we find these compounds only block further smooth muscle formation and leave established layers intact. However, in the presence of either AG1295 or FK506 the longitudinal muscle layer fails to differentiate and the zigzag

Figure 3.3. Differentiation of outer and inner longitudinally oriented smooth muscle layers is required for development of the zigzags and villi, respectively. **(A)** Ratio of lengths in the longitudinal axis of separated muscle layers to mesenchyme and attached endoderm before (E12) and after (E13, E14, E15) longitudinal muscle layer forms. **(B)** Separation of endoderm from mesenchyme and muscle at E14 does not abolish zigzag pattern in mesenchyme. **(C)** E12 guts cultured in vehicle alone (Dmso) or with either 10μm AG1295 or 10μm FK506 for 48 hours, experiment schematized bottom left. Top panels are luminal views, bottom are longitudinal sections immunolabeled with DAPI (blue) and SMA (green). Bottom right, Quantification of compression from E14 longitudinal muscle. Graph shows the ratio of the length of the control cultured segments to those lacking muscle. **(D)** Fresh E17 gut or E15 guts cultured in vehicle alone (Dmso) or with either 10μm AG1295 or 10μm FK506 for 48 hours. Top panels are luminal views, bottom are longitudinal sections, labeled as in 3C. Bottom right, Quantification of compression from inner longitudinal muscle. Graph shows the ratio of the length of the control cultured segments to those lacking muscle. ($n<3$ for all culture experiments, error bars represent one stdev. Scale bar = 20μm)

Figure 3.3 (Continued)

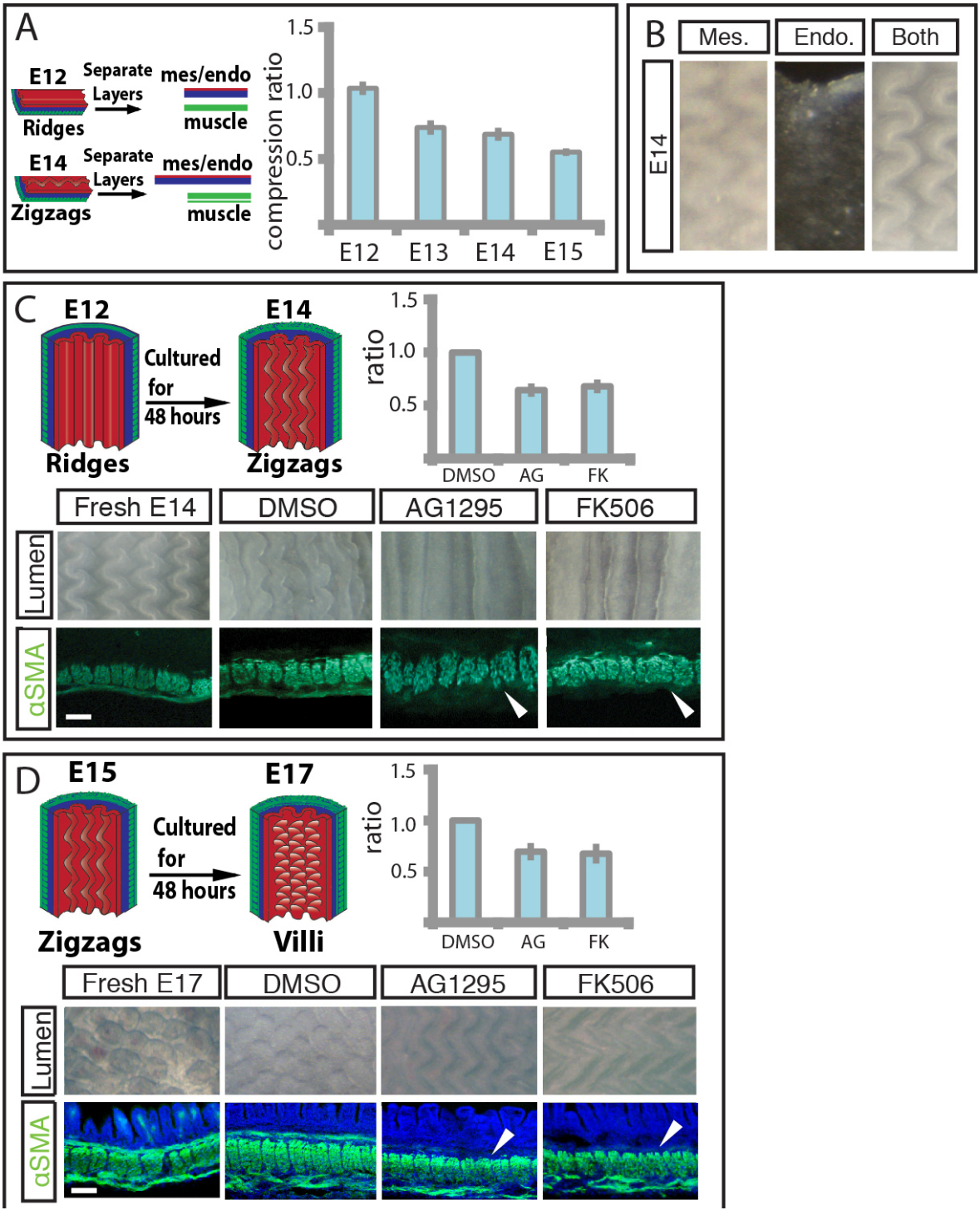

pattern does not form, but the ridges remain (Figure 3.3C). This suggests that the longitudinal layer is required to induce zigzags. Additionally, when differentiation of this longitudinal muscle is blocked, the length of the tube increases significantly compared to control gut segments. Specifically, the ratio of the length of control gut segments to those cultured in the presence of either compound is on average 0.66, suggesting that, in the E14 gut, this longitudinal muscle layer compresses the mesenchyme and attached epithelium by a factor of approximately 1.5 (Figure 3.3C). Importantly, this corroborates the value for compression from the outer longitudinal layer in E14 we obtained following manual dissection of the layers. As for ridge formation above, transformation of ridges to zigzags occurs independent of active contraction of smooth muscle (Appendix II).

Smooth muscle differentiation is also required for villus morphogenesis

To investigate whether the final patterning step where villi form is also dependent on the differentiation of a smooth muscle layer, we cultured E15 guts, which have both a circumferential layer and outer longitudinal layer, for 48 hours in the presence of the muscle blocking compounds or with the drug vehicle alone. We find that gut segments cultured with vehicle alone develop an inner longitudinal muscle layer and begin to form villi. However, those cultured with either AG1295 or FK506 fail to form this muscle layer and also do not initiate villi outgrowth (Figure 3.3D). Again, when differentiation of this longitudinal muscle is blocked, the length of the tube increases significantly compared to control gut segments (Figure 3.3D). The ratio of the length of gut segments grown with vehicle alone to that of those lacking the outer longitudinal muscle is on average 0.68., suggesting this inner longitudinal layer also compresses the mesenchyme and endoderm by a factor of approximately 1.5. These findings support the hypothesis

that differentiating smooth muscle acts as a barrier to the expansion of the attached mesenchyme and endoderm, compressing these layers first circumferentially to form ridges, then longitudinally to form zigzags, and finally longitudinally again to form villi. We emphasize that since the patterns relax when the muscular constraints are released, the morphology of the lumen minimizes the energy of constrained growth in a soft layered elastic tissue.

Quantitative models substantiate the role of tissue growth constrained by muscle layers to drive ridge and zigzag formation

To more quantitatively understand the physical basis of luminal patterns, we constructed a mathematical and computational model of the process based on measured geometrical and biophysical parameters (Figure 3.4A). We start with a composite of a cylindrical elastic mesenchyme adhered to a cylindrical endoderm that are together squeezed to fit into a rigid tubular configuration with an outer boundary of diameter D that mimics the circular smooth muscle. Based on our measurements of the mechanical properties we assume that the tissues may be well described using a simple neo-Hookean constitutive model. The strain energy density of the model is given by

$$W = \frac{\mu}{2}\left[\mathrm{Tr}\left(\mathbf{F}\mathbf{F}^{\mathrm{T}}\right)J^{-2/3} - 3\right] + K(J - \log J - 1),$$

where μ and K are the shear and bulk moduli, respectively, $\mathbf{F}$ is the elastic deformation gradient, and $J = \det(\mathbf{F})$. Given the timescale of several days, we assume that the tissues are compressible with a typical $K = 3\mu$ of a solid matrix of soft tissues (Cowin et al. 2007). We simulate the relative growth of the endoderm and mesenchyme compared to

the muscular layer by expanding their stress free states. At each stage, we minimize the elastic energy of the system by a custom finite element model (Appendix II).

In Figure 3.4B we show a series of images from a biologically-based simulation that closely mimics the folding pattern progression observed from E7 to E14 (Figure 3.4C). Direct input parameters of the simulations include the outer circumference $S_o = \pi D$ of the compressed mesenchyme-endoderm composite, which increases by a factor of 2.7 as time goes from E7 to E14 (Figure 3.4A), and elastic moduli. Based on the measurements (Figure 3.4A), we assume that the endoderm is 12 times stiffer than the mesenchyme ($\mu_e = 12\mu_m$), i.e., we neglect the small difference in the measured modulus between E8 and E10. We also utilize image analysis to measure the circumference and thickness of the endoderm and the volume occupied by the mesenchyme from the stained cross-section images (Appendix II). Since these measurements are based on deformed states, they cannot be input directly to the simulation. Instead, we look for rates of uniform growth of the mesenchyme and endoderm that lead to the observed cross-section geometries and compression ratios in circumferential and longitudinal directions (Figure 3.4A). To this end, the mesenchyme is allowed to grow laterally with the muscle such that its stress free circumference is $1.5\,S_o$ throughout the simulation. The endoderm grows faster than the mesenchyme; its stress-free circumference is assumed to expand by a factor of 13.5 from E7 to E14. The stress-free thickness of the endoderm is one third of that of the mesenchyme, $h_e = h_m / 3$, and the thickness of the whole mesenchyme/endoderm composite decreases by a factor 1.5 during the simulation, implying that the endoderm thickness decreases from 18 μm at E7 to 12 μm at E14. From E7 to E14 the intestine grows substantially also in the longitudinal direction. We do not

Figure 3.4. A numerical simulation based on measured geometric and biophysical parameters predicts the formation of an increasing number of ridges, and the emergence of zigzags in chick (**A**) Left, Circumference of the inner boundary of the muscle (blue) and endoderm (red). Middle left, Spacing of longitudinal ridge folds, measured along the endoderm, relative to the deformed thickness of the endoderm. Black dashed line is the theoretical estimate $\lambda \approx 10h_e$. Middle right, Ratio of muscle to separated mesenchyme-endoderm composite in circumferential (blue) and longitudinal (red) directions. Right, Shear modulus of mesenchyme (blue) and endoderm (red), and the relative modulus (magenta). In all panels solid lines are experimental observations and dashed lines are computational model. **(B)** A series of images from a single simulation run that shows the first folds forming in a fully stuffed tube, followed by an increase in the number of folds and buckling into zigzag pattern. **(C)** Transverse sections of corresponding chick guts labeled with DAPI (blue) and SMA (green) show similarity of patterns.

Figure 3.4 (Continued)

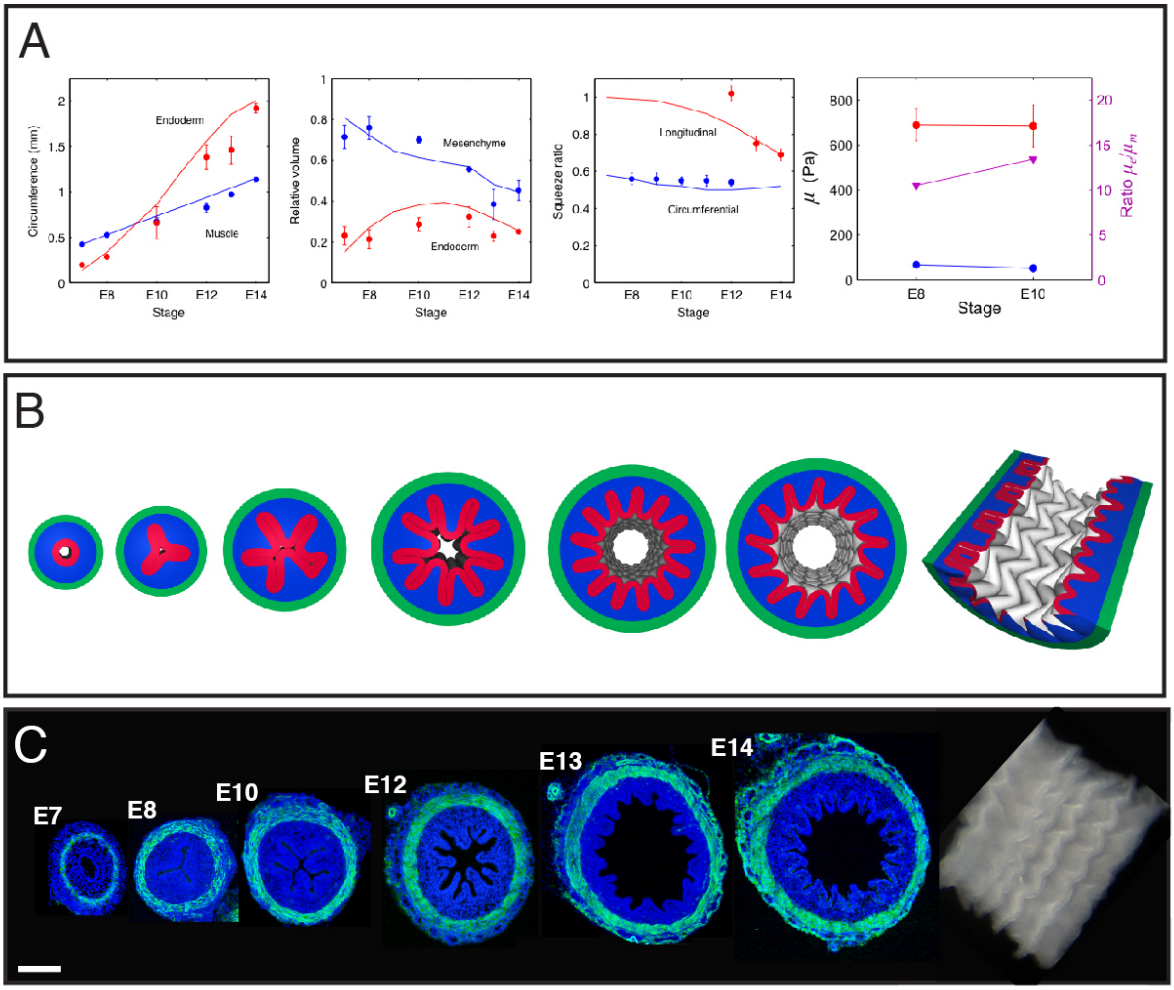

simulate this explicitly, but model a longitudinal section of length 1.25*D* and apply periodic boundary conditions at the ends. This does not affect the results since only the growth relative to the muscle is important.

Under the assumption of small strains, a thin sheet of stiffness μ_e and thickness h_e assumes a buckling wavelength $\lambda = 4.36(\mu_e / \mu_m)^{1/3} h_e$ on an elastic substrate of stiffness μ_m (Chen et al. 2004). With $\mu_e / \mu_m = 12$ $\lambda \approx 10 h_e$ which, when measured along the endoderm, matches fairly well with the spacing of the longitudinal folds (Fig. 4A). However, strains in the intestine are large and also the substrate (mesenchyme) is under substantial compression, which implies that the mesenchyme thickness also affects the spacing. Furthermore, the folds during stages E8 to E12 when the tube is entirely stuffed are not of uniform size, as is evident from, for example, E12 cross-sections that show small and large folds alternating. Nevertheless, by varying the thickness and stiffness of the endoderm in our simulation, we confirm that the above theoretical λ approximately predicts how the average spacing changes with thickness and stiffness of the endoderm.

In conclusion, from E7 to E12 our model captures the progression of luminal ridge folds during chick villi development. Furthermore, our simulation can be extended to model the subsequent patterning step at E13 and E14 where zigzags arise simply by applying a longitudinal compressive strain due to the longitudinal muscle layers equivalent to the values shown in Figure 3.3 Thus ridge and zigzag formation follows from simple mechanical instabilities in the growing but constrained tissue, associated with two broken symmetries first circumferentially and then longitudinally.

Villus formation requires localized changes in endodermal and mesenchymal proliferation in addition to smooth muscle differentiation.

While we demonstrated in Figure 3 that additional compression from the inner longitudinal layer is necessary for the formation of villi from zigzags, simply applying additional longitudinal compression in our simulation after zigzags form does not result in the formation of villi (Appendix II). This suggests additional parameters contribute to the process of villi formation. Previous work in mouse has shown that although proliferating cells can be found uniformly across the mesenchyme and endoderm before villi arise, as villi form, proliferating cells are found only in the intervillous region (Reviewed in Noah et al. 2010). A similar phenomenon occurs in chick as proliferating cells appear uniformly within each tissue layer through the formation of zigzags, but at E15 just before villi arise, proliferating cells are found predominantly in the valleys between the raised zigzags (Figure 3.5A). Interestingly, we note that after definitive villi begin to form at E16, proliferation is no longer restricted from the tips (Figure 3.5A). We hypothesize that this proliferation pattern at E16 is due to a change in topography of the zigzags as villi arise, displacing the proliferating populations upward from the valley. Specifically each "arm" of the zigzag twists out of the plane and into the lumen, pinching-off a region of the zigzag arm near each "elbow", delineating pockets of mesenchyme surrounded by endoderm that will each become a villus (Figure 3.5B). This shift in topography brings the highly proliferating cells in the zigzag valleys to the tips of the pattern where they can find the most room to expand.

To theoretically investigate whether the topographical changes during zigzag twisting would in fact relocate regions of proliferation as villi form, we created a

malleable clay model of zigzags. We labeled the proliferating regions of our model zigzags and performed a manual twist of the clay, mimicking the twist observed in the E16 gut (Figure 3.5B). We then sectioned the resulting shape (Figure 3.5C). The resulting clay label localization closely matches Edu staining for proliferation in the sectioned post-twist E16 gut tissue (Figure 3.5C). These results suggest that the tissue movements we describe could account for the proliferation patterns seen, and that non-uniform proliferation is involved in villi formation.

To probe the effect of non-uniform growth in our computational model, we set up a minimal configuration of planar mesenchyme and endoderm layers (Appendix II). Initially, the layers are grown laterally such that the endoderm is compressed to 50% of its stress-free width and length and the mesenchyme is compressed to 60% of its stress-free width and length. This implies that the mesenchyme-endoderm composite would expand by nearly a factor of two in both lateral directions if it were relaxed, in agreement with the measured compression ratios during late zigzag stages (Figure 3.3A). The compression first results in a tightly packed elastic zigzag pattern (Appendix II), with the energetically optimal spacing of approximately twice the thickness of the mesenchyme-endoderm composite in both directions. The approximate equality of the longitudinal and azimuthal spacing can be confirmed from experimental images in Figure 3.5. As a next step we incorporate non-uniform growth to this pattern by allowing the growth of spots of the endoderm in the zigzag valleys . These spots are centered at the deepest points of the valleys, and their initial lateral diameter is $6\,h_e$ in the stress-free endoderm. These spots

Figure 3.5. The formation of villi from zigzags involves non-uniform proliferation and a complex change in topography. (A) Transverse sections of Edu labeled (red) guts show of patterns of proliferation over time. **(B)** Top, Luminal views of guts from E15 to E16 as villi form. Bottom, clay models, purple label represents proliferating regions. Clay model is twisted to mimic change in topology seen above. **(C)** Top, Labeled twisted model is sliced reveal label localization. Bottom, Edu label in longitudinal sections of E16 guts. **(D)** Top, Images from a single simulation run that incorporates non-uniform proliferation along with measured geometric and biophysical parameters show the formation of villi in whole mount, shown at an angle and from above. Bottom, Corresponding whole mount images of the chick lumen as villi form (red color and stained puncta are due to antibody stain and can be disregarded) **(E)** Top, Sections of the same simulation shown in D. Bottom , Sections of corresponding stage in chick demonstrates similarity of geometry.

Figure 3.5 (Continued)

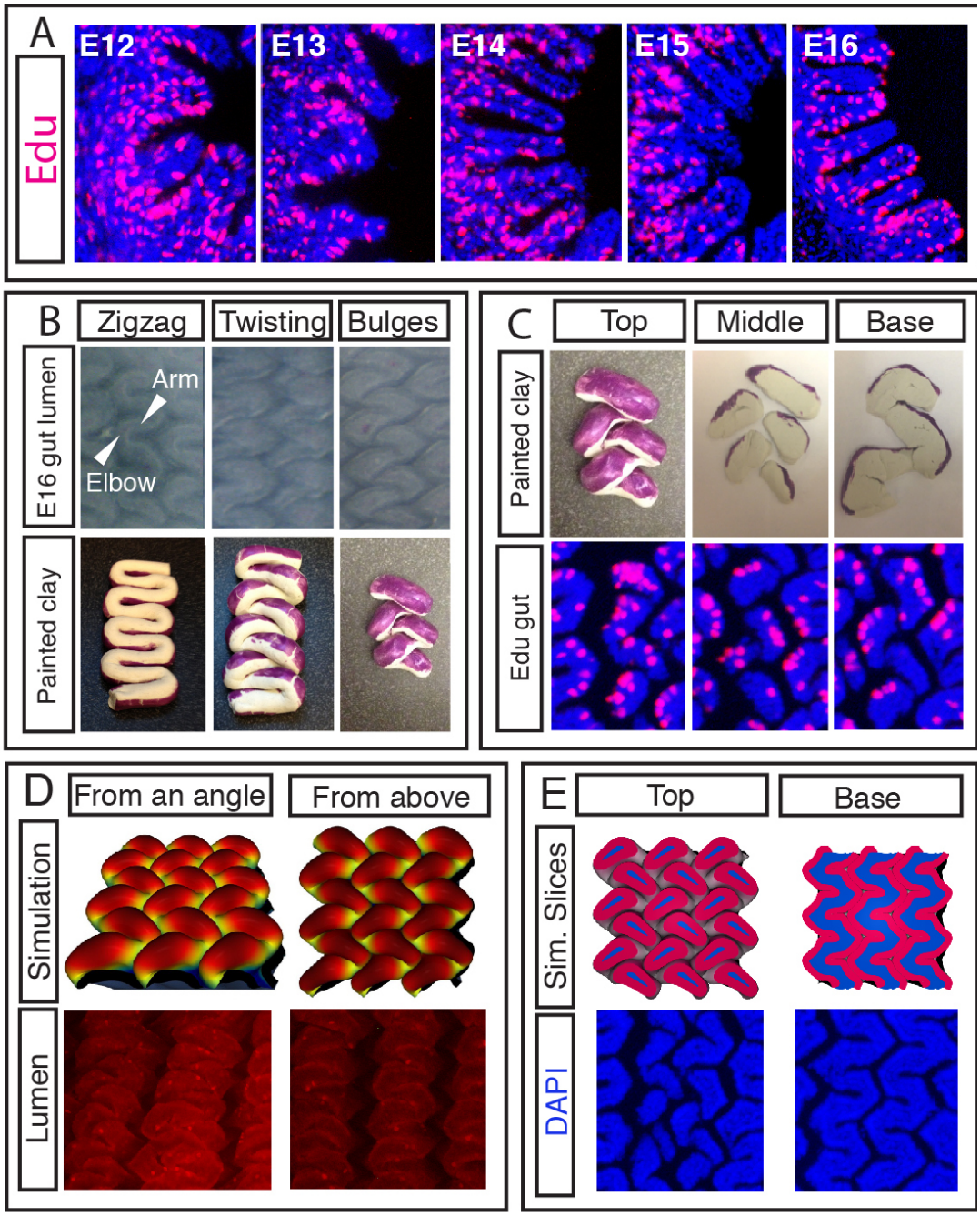

are grown laterally such that their diameter doubles during the simulation relative to areas of the endoderm outside the spots. This pattern of growth causes the zigzags to shift and twist so as to relocate the rapidly growing regions to the arms, similar to our clay model and consistent with the observed proliferation patterns. As the spots keep growing at the arms, they form pre-villous bulges. Sliced plane views of this twisted pattern reveal its similarity with the corresponding experimental patterns (Figure 3.5E); bulging peaks are rotated while the regular zigzag valleys persist deeper in the pattern. Thus, although the final patterning step where definitive villi arise involves more complex morphogenetic tissue movements and non-uniform proliferation, it follows from the same general physical principles as the first patterns since it is guided by the preceding zigzag pattern.

A phylogenetically conserved mechanism directs luminal gut morphogenesis

Although the patterns seen on the luminal surface of the gut vary dramatically across species (Appendix II), the underlying physical principles we have uncovered for the chick lumen morphology suggests that these patterns develop according to the same basic mechanical mechanisms elsewhere. In the adult *Xenopus*, the luminal surface of the intestine is folded into a zigzag pattern (McAvoy et al. 1978). Development of this pattern involves progressing through the same patterning steps as in chick, with a smooth lumen forming ridges that then develop into zigzags (Figure 3.6A). We observe that ridges form just as the circular smooth muscle layer thickens, and zigzags arise when the outer longitudinal muscle is said to shorten longitudinally, likely shortening the attached tissue layers (Figure 3.6A and Schreiber et al. 2005). Importantly, *Xenopus*, unlike chick, do not develop an inner longitudinal muscle layer (Figure 3.6A). It follows from our studies in chick that the absence of this layer may explain why individual villi do not

develop from zigzags in *Xenopus*. Specifically without the additional compression from this longitudinal layer, the *Xenopus* gut remains in a zigzag pattern in the adult state.

In the adult mouse, villi resemble the finger-like projections seen in chick, however, the mouse gut does not progress through intermediate patterns during villi development and instead, villi emerge directly from a smooth lumen (Sbarbati et al. 1982). Importantly, however, we find that villi arise in mouse only once smooth muscle layers form (Figure 3.6E). This suggests that the relatively rapid pace at which muscle layers form in the mouse does not leave time for proliferation and expansion of the inner mesenchyme and endoderm in between the differentiation of sequential muscle layers, and thus prevents the development of visible intermediate patterns such as ridges and zigzags. Specifically, in mouse, all muscle layers develop within a 48 hour period, a very short time window when compared to the 8 days required for muscle to fully develop in chick (McHugh et al. 1995). To experimentally determine whether villi formation in mouse also requires differentiation of smooth muscle, we tested the effect of the smooth muscle inhibitors used in our chick studies on the formation of villi in mouse guts grown in culture. Just as in chick, the mouse guts grown in the presence of AG1295 or FK506 do not form smooth muscle and concomitantly do not develop villi (Figure 3.6B). This finding suggests that compression from the smooth muscle layer is necessary for, and likely drives, the formation of villi in mouse.

To quantitatively test our theory of villi formation in mouse, we performed mechanical and morphometric measurements of the tissues in the developing mouse gut (see Figure 3.6C). We incorporated these measurements into our simulations (Appendix II) and, in agreement with our results in chick, we found that the relative growth with the

Figure 3.6. The mechanical mechanism of villi formation can be extended to other species. (A) Luminal pattern formation in *Xenopus*. Sectioned immunolabeled with DAPI (blue) and SMA (green). The gut begins with a smooth lumen (stage 54), ridges form as circular muscle thickens (stage 63), and zigzags arise as the longitudinal layer shortens during metamorphosis (stage 66). **(B)** Transverse sections of E11.5 mouse guts (labeled as in A) cultured in vehicle alone (Dmso) or with either 10μm AG1295 or 10μm FK506 for 72 hours, experiment schematized above. **(C)** Left, Circumference of the inner boundary of the muscle (blue) and endoderm (red). Solid lines are experimental observations and dashed lines are computational model. Thin dashed line shows the stress-free circumference of the simulated endoderm. Middle, Spacing of folds relative to the deformed thickness of the endoderm, measured along the endoderm. Right, Shear moduli of mesenchyme (blue) and endoderm (red), and the relative moduli (magenta). **(D)** A series of cross-sectional (top) and luminal (bottom) images from a single simulation run based on measurements from the developing mouse gut. Color shows distance of the luminal surface to the center line relative to the diameter of the tube. **(E)** Top, Transverse sections (labeled as in A) and Bottom, Whole mount images of the lumen for corresponding stages during mouse villi formation.

Figure 3.6 (Continued)

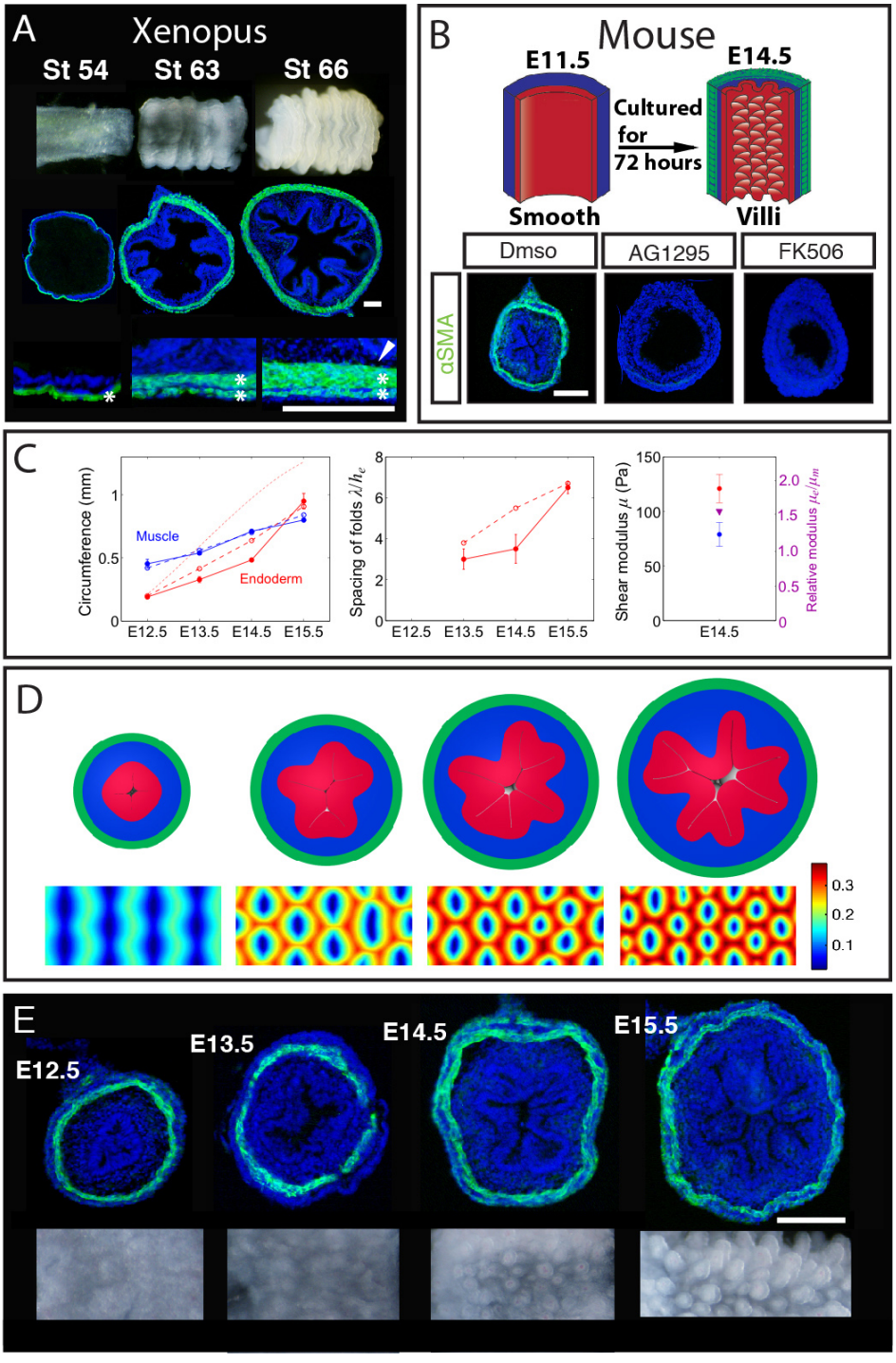

measured geometric and biophysical parameters suffice to predict the formation of villi in mouse (Figures 3.6D and 3.6E). Most importantly, while in chick the endoderm is more than ten times stiffer than the adjacent mesenchyme, the mouse endoderm is only approximately 1.5 times as stiff as the mesenchyme (Figure 6.3C). Our simulations reveal that the soft endoderm in mouse is essential for the initial folding that occurs in endoderm alone, and for the direct formation of an array of pre-villous bumps rather than zigzags. Indeed, the formation of bumps in mouse is qualitatively similar to sulcus formation on squeezed gel surfaces that lack a stiff top layer and the associated zigzag phase (Tallinen et al. 2013, Dervaux et al. 2012). The formation of bumps requires substantial compression in both lateral directions, which in mouse occurs via nearly simultaneous development of circumferential and longitudinal smooth muscle layers. As in chick, both mesenchyme and endoderm are under substantial compression. They buckle together, with spacing of bumps comparable to the thickness of the whole mesenchyme-endoderm composite. Stretching the classical buckling formula $\lambda = 4.36(\mu_e / \mu_m)^{1/3} h_e$ to predict the spacing of bumps yields $\lambda \approx 5h_e$, i.e., half of the fold spacing in chick, which approximately coincides with our measurements (Figures 3.4A and 3.6C, note that we approximate h_e by the deformed thickness in the plots). In general, however, the above formula for λ gives only a qualitative hint on how the endoderm modifies the spacing.

Discussion:

In the chick, a series of morphological patterns emerge during the process of villi formation, each attributable to the differentiation of a layer of smooth muscle. The

mesenchyme and endoderm are first compressed circumferentially leading to buckling in this circumferential axis, then compressed longitudinally adding longitudinal buckling to the pattern generating zigzags. Finally, further longitudinal compression from a newly formed second layer of longitudinal muscle forces the tissue layers to buckle radially into the lumen, because circumferential and longitudinal compression prohibits further expansion in these axis. We find that this same mechanism underlies villi formation in mouse, and that differences in the way villi emerge can be explained by relatively minor changes in the relative growth and physical properties of the developing tissues.

Recently, an alternative view of mouse villus formation was put forward; postulating a potential inductive role of the endodermally derived signal Sonic Hedhehog (Shh) in triggering a morphogenetic cascade directing villus outgrowth (Walton et al. 2012). The key results that led in this direction were the failure of villus formation when Shh activity was pharmacologically blocked with the Shh antagonist cyclopamine and the increased size of the villi when guts were provided with excess Shh signal. However, as these reagents were applied prior to villus formation, they were de facto also treated prior to smooth muscle differentiation. As Shh activity is both necessary and sufficient to direct smooth muscle formation in the developing intestine (Sukegawa et al. 2000, Ramahlo-Santos et al. 2000) an alternative interpretation is suggested. This would, of course have been difficult for the prior authors to anticipate in the absence of knowledge of the direct role of smooth muscle differentiation on villus formation.

Our study highlights the fact that relatively minor change in the growth, physical properties, and geometry of the developing tissue in various species can dramatically alter the process of villi formation, or final pattern formed. Perhaps these properties are

an elegantly simple set of parameters which can be tuned in nature to drive variation. We previously reported a qualitatively similar mechanical basis based on differential growth for the looping pattern of the intestine and determined that variation in the same simple set of parameters are responsible for a diverse array of looping patterns (Savin et al. 2011). Importantly, just as altering luminal topography influences luminal surface area, looping allows for a longer tube to be packed into the small space allotted for the organ in the body, providing an additional opportunity for increased luminal surface area. Therefore, the embryo may simply exploit basic mechanical properties of the tissue, optimizing gut size and luminal morphology in concert to form the best adapted intestine. For example, if the chick gut must fit into a relatively small space, the optimal gut could be highly looped or could be shorter with a more intricate surface morphology. Interestingly the inner longitudinal muscle layer concurrently restricts the tube length and increases luminal surface by driving the formation of villi, a topography with more surface area than zigzags. As this layer does not form in frog, we speculate that it arose in higher vertebrates as a mechanism to optimize gut function through changing both gut length and luminal surface pattern simultaneously.

Materials and Methods:

Embryos and Dissections

Fertile chicken eggs (White Leghorn eggs) were obtained from commercial sources. All eggs were incubated at 37.5°C and staged according to Hamburger and Hamilton. Timed pregnant CD1 mice were obtained from Charles River. *Xenopus* embryos were derived by *in vitro* fertilizations and allowed to develop to the desired stages. The layers of the gut tube were separated using human hair, fine forceps, and tungsten wire to cut the connections between the layers.

Immunohistochemistry and Edu Staining

Small intestines were collected from embryos at desired stages and fixed in 4% paraformaldehyde in PBS and embedded in OCT, allowing for 14um transverse sections of the gut tube. Immunohistochemistry was performed with mouse anti-smooth muscle actin (FITC-conjugated, 1:200, Abcam), rabbit polyclonal anti-phospho-H3 (1:100, Millipore) overnight at 4 degrees in PBS containing 3% goat serum and 0.1% Triton X-100 (Davis, Kurpios et al. 2008). Sections were next incubated with Alexa Fluor 594 goat-anti-rabbit secondary antibody (1:300) for 1 hour at room temperature. DAPI (molecular probes) was used as a nuclear counter stain. 1mM Edu (Invitrogen) was injected in ovo and embryos were harvested 4 hours post-injection. Edu was detected in sectioned tissue using the Click-iT Edu system (Invitrogen)

Organ Culture

Intestines were dissected from the embryos of the desired stage in cold PBS, connective tissue was removed, and intestines were gently pinned to an agar base with tungsten wire (for chick E6 or E12, mouse E11.5) or placed on transwells (Costar 3428) (for chick E15)

in DMEM media supplemented with 1% pen/strep and 10% Chick Embryonic Extract (for chick tissue only). Intestines were cultured for 48 – 72 hr (as indicated in the figure legends) at 37 °C with 5% CO2 with media changes every 24 hr.

Elasticity Measurements

Layers of tissue were separated as described above, a ring of gut tissue was placed in a dish of PBS between a glass coverslip, acting as a substrate, and a piece of glitter which was attached to a long, thin tungsten beam. The beam act as a cantilever, allowing us to observe beam bending as a measure of force from the tissue on the beam – a stiffer tissue will cause more bending (deflection). The ring of tissue is then compressed along its diameter through slow measured movements of a micromanipuator attached to the tungsten beam. Images were taken every 10um and measurements of the displacement of the beam were attained by analyzing the resulting data with imageJ. Plots of displacement of the beam (distance the glitter moved) versus force (deflection of the beam * bending stiffness) were created for each sample. The resulting data were incorporated into a fine element model (details in Appendix II) in order to determine the modulus of the measured sample.

Computational model of luminal patterns

See text, for details Appendix II.

Clay Modeling

Clay models were constructed out of Crayola Modeling Clay (CVS) and labeled with purple nail polish. Photos were taken with a standard digital camera.

References

H. Benabdallah, D. Messaoudi, K. Gharzouli, The spontaneous mechanical activity of the circular smooth muscle of the rabbit colon in vitro. *Pharmacol. Res.* **57**, 132-141 (2008).

Burgess, D. R. Morphogenesis of intestinal villi. II. Mechanism of formation of previllous ridges. J. Embryol. Exp. Morph. 34, 723-740 (1975).

A. J. Coulombre, J. L. Coulombre, Intestinal development. I. Morphogenesis of the villi and musculature. *J. Embryol. Exp. Morphol.* **6**, 403-411 (1958).

E. Hannezo, J. Prost, J. F. Joanny, Instabilities of monolayered epithelia: shape and structure of villi and crypts. *Phys. Rev. Lett.* **107**, 078104 (2011).

N. Harada, Y. Chijiiwa, T. Misawa, M. Yoshinaga, H. Nawata, Direct contractile effect of motilin on isolated smooth muscle cells of guinea pig small intestine. *Life Sci.* **51**, 1381-1387 (1992).

L. Karlsson, P. Lindahl, J. K. Heath, C. Betsholtz, Abnormal gastrointestinal development in PDGF-A and PDGFR-(alpha) deficient mice implicates a novel mesenchymal structure with putative instructive properties in villus morphogenesis. *Development.* **127**, 3457-3466 (2000).

W. J. Krause, Ultrastructure of the platypus and echidna mandibular glands. *Anat. Histol. Embryol.* **40**, 352-359 (2011).

M. Kurahashi *et al.*, Platelet-derived growth factor signals play critical roles in differentiation of longitudinal smooth muscle cells in mouse embryonic gut. *Neurogastroenterol. Motil.* **20**, 521-531 (2008).

B. Lacroix, M. Kedinger, P. Simon-Assmann, K. Haffen, Early organogenesis of human small intestine: scanning electron microscopy and brush border enzymology. *Gut.* **25**, 925-930 (1984).

M. L. Lovett, C. M. Cannizzaro, G. Vunjak-Novakovic, D. L. Kaplan, Gel spinning of silk tubes for tissue engineering. *Biomaterials.* **29**, 4650-4657 (2008).

B. B. Madison *et al.*, Epithelial hedgehog signals pattern the intestinal crypt-villus axis. *Development.* **132**, 279-289 (2005).

L. Mahadevan, S. Rica, Self-organized origami. *Science.* **307**, 1740 (2005).

J. W. McAvoy, K. E. Dixon, Cell specialization in the small intestinal epithelium of adult Xenopus laevis: structural aspects. *J. Anat.* **125**, 155-169 (1978).

V. A. McLin, S. J. Henning, M. Jamrich, The role of the visceral mesoderm in the development of the gastrointestinal tract. *Gastroenterology.* **136**, 2074-2091 (2009).

T. K. Noah, B. Donahue, N. F. Shroyer, Intestinal development and differentiation. *Exp. Cell Res.* **317**, 2702-2710 (2011).

M. Ormestad *et al.*, Foxf1 and Foxf2 control murine gut development by limiting mesenchymal Wnt signaling and promoting extracellular matrix production. *Development.* **133**, 833-843 (2006).

M. Ramalho-Santos, D. A. Melton, A. P. McMahon, Hedgehog signals regulate multiple aspects of gastrointestinal development. *Development.* **127**, 2763-2772 (2000).

T. Savin *et al.*, On the growth and form of the gut. *Nature.* **476**, 57-62 (2011).

R. Sbarbati, Morphogenesis of the intestinal villi of the mouse embryo: chance and spatial necessity. *J. Anat.* **135**, 477-499 (1982).

A. M. Schreiber, L. Cai, D. D. Brown, Remodeling of the intestine during metamorphosis of Xenopus laevis. *Proc. Natl. Acad. Sci. U. S. A.* **102**, 3720-3725 (2005).

A. Sukegawa *et al.*, The concentric structure of the developing gut is regulated by Sonic hedgehog derived from endodermal epithelium. *Development.* **127**, 1971-1980 (2000).

K. D. Walton *et al.*, Hedgehog-responsive mesenchymal clusters direct patterning and emergence of intestinal villi. *Proc. Natl. Acad. Sci. U. S. A.* **109**, 15817-15822 (2012).

B. R. Wiggs, C. A. Hrousis, J. M. Drazen, R. D. Kamm, On the mechanism of mucosal folding in normal and asthmatic airways. *J. Appl. Physiol.* **83**, 1814-1821 (1997).

W. A. Hilton. The morphology and development of intestinal folds and villi in vertebrates. American Journal of Anatomy 1, 459-505 (1902).

H. Hamburger and H.L. Hamilton, A series of normal stages in the development of the chick embryo, *J. Exp. Morphol.* **88** pp. 49–92 (1951).

S. Ferri, L. C. U. Junqueira, L. F. Medeiros AND L. 0. Medeiros, Gross, microscopic and ultrastructural study of the intestinal tube of *Xenodon merremii*. Journal of Anatomy, 121, **2**, pp. 291-301 (1976).

K. Fukuda, Y. Tanigawa, G. Fujii, S. Yasugi, S. Hirohashi, cFKBP/SMAP; A novel molecule involved in the regulation of smooth muscle differentiation. Development **125**, 3535-3542 (1998).

D. R. Burgess, Morphogenesis of intestinal villi II. Mechanism of formation of previllous ridges. Embryol exp. Morph. Vol. 34, 3, pp. 723-740 (1975).

R.L. Walker, A.G. Buret, C.L. Jackson, K.G.-E. Scott, R. Bajwa, and H.R. Habibi, Effects of growth hormone on leucine absorption, intestinal morphology, and ultrastructure of the goldfish intestine. Can. J. Physiol. Pharmacol. **82**: 951–959 (2004)

L. Bell and L. Williams, A Scanning and Transmission Electron Microscopical Study of the Morphogenesis of Human Colonic Villi. Anat Embryol **165** : 437-455 (1982).

Fr. WINKLER, K.-H. WILLE, Uber die friihfetale Entwicklung der Diinndarm-Mukosa des Rindes *(Bos pvimigenius* taurus). Anat. Histol. Embryol. **27**, 33.5-343 (1998).

B. Li, Y.-P. Cao, X.-Q. Feng, H. Gao, Mechanics of morphological instabilities and surface wrinkling in soft materials: a review, Soft Matter **8**, 5728 (2012).

J. Dervaux, M. Ben Amar, Mechanical instabilities of gels, Annu. Rev. Condens. Matter Phys. **3**, 311 (2012).

S. C. Cowin, S. B. Doty, Tissue Mechanics, Springer, New York, 2007.

X. Chen, J. W. Hutchinson, Herringbone buckling patterns of compressed thin films on compliant substrates, J. Appl. Math. **71**, 597 (2004).

T. Tallinen, J. S. Biggins, L. Mahadevan, Surface sulci in squeezed soft solids, Phys. Rev. Lett. **110**, 024302 (2013).

Chapter Four

Epithelial Topography Mediates Localization of Proliferating Progenitors to the Presumptive Intestinal Stem Cell Niche

Epithelial Topography Mediates Localization of Proliferating Progenitors to the Presumptive Intestinal Stem Cell Niche

Amy E. Shyer[1], Tuomas Tallinen[2,3], Clifford J. Tabin[1], L. Mahadevan[2,4,5,6,7,8]

[1] Department of Genetics, Harvard Medical School, Boston MA 02115

[2] School of Engineering and Applied Sciences, Harvard University, Cambridge MA 02138

[3] Department of Physics, University of Jyväskylä, P.O. Box 35, FI-40014 Jyväskylä, Finland

[4] Department of Organismic and Evolutionary Biology, Harvard University, Cambridge MA 02138

[5] Department of Physics, Harvard University, Cambridge, MA 02138

[6] Department of Systems Biology, Harvard Medical School, Boston MA 02115

[7] Wyss Institute for Biologically Inspired Engineering, Harvard University, Cambridge MA 02138

[8] Kavli Institute for Nanobio Science and Technology, Harvard University, Cambridge MA 02138

This project was first conceived by C. J. Tabin and A. E. Shyer. All experiments were conducted by A. E. Shyer. Text and figures were produced by A. E. Shyer, with input from Clifford Tabin, Tuomas Tallinen and L. Mahadevan.

Summary

Adult intestinal stem cells (ISCs) are long-lived, multipotent cells that serve to replenish the mucosal surface of the intestine during homeostasis. In the adult, these cells reside in the crypt, the intestinal niche located at the base of villi. Here we investigate the process by which intestinal stem cells are ultimately localized to the base of each villus. In the early embryo, proliferating progenitors are evenly distributed throughout the epithelium and are then restricted to the space between villi as they form during development. We find, as mechanical forces deform the luminal surface of the gut during villi formation, uniform Shh signal from the epithelium results in local maxima of Shh responsive genes in the mesenchyme. We demonstrate that the shape of the overlying epithelium determines how the mesenchyme receives and interprets these signals, and ultimately induces a new signaling center under the villus tip termed the villus cluster. Signals from the cluster, in turn, feed back to restrict proliferating progenitors in the epithelium, the presumptive precursors of the stem cells, to the base of each villus. Further, we assay for expression of ISC markers in the embryonic gut and find that embryonic progenitors resemble adult ISCs, suggesting ISCs may arise from this pool of embryonic progenitors.

Introduction

As the fastest self-renewing adult tissue, the intestine relies heavily on the resident stem cell population. The epithelial lining of the intestine is maintained during homeostasis by stem cells residing in the crypt, a structure at the base of the villi which

acts as the niche. Until recently, our understanding of intestinal stem cells was limited, as isolation of this population was not possible. However, the discovery of genes specific to these cells has enabled investigation of the behavior and molecular signature of intestinal stem cells. Specifically, lineage tracing and transplantation studies demonstrating that Lgr5-positive cells are multipotent and long-lived have established Lgr5 as a bone fide intestinal stem cell marker (Barker et al. 2007). Impressively, a single Lgr5-positive cell can form a self-renewing, long-lived, gut-like organoid in culture (Sato et al. 2009). Lgr5 is exclusively expressed in the crypt-basal columnar cells (CBCs) located between Paneth cells at the base of the crypt, therefore CBCs have been termed Lgr5-positive intestinal stem cells, (referred to simply as ISCs in this dissertation) (Barker et al. 2007).

In addition to Lgr5, ISCs possess a molecular signature involving several expressed factors including Ascl2, Smoc2, CD44, Msh1, and Olfm4 (Itzkovitz et al. 2011, reviewed in Barker et al. 2012) These genes have been utilized to locate, track, and test the function of ISCs in the adult during homeostasis and in disease. Additionally, assaying expression of these genes has allowed for exploration of the signaling events that maintain the ISC niche. The Wnt, hedgehog, and TGF-β/Bmp pathways, among others, coordinate proliferation, differentiation, and migration events necessary for proper function of the niche (Reviewed in Crosnier et al. 2006). Notably, the Wnt pathway, through the action of its effector Tcf4, is necessary for epithelial proliferation and maintenance of the niche (van Es et al. 2012). Additionally, both Lgr5 and CD44 are prominent targets of Wnt (Barker et al. 2007, Wielenga et al. 1999). Bmps, expressed in a graded fashion in regions outside the crypt, are downstream of hedgehog and serve to restrict Wnt, and therefore proliferation (Haramis et al. 2004, He et a. 2004).

While, in the adult, proliferation is limited to the crypt, in the early stages of gut development, all cells of the endodermally-derived epithelium are mitotically active (Reviewed in Crosnier et al. 2006). After villi begin to form, proliferating cells are found only in the space between the emergent villi (Reviewed in Crosnier et al. 2006, Noah et al. 2010). During the final stages of embryogenesis, the proliferation pattern is further refined within this intervillous space where crypts will later form after birth. It has therefore been postulated that, in the embryo, the epithelium is composed of proliferative progenitors, and adult ISCs are the remnants of this population, protected in some way from differentiation (Reviewed in Crosnier et al. 2006, Takashima et al. 2012). Therefore understanding how proliferation is restricted to the intervillous space may additionally shed light on how ISCs arise and are directed towards the niche.

Because the signaling that governs proper function of the niche during homeostasis is coordinated by pathways with established roles in embryonic development, we speculate these same pathways orchestrate the birth of ISCs during development. The Wnt pathway in the developing intestine has been shown to direct proliferation, as loss of TCF4 results in absence of intervillous proliferation (Korinek et al. 1998). However, the Wnt pathway may have additional, non-proliferative functions in the embryo that differ from its role in the adult (Kim et al. 2007). The PDGF-A ligand is expressed in the epithelium and signals to its receptor in the underlying mesenchyme (Karlsson et al. 2000). This pathway plays a role in establishing the intervillous zone, as loss of the epithelial PDGF-A ligand leads to decreased proliferation (Karlsson et al. 2000). Additionally Shh and Ihh are expressed throughout the epithelium during intestinal development and are upstream of Bmp4 and the transcription factors Foxf1 and

Foxf2 in the mesenchyme (Ramalho-Santos et al. 2000, Ormestad et al. 2005). Loss of hedgehog signal leads to inhibition of Bmps and therefore enhanced activity of Wnt target genes, such as CD44, as well as increased proliferation outside of the intervillous space (Madison et al. 2005). Similarly, loss of Foxf1/2 in the developing intestine leads to expansion of epithelial Wnt signal and proliferation the villous tips (Ormestad et al. 2005). Further, loss of Ihh in the epithelium leads to an increase in Lgr5 expression (Kosinski et al. 2010) These findings suggest that epithelial hedgehog induces Bmp in the underlying mesenchyme which, in turn, represses Wnt signal, proliferation, and potentially Lgr5 in the overlying epithelium. Importantly, because Bmps are expressed in a graded pattern with higher expression at the villous tip than in the mesenchyme at the base of villi, repression of Wnt and downstream proliferation occurs specifically in the surrounding, villous tip epithelium. Therefore these non-uniform mesenchymal patterns play a role in protecting proliferating progenitors in the intervillous space, and an understanding of how these patterns form may shed light on how intestinal ISCs arise.

Additionally, an understanding of ISC development requires spatial and temporal investigation of ISC marker expression during development. In *Drosophila*, a pool of proliferating progenitors are specified in the embryo and adult ISCs arise out of this pool of progenitors. Importantly, all of the markers of adult ISCs in *Drosophila* are expressed in embryonic progenitors (Reviewed in Takashima et al. 2012). Conversely, in *Xenopus*, ISCs appear to arise *de novo*, as markers of ISCs such as Lgr5 do not arise until after metamorphosis (Sun et al. 2010). This process is driven by endogenous thyroid hormone and is accompanied by a wave of cell death in the epithelium (Sun et al. 2010). Surprisingly, the origin of this important cell type in humans, as well as in chick and

mouse, is not known. The earliest established expression of the ISC marker Lgr5 is found at birth, or shortly after, in the intervillous region before crypts form in mouse (Kim et al. 2012, Itzkovitz et al 2012). A limited number of studies have set out to trace ISC markers such as Lgr5 back to their embryonic origin. Preliminary evidence that ISC markers are not embryonically expressed as well as data supporting embryonic expression has been put forth (Kim et al. 2012, Garcia et al. 2009). We hypothesize that ISC marker expression in the embryo aligns with proliferation, as the ability to proliferate is an important component of the ISC signature. Additionally, the signals that regulate proliferation also regulate Lgr5. Alignment of ISC marker expression with this striking regression of proliferation would reveal a strong molecular and cellular resemblance between the embryonic progenitors and adult ISCs. Such a finding would suggest a portion of these embryonic, mitotically-active progenitor cells are preserved in an undifferentiated state in order to give rise to ISCs in the adult.

Through studies of the developing gut in both chick and mouse, we aim to address how epithelial proliferation becomes restricted to the intervillous region, how non-uniform expression patterns in the mesenchyme arise in response to uniform epithelial signals, and whether proliferating embryonic gut progenitors share aspects of the genetic signature of adult ISCs.

Results

Proliferation in the intestine of the developing chick, as in mouse and other species, is initially found uniformly throughout the epithelium but is progressively restricted, and is specific to the crypt after hatching. Specifically, in chick, proliferation

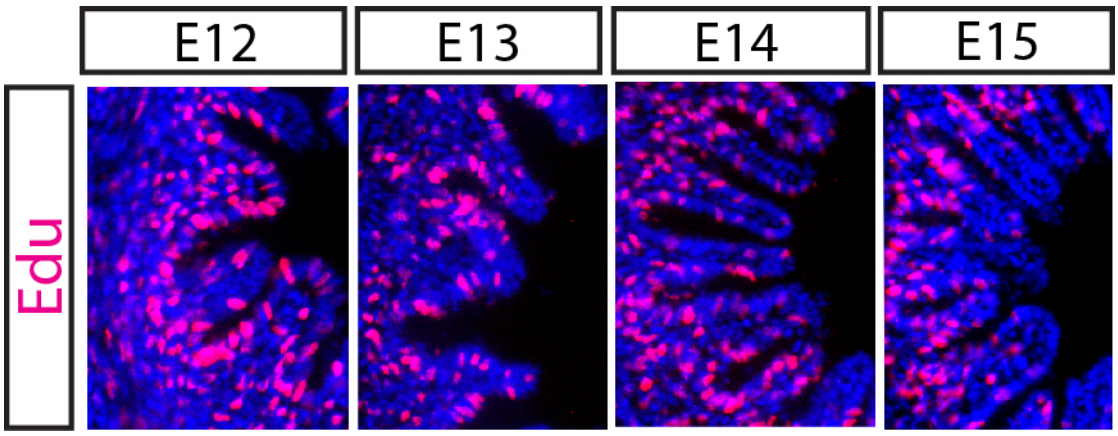

Figure 4.1. Proliferation is restricted from the most luminal aspects of the zigzag topography during gut development. Proliferation at E12 when the luminal pattern consists of many ridges is uniform throughout the epithelium. Beginning at E14 and through E15, just as zigzags are becoming larger and more compact and right before definitive villi form, proliferation is restricted from the inner most aspect of the pattern. Staining is evident only in the regions at the base of the pattern. 1μM Edu was applied *in ovo* for four hours and Edu was detected on 14 μM transverse tissue sections.

is restricted from the most luminal aspect of the zigzag pattern at E15 just as the cluster signal forms and before true villi form (Figure 4.1). Because this restriction is coincident with the formation of the villus cluster, a locus of signal in the mesenchyme under the growing villus tip, we speculate signals from the cluster inhibit proliferation in the adjacent epithelium. In order to address this hypothesis, we first investigated the origin of the cluster and its genetic signature. In mouse, the cluster forms in response to epithelial Shh signals (Walton et al. 2012). We hypothesize that epithelial ligands, Shh and PDGFA signal to their receptors in the underlying mesenchyme, leading to the cluster expression pattern. I find that when I culture E15 chick guts in the presence of an excess of Shh, thus abolishing a gradient of the ligand, cluster-specific expression is lost and instead expression is seen uniformly across the mesenchyme. Conversely, when cultured in the presence of cyclopamine, all expression of Ptc1 and Bmp4 is abolished (Figure 4.2). These data corroborate a recent study of the villus cluster in mouse and confirm that, in chick, Shh is upstream of Bmp4 and that a gradient of Shh is necessary to instigate a cluster of expression specific to the villus tip mesenchyme.

How such a uniform epithelial signal could induce this non-uniform mesenchymal pattern is a fascinating unanswered question. In a simple one-dimensional morphogentic field, cellular response is based on the distance between a cell and the morphogen source. When extending this model to two or three-dimensions, it is critical to consider that the shape of the source tissue can assume a non trivial role in how a signal is received. As the luminal pattern of the chick gut is transformed from ridges to zigzags to villi, the mesenchyme and overlying epithelium are driven to change their shape. Figure 4.3 shows, in cross section, the changes in shape seen in the epithelium and underlying

Figure 4.2. Shh is upstream of BMP4 in the villus cluster. *In situ hybridization* of E15 chick guts cultured for 36 hours. Normally, Shh is expressed uniformly throughout the mesenchyme and its receptor, and pathway target, Ptc as well as Bmp4 are expressed in a cluster under the tip of the pattern. Upon addition of Shh, the localized signal is lost and both Ptc and Bmp4 are expressed throughout the underlying mesenchyme. When cultured in the presence of cyclopamine, expression of both Ptc1 and Bmp4 are is lost.

Figure 4.2 (Continued)

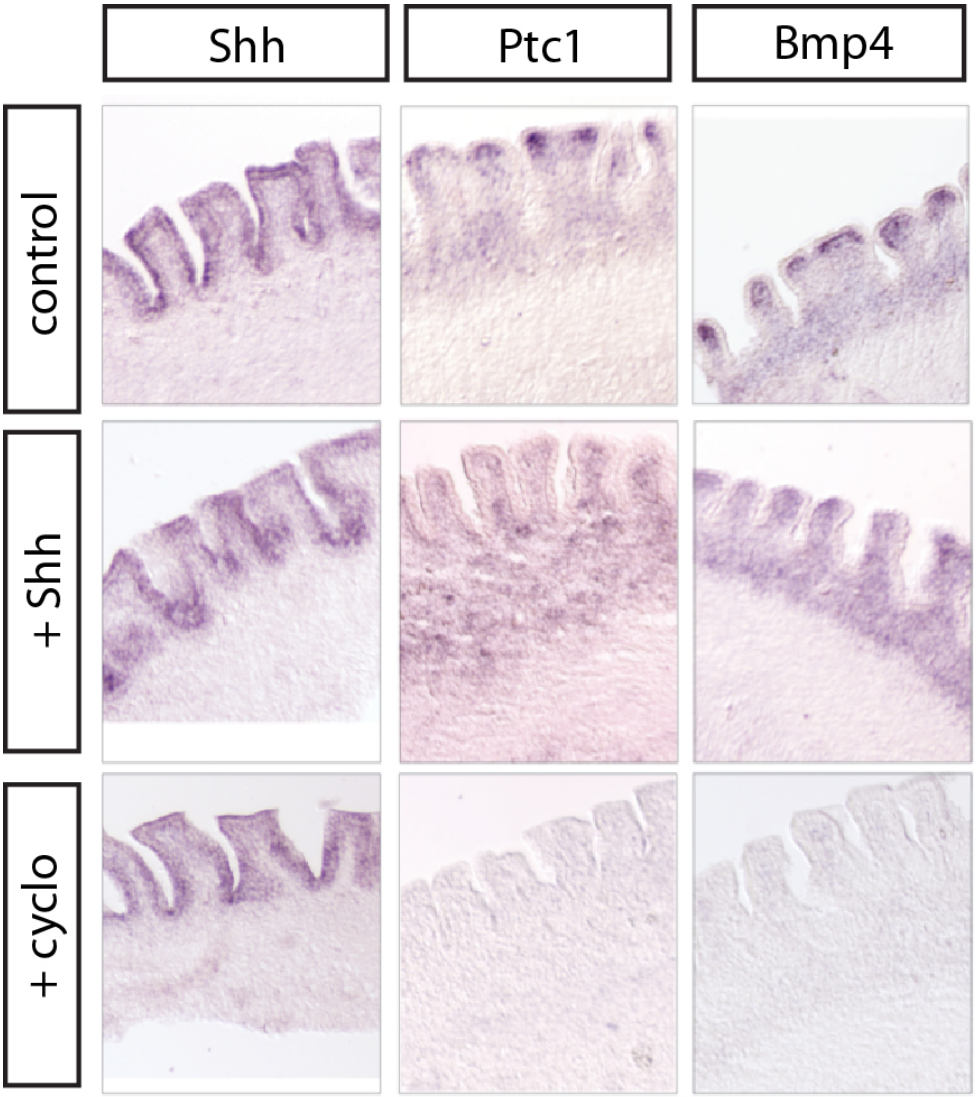

mesenchyme as the zigzags condense, enlarge, and flatten from E13 to E15. We hypothesize that the shape of the overlying epithelium determines how the mesenchyme receives and interprets signals. I designed a simple model to simulate the patterns that could occur when a morphogen defuses in a gradient from the various shapes of epithelia seen in our system. The model predicts a pattern of expression in the mesenchyme that changes from a region of expression directly under the epithelium of a wide flat zigzag to a filled-in pattern in the narrow, tall zigzag (Figure 4.3). The expression pattern of PDGFRα, a gene known to be expressed in the cluster, closely aligns with these predictions (Figure 4.3). Additional genes known to be expressed in the cluster such as Bmp4 and Ptc1 as well as Foxf1 also align with these predicted expression pattern over time (Figure 4.4). In the finger-like cross section seen just before definitive villi emerge, the epithelial layer encapsulates the responding mesenchymal cells. Interestingly, due to the finger-like shape and relatively small size of the domain, mesenchymal cells may receive signal from more than one point along the epithelium leading to the potential for an additive effect of the signal. This additive effect would lead to a density of signal at the villus tip, where cells are receiving signal from multiple directions. This pattern can be seen both in the model and in the corresponding *in situs*. Our model provides an explanation for the how a localized mesenchymal signal such as the villus cluster could arise in spite of the fact that the overlying epithelium is secreting a signal uniformly.

To test the role of the epithelial shape in articulating signals to the underlying mesenchyme, I manipulated the shape of the epithelium and assayed the resulting expression patterns. I altered the shape of the tissue by slicing the E15 gut tube into rings

Figure 4.3. The shape of the overlying epithelium determines how the mesenchyme receives and interprets signals. Top, Changes in shape seen in the epithelium and underlying mesenchyme as the zigzags condense, enlarge, and flatten from E13 to E15**.** Middle, A simple model to simulate the mesenchymal expression patterns that could occur when a morphogen defuses in a gradient from the various shapes of epithelia seen in our system. The outline of the epithelium in cross-section is lined with points, each with a radial decrease in color intensity, simulating diffusion of a morphogen from the epithelium. The darker regions represent higher levels of signal from the epithelium. Bottom, The simulated patterns closely mimic the expression patterns of the cluster gene PDGFR-α from E13 to E14. Images shown are *in situ hybridizations* performed on transverse sections.

Figure 4.3 (Continued)

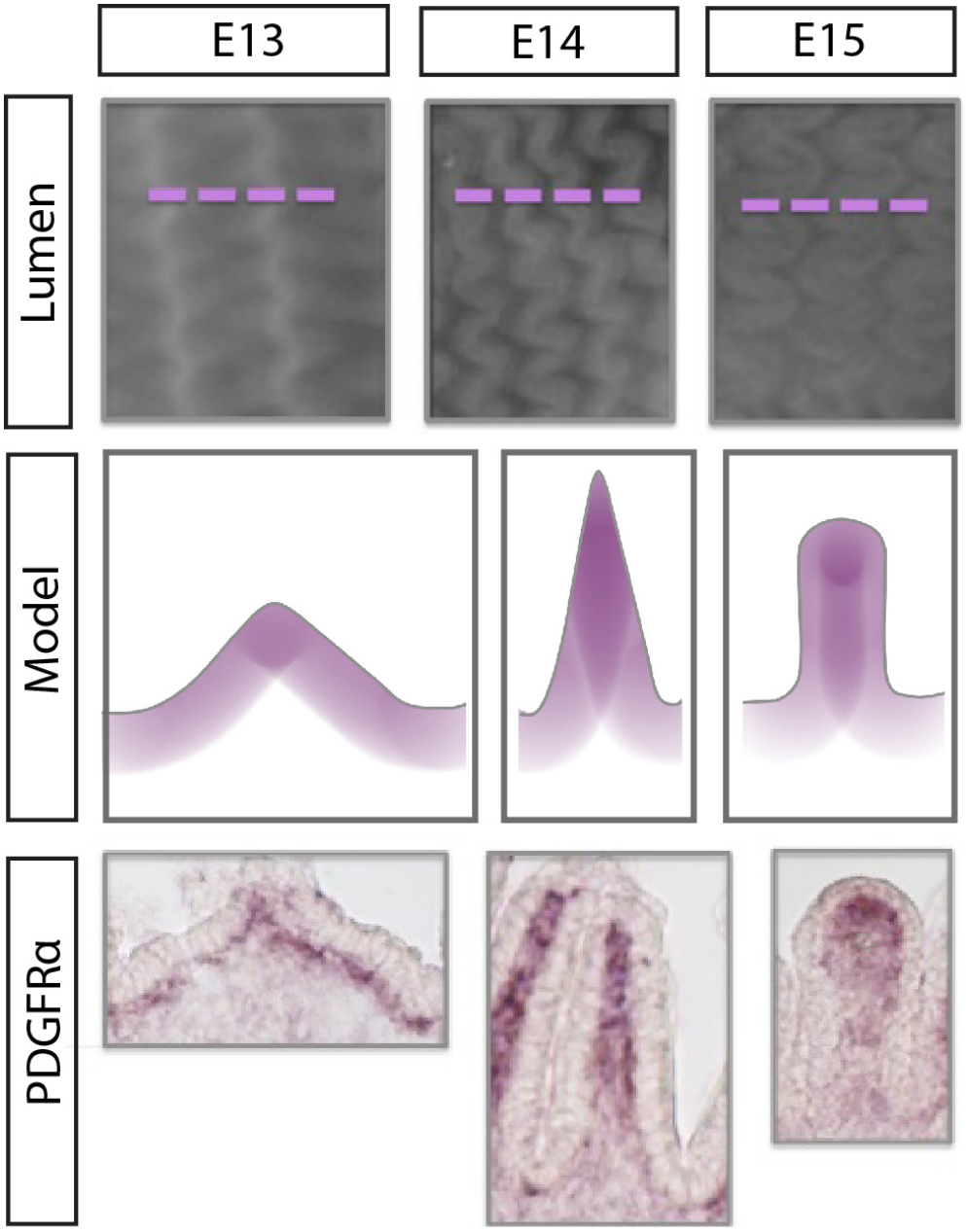

Figure 4.4. Cluster genes also align with predicted expression patterns. Shh is expressed throughout the epithelium. The expression of Ptc2, Bmp4, Foxf1, and PDGFR-α align with the predictions of our model: a pattern of expression in the mesenchyme that changes from a region of expression directly under the epithelium of a wide flat zigzag (left) to a filled in pattern in the narrow, tall zigzag (middle) to a cluster of signal at the tip of the luminal pattern (right). Images shown are *in situ* hybridizations performed on transverse sections.

Figure 4.4 (Continued)

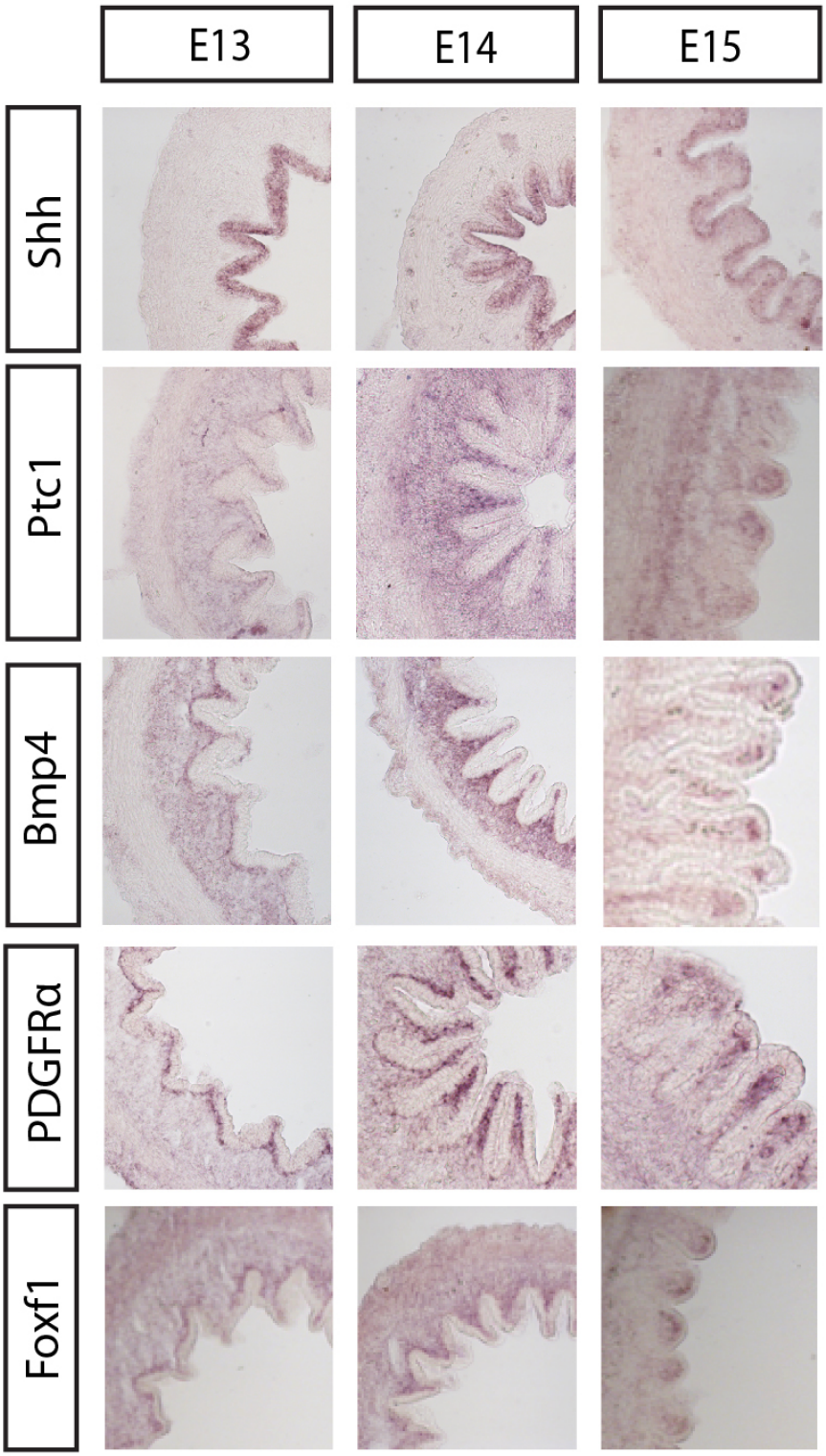

and then flipping these rings inside out changing the luminal topography from a narrow or rounded peak to a wider ridge (Figure 4.5). I then culture these inside out rings for 36 hours. When done at E14 or E15 the expression pattern in the inside out tissue reverts back to the pattern normally seen the wider peaks of E13 guts, with expression tracing the area just under the epithelium. These results support our hypothesis that epithelial shape determines the nature of the mesenchymal expression patterns, such as the villus cluster, through the articulation of signal gradients.

The loss of the cluster in these inside out experiments would predict a return to uniform proliferation in the epithelium, as repression from the cluster would be eliminated. Indeed, I find that proliferation in the inside out epithelium resembles that of an E13 gut with uniform epithelial Edu staining, whereas control guts show proliferation still excluded from the tips (Figure 4.6). I have developed a complimentary assay to turn an earlier, E10 ridge-stage gut into one with villi-like protrusions by culturing the guts against a fine mesh (Figure 4.7). I find that while the control samples from E10 guts maintain even proliferation throughout the epithelium, proliferation is lost in tips of these artificially induced villi (Figure 4.7). Together these results suggest the villus cluster restricts proliferation of the surrounding epithelium.

We hypothesize that proliferation is restricted through repression of epithelial Wnt signal, as canonical Wnt in the gut is so closely tied to proliferation, and because previous data points to Shh, and its downstream mesenchymal factors such as BMP4 and Foxf1, as negative regulators of canonical Wnt signal mouse in the developing intestine (Madison et al. 2005, Ormestad et al. 2005). I have assayed for expression of CD44v6, a variant isoform of CD44 and a known target of canonical Wnt, in mouse intestines over

Figure 4.5. The role of the epithelial shape in articulating signals to the underlying mesenchyme. Top left, E15 chick gut before and after being manually turned inside out. Top right, Control and inside out samples are cultured for 36 hours and assayed for cluster gene expression. Reverting the architecture back to a wide flat peak abolishes Bmp4 expression and returns expression to just under the epithlium. Bottom, expression patterns of additional cluster genes reveals similar results. Additionally, these data confirm Foxf1 is downstream of Shh signal from the epithelium as its expression is expanded in the presence of Shh and lost when cultured with cyclopamine (Bottom right). Again the topographically driven mesenchymal patterns are abolished when an excess of Shh, or cyclopamine interfere with the gradient from the epithelium. Images shown are *in situ* hybridizations performed on transverse sections.

Figure 4.5 (Continued)

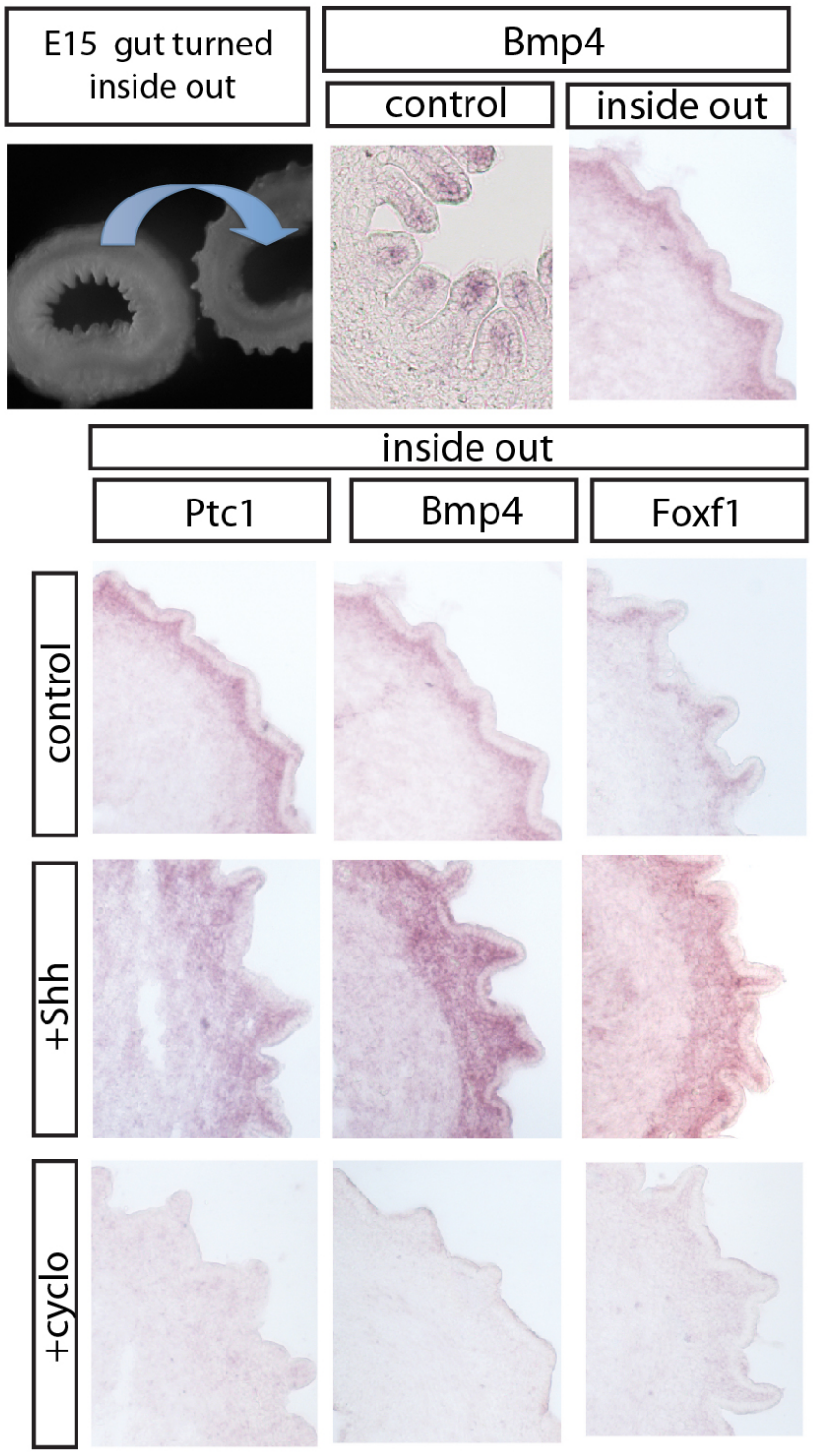

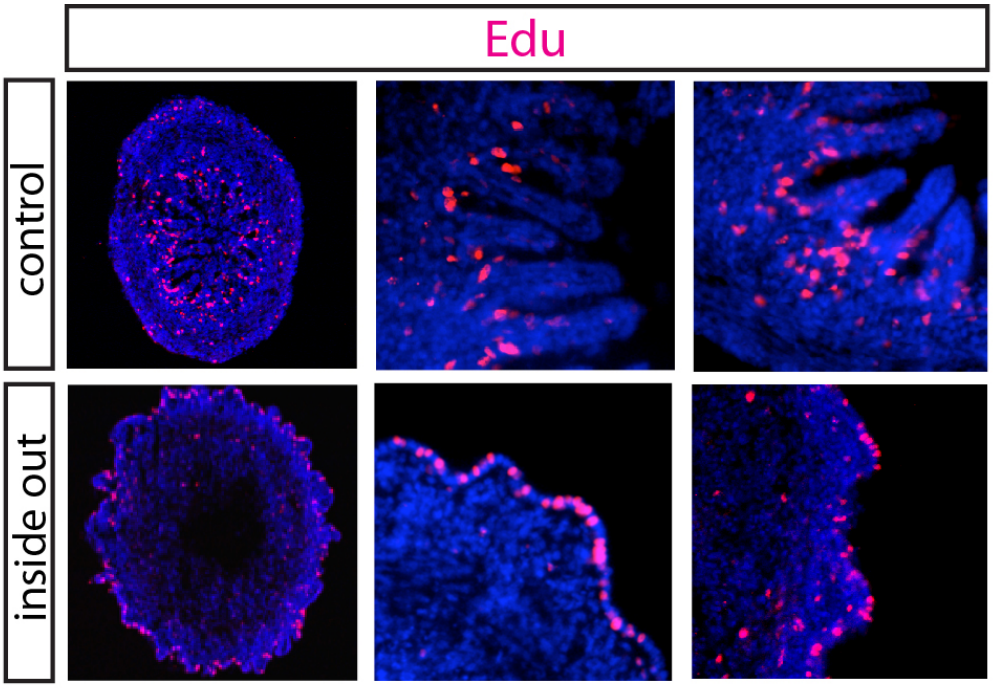

Figure 4.6. E15 inside out cultured guts show a return to uniform proliferation in the epithelium. E15 gut rings were cultured for 36 hours, either as normal rings (top) or after bring turned inside out (bottom). Proliferation in the inside-out epithelium resembles that of an E13 gut with relatively uniform epithelial Edu staining, whereas control guts show proliferation still excluded from the tip. Results are most clearly viewed in two close up samples on the right. Gut samples were cultured in 10μM Edu for four hours and Edu was detected on 14 μM transverse tissue sections

Figure 4.7. Proliferation is lost in tips of artificially induced villi. E10 gut samples were cultured for 36 hours, either as normal ridged tissue or under a fine mesh (schematized top left). Top, E10 ridge-stage guts cultured under the mesh form villi-like protrusions, seen in close-up (middle) and from the side (right). Control samples from E10 guts (left) maintain even proliferation throughout the epithelium, proliferation is lost in tips of these artificially induced villi (right). Gut samples were cultured in 10μM Edu for four hours and Edu was detected on 14 μM transverse tissue sections.

Figure 4.7 (Continued)

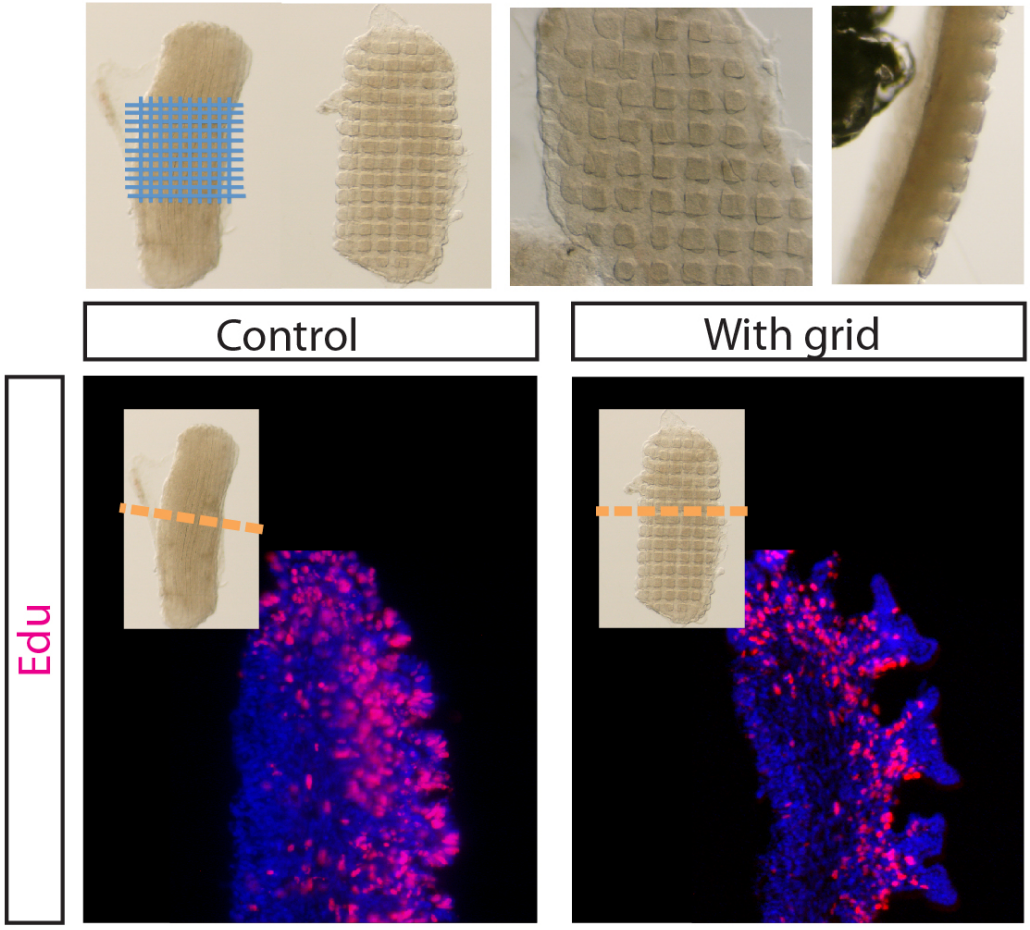

time and find that its expression is uniform initially, but is lost at villus tips just after the cluster forms, aligning with patterns of proliferation (Figure 4.8). Additionally because CD44v6 is also a known marker of ISCs, we speculate CD44v6-positive, cycling epithelial cells that are first found along the entire epithelium and then restricted to the base of the luminal pattern are a protected population of progenitors from which adult ISCs arise. Therefore, to explore the hypothesis that adult ISCs can be thought of as preserved embryonic progenitors, we investigated whether additional components of the adult ISC signature are shared with the cycling cells of the developing gut. We have begun to investigate the embryonic expression of Lgr5 in the gut through single-molecule fluorescent *in situ* hybridization (FISH). Preliminarily we find Lgr5 is expressed at low levels throughout the epithelium of the developing chick gut (Figure 4.9). As expected, we find expression is limited to the forming crypt after hatching (Figure 4.9). We additionally confirmed the existence of Lgr5 transcripts through qPCR. Importantly we find expression of Lgr5 is expressed more highly in E12 endoderm than the E12 mesoderm of the same stage (Figure 4.9). Additionally, the transcript is expressed in samples of the whole gut during development, albeit at lower levels than those found at hatching. Thus, preliminarily, Lrg5 is expressed in the chick embryonic epithelium.

Future Directions and Discussion

The data shown here demonstrate that changes in the topography of the epithelium during the mechanically driven morphogenesis impact the manner in which signals defusing from the epithelium are received by the underlying mesenchyme. We show that non-uniform mesenchymal patterns of Ptc1, BMP4, Foxf1 and PDGFR-α in the villus cluster arise as a result of the shape of the overlying epithelium by changing the

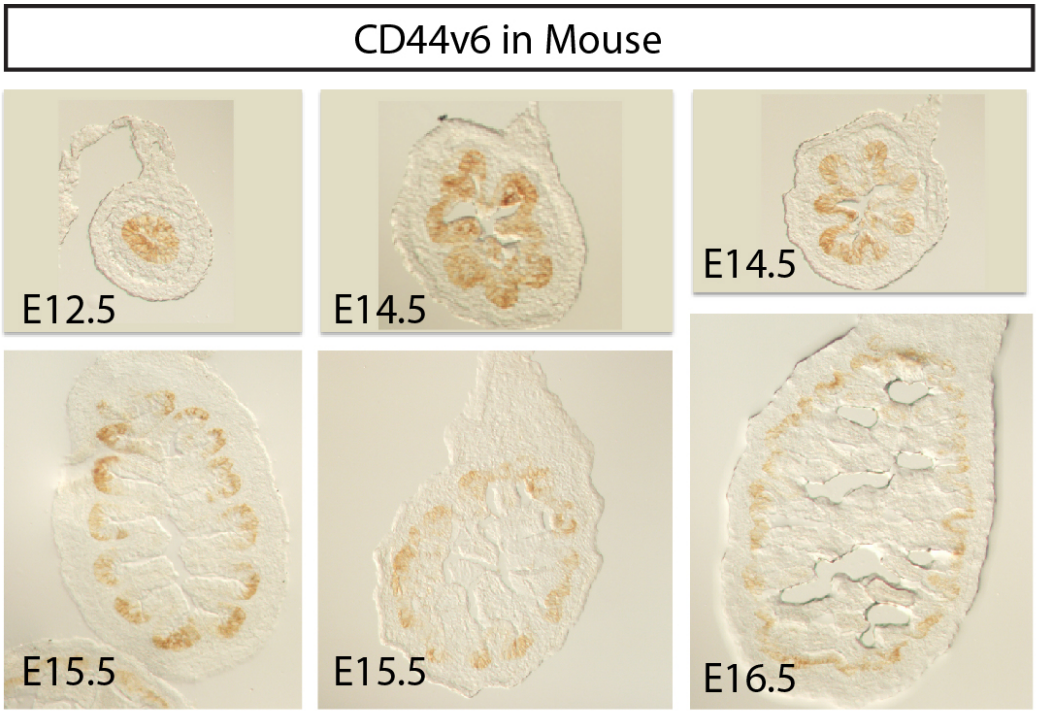

Figure 4.8. The Wnt target gene CD44v6 is expressed uniform initially, but is lost at villus tips just after the cluster forms in mouse. CD44v6 antibody staining of mouse intestines reveals its expression pattern mimics previously published proliferation patterns during development. In mouse the cluster forms at approximately e15.5, coinciding with the regression of both proliferation and CD44v6 to the intervillous region.

Figure 4.9. Lgr5 is expressed in the intestinal epithelium of the developing chick. Lgr5 expression is assayed by single-molecule fluorescence *in situ* hybridization (FISH). Lgr5 transcripts are found throughout the epithelium, and exclusively in the epithelium at E13 (green dots, top panels). Once the crypt forms after hatching, Lgr5 transcripts are specific to the crypt, as we would expect (green dots, bottom panels). qPCR of gut tissue shows Lgr5 is expressed more highly in the endoderm than in the mesenchyme at E13, confirming what we see in FISH experiments. Also, comparison of embryonic levels of Lrg5 in the whole gut tissue reveals Lgr5 is expressed at E15, and E18, albeit at lower levels than at hatching. qPCR data was normalized to β-actin.

Figure 4.9 (Continued)

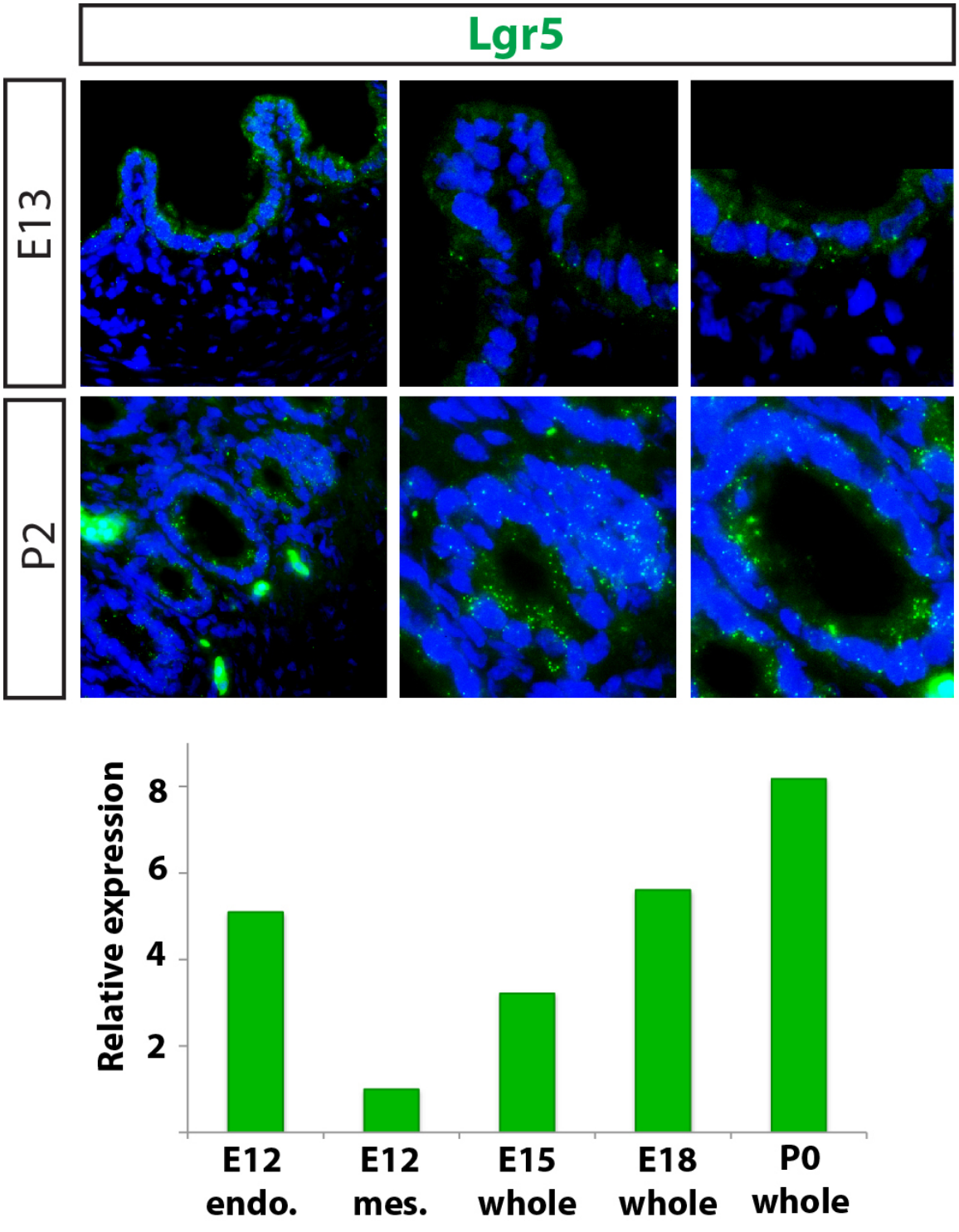

shape of the tissue and observing loss of the cluster expression pattern. While Ptc1 Bmp4, and Foxf1 are downstream of epithelial Shh, it is not known whether PDGF interacts with Shh signaling in the cluster, although previous reports suggest that PDGFR-α in the villus cluster is not downstream of Shh (Walton et al. 2012). Because Bmp expression appears more specific to the cluster than the Shh readout Ptc1, it seems likely an additional epithelial signal serves to refine this signal from Shh, leading to a more precise cluster pattern. Therefore, perhaps Shh acts in cooperation with a pathway such as PDGF to coordinate cluster expression. These questions regarding the dynamics of signaling in the villus cluster can be addressed in our *in vitro* system through the addition of recombinant proteins, agonists, and antagonists to guts grown in culture. Specifically we plan to culture E15 guts in the presence of cyclopamine to block Shh and Bmp inhibitors such as Noggin and assay for PDGFR-α expression. Additionally we'd like to culture guts in the presence of inhibitors of PDGF signal and query whether Bmp4 or Ptc expression is impacted.

The presence of the cluster appears necessary for restricting proliferation from the villus tip as loss of cluster signal in experiments where gut segments are turned inside out results in a return of proliferation to the peaks of the pattern. We aim to test our prediction that culturing E15 gut segments in the presence of antagonists of Shh or antagonists of downstream BMP would similarly return proliferation to the peaks of the pattern as cluster driven restriction or proliferation would be abolished. Additionally, artificially inducing a tissue topography which would induce a cluster signal results in loss of proliferation in the overlying epithelium. We aim to confirm whether this manipulation of the tissue induces a cluster signal where there was not one previously.

We will also apply cluster signal agonists as well as antagonists and observe the impact on proliferation patterns in artificial villi to confirm that Shh and downstream factors in the cluster inhibit neighboring proliferation. Our hypothesis would predict that addition of cyclopamine to artificially induced villi would return proliferation to the tips of the pattern.

Lastly, we are exploring the location of ISC markers during intestinal development. We find that, in mouse, CD44 is initially expressed uniformly in the epithelium and is progressively confined to the intervillous space, aligning with patterns of proliferation. As CD44 is a target of Wnt, which is repressed by cluster signals, Wnt signals are likely to be responsible for the regression of CD44 from the villous tips. We predict the same pattern exists in the developing chick intestine and are assaying expression of CD44 and additional Wnt targets in the chick. Additionally, it will be interesting to confirm our hypothesis that the regression of Wnt targets from the villous tip is cluster-driven. To do so, we can culture guts in the presence of Shh and BMP antagonists and assay for expression of CD44. We expect inhibiting hedgehog or BMP will prevent CD44 from being restricted from the tips of the tissue. Additionally, we aim to assay CD44 and expression of other Wnt target genes in guts that have been turned inside out guts with artificially induced protrusions. We anticipate the guts grown inside out will not restrict CD44 from the tips of the tissue and E10 guts forced to form protrusions through application of a grid will prematurely restrict proliferation from the tips of the artificial villi.

Preliminarily, we find that Lgr5 is expressed embryonically, first uniformly in the epithelium and later restricted to the crypt, therefore aligning with proliferation and Wnt

targets. This finding supports the existence of an embryonic progenitor pool that shares molecular and cellular features with adult ISCs. Further, resemblance of the embryonic progenitors to ISCs supports the hypothesis that ISCs arise, after birth, from the embryonic progenitor pool. Lgr5 is expressed at relatively low levels, even in the cells of the crypt, making this transcript difficult to detect through traditional methods, however, further characterization of Lgr5 expression through single-molecule FISH will be carried out. Lastly, if Lgr5 expression profiles emulate that of proliferation, it will be important to investigate whether Shh and downstream Bmp and Foxf1 are upstream of Lrg5 expression. This can be accomplished by assaying for Lgr5 expression using single-molecule FISH in guts cultured in the in presence of Shh and Bmp antagonists proposed above.

Stem cells in the adult maintain and repair tissues throughout the life of an organism. These cells retain the capacity to self-replicate and give rise to multiple cell types. Understanding the ontogeny of ISCs may shed light on how they are programmed into such uniquely multipotent and long-lived adult cells. A grasp of how this cell type arises may provide insights into methods for inducing or manipulating ISC formation. While adult stem cells exist in many tissue types, established tissue-specific adult stem cell markers are rare, therefore the discovery of ISC markers like Lgr5 appoints the intestine an ideal system in which to explore the ontogeny of adult stem cells.

Materials and Methods:

Embryos and Dissections

Fertile chicken eggs (White Leghorn eggs) were obtained from commercial sources. All eggs were incubated at 37.5°C and staged according to Hamburger and Hamilton. Timed pregnant CD1 mice were obtained from Charles River.

Immunohistochemistry, Edu Staining, In situ hybridization, single-molecule FISH

Small intestines were collected from embryos at desired stages and fixed in 4% paraformaldehyde in PBS and embedded in OCT, allowing for 14μm transverse sections of the gut tube. Immunohistochemistry was performed with anti-CD44v6 (BMS145 eBioscience), 1:100, overnight at 4°C in PBS containing 0.1% Triton X-100, and detected with a standard DAB-IHC protocol. DAPI (molecular probes) was used 1:1000 as a nuclear counter stain. 1mM Edu (Invitrogen) was injected in ovo and embryos were harvested 4 hours post-injection. Edu was added to a final concentration of 100μM *in vitro* and samples were incubated for 4 hours. Edu was detected in sectioned tissue using the Click-iT Edu system (Invitrogen). In situ hybridizations were performed as in Davis, Kurpios et al. 2008, DIG-labeled probes were detected with NBT/BCIP (Sigma). Single-molecule FISH experiments were carried out as previously described (Itzkovitz et al. 2011) with Lgr5 probes purchased from Biosearch Technologies.

Organ Culture

Intestines were dissected from the embryos of the desired stage in cold PBS, connective tissue was removed, and intestines were gently placed on transwells (Costar 3428) in DMEM media supplemented with 1% pen/strep and 10% Chick Embryonic Extract (for

chick tissue only). Intestines were cultured for 36 hours, or as indicated, at 37 °C with 5% CO_2.

***In vitro* tissue manipulations**

In order to invert the E15 gut into the inside out conformation, I cut thin rings of tissue (approximately 150 to 200 μm in thickness) and encourage the ring of gut to invert with forceps. As the inner circumference is longer than the outer one, leading to residual strain in the tissue, the tissue prefers the inside out conformation, and so inversion is not difficult. To induce artificial villi, I dissect E10 gut segments, slice them lengthwise to open the tube and place them lumen-side-up on a transwell filter. Then I place a fine mesh over the surface of the tissue. No added pressure is needed to induce protrusions. The filter is removed after 36 hours in culture when the sample is collected and fixed.

References

Barker, N. *et al*. Identification of stem cells in small intestine and colon by marker gene Lgr5. *Nature* **449**, 1003-1007 (2007).

Barker, N., van Oudenaarden, A. & Clevers, H. Identifying the stem cell of the intestinal crypt: strategies and pitfalls. *Cell. Stem Cell.* **11**, 452-460 (2012).

Crosnier, C., Stamataki, D. & Lewis, J. Organizing cell renewal in the intestine: stem cells, signals and combinatorial control. *Nat. Rev. Genet.* **7**, 349-359 (2006).

Haramis, A. P. *et al*. De novo crypt formation and juvenile polyposis on BMP inhibition in mouse intestine. *Science* **303**, 1684-1686 (2004).

He, X. C. *et al*. BMP signaling inhibits intestinal stem cell self-renewal through suppression of Wnt-beta-catenin signaling. *Nat. Genet.* **36**, 1117-1121 (2004).

Itzkovitz, S. *et al*. Single-molecule transcript counting of stem-cell markers in the mouse intestine. *Nat. Cell Biol.* **14**, 106-114 (2011).

Karlsson, L., Lindahl, P., Heath, J. K. & Betsholtz, C. Abnormal gastrointestinal development in PDGF-A and PDGFR-(alpha) deficient mice implicates a novel mesenchymal structure with putative instructive properties in villus morphogenesis. *Development* **127**, 3457-3466 (2000).

Kim, B. M., Mao, J., Taketo, M. M. & Shivdasani, R. A. Phases of canonical Wnt signaling during the development of mouse intestinal epithelium. *Gastroenterology* **133**, 529-538 (2007).

Korinek, V. *et al*. Depletion of epithelial stem-cell compartments in the small intestine of mice lacking Tcf-4. *Nat. Genet.* **19**, 379-383 (1998).

Korinek, V. *et al*. Two members of the Tcf family implicated in Wnt/beta-catenin signaling during embryogenesis in the mouse. *Mol. Cell. Biol.* **18**, 1248-1256 (1998).

Kosinski, C. *et al*. Indian hedgehog regulates intestinal stem cell fate through epithelial-mesenchymal interactions during development. *Gastroenterology* **139**, 893-903 (2010).

Madison, B. B. *et al*. Epithelial hedgehog signals pattern the intestinal crypt-villus axis. *Development* **132**, 279-289 (2005).

Mahoney, Z. X., Stappenbeck, T. S. & Miner, J. H. Laminin alpha 5 influences the architecture of the mouse small intestine mucosa. *J. Cell. Sci.* **121**, 2493-2502 (2008).

Noah, T. K., Donahue, B. & Shroyer, N. F. Intestinal development and differentiation. *Exp. Cell Res.* **317**, 2702-2710 (2011).

Ormestad, M. *et al*. Foxf1 and Foxf2 control murine gut development by limiting mesenchymal Wnt signaling and promoting extracellular matrix production. *Development* **133**, 833-843 (2006).

Ramalho-Santos, M., Melton, D. A. & McMahon, A. P. Hedgehog signals regulate multiple aspects of gastrointestinal development. *Development* **127**, 2763-2772 (2000).

Sato, T. *et al*. Single Lgr5 stem cells build crypt-villus structures in vitro without a mesenchymal niche. *Nature* **459**, 262-265 (2009).

Spence, J. R., Lauf, R. & Shroyer, N. F. Vertebrate intestinal endoderm development. *Dev. Dyn.* **240**, 501-520 (2011).

Sun, G. *et al*. Spatio-temporal expression profile of stem cell-associated gene LGR5 in the intestine during thyroid hormone-dependent metamorphosis in Xenopus laevis. *PLoS One* **5**, e13605 (2010).

Takashima, S., Gold, D. & Hartenstein, V. Stem cells and lineages of the intestine: a developmental and evolutionary perspective. *Dev. Genes Evol.* **223**, 85-102 (2013).

Takashima, S. & Hartenstein, V. Genetic control of intestinal stem cell specification and development: a comparative view. *Stem Cell. Rev.* **8**, 597-608 (2012).

van Es, J. H. *et al*. A critical role for the Wnt effector Tcf4 in adult intestinal homeostatic self-renewal. *Mol. Cell. Biol.* **32**, 1918-1927 (2012).

Wielenga, V. J. *et al*. Expression of CD44 in Apc and Tcf mutant mice implies regulation by the WNT pathway. *Am. J. Pathol.* **154**, 515-523 (1999).

Chapter Five

Concluding Discussion

The biophysical basis of loop and villi morphogenesis

The vertebrate intestine acts as the main site for nutrient absorption in the body. The surface area of the luminal lining of the tube is maximized in order to optimize intestinal function. One way to boost surface area is to increase the length of the tube, however, the size of the organ is restricted by the space allotted for it in the body cavity. Therefore, folding the tube into a series of loops allows a longer intestine to maintain a compact form. Alternatively, modifying the luminal topography can dramatically increase surface area without increasing the size of the organ. Thus, investigating how the intestine forms loops and builds luminal topographies is key to understanding its how a functional organ develops. Further, understanding the mechanisms driving these patterning events will give a clearer picture of how variation in patterns may have developed across species.

Using a combination of biological experiments, physical models, theory, and quantitative simulations, we demonstrate that the vertebrate gut forms loops as a result of homogeneous and isotropic forces that arise from the relative growth between the gut tube and the anchoring dorsal mesenteric sheet, tissues that grow at different rates. We developed a computational model and validated its predictive ability in chick as well as in other bird species and in mouse. Importantly looping pattern depends upon a simple set of parameters: geometry, growth rate, and physical properties. We speculate these are the minimal properties upon which selection has acted to achieve the diversity of looping patterns found in nature.

This same set of parameters is responsible for the diversity of luminal patterns explored in our studies of villi formation. We find intestinal villi form in a stepwise

process as a result of physical forces generated as proliferating endodermal and mesenchymal tissues are constrained by sequentially differentiating layers of smooth muscle. Our study reveals that relatively minor changes in the growth, physical properties, and geometry of the developing tissue in various species can dramatically alter the process of villi formation, or final pattern formed. Again, we speculate these properties are an elegantly simple set of parameters which can be tuned in nature to drive variation.

Because the same parameters underlie the outcomes of both loop and villi formation, and because loops and villi form simultaneously and conspire to increase surface area it is important to consider the formation of these two patterns together. It is interesting to consider that the embryo may simply exploit basic mechanical properties of the tissue, optimizing gut size and luminal morphology in concert to form the most morphologically adapted intestine. For example, as discussed in Chapter 4, the inner longitudinal muscle layer concurrently restricts the tube length and increases luminal surface by driving the formation of villi. As this layer does not form in frog, we speculate that it arose in higher vertebrates, optimizing gut function through changing both gut length and luminal surface pattern simultaneously.

Further, in our interspecies comparisons of the formation of both loops and villi, we find that differences in physical properties between mouse and chick define the divergence of their patters. Specifically, the gut tube in mouse is much softer than that in chick leading to a more tightly looped gut. Similarly, our computational modeling reveals that the softer mouse endoderm is responsible for the direct formation of an array of villi rather than ridge or zigzag intermediates. Therefore, in this instance, interspecies

variation of both looping and villi patterns centers on the difference in stiffness between the species. It would be interesting to explore whether this difference in stiffness is consistent throughout other developing tissues and whether it similarly contributes to interspecies variation in other organs.

The biomechanical basis of pattern formation we describe should be explored at a molecular and cellular level as mechanical properties of the tissue are derived from the molecular make up of the cells and tissue layers. Since tissue stiffness plays such a central role in pattern formation and defines differences in pattern between species, it will be important to explore the molecular root of these differences. Assaying for levels and localization of known adhesion molecules, cytoskeletal elements as well as components of the basal lamina, which underlies the epithelium, in chick versus mouse would allow us to explore the basis of a softer endoderm in mouse.

A more directed approach would be to mine for mouse mutants of these same molecular components which present with altered villi morphology. In fact, mice lacking the basal lamina component laminin 5α exhibit alterations in mucosal architecture that resemble zigzags (Mahoney et al. 2005). The loss of laminin 5α is said to potentially increase the stiffness of the lamina and endoderm through compensatory mechanisms. It would be fascinating to pursue whether this laminin 5α knockout mouse reverts to an embryonic chick luminal topography because of changes in epithelial stiffness. We have developed the tools to measure tissue layer stiffness and could therefore verify that loss of laminin 5α leads to a stiffer endoderm. Further, we could manipulate expression of laminins or similar molecules in chick though *in ovo* and *in vitro* studies with the aim of inducing a softer endoderm and mimicking mouse-like villi formation. These studies

would deepen our understanding of the molecular basis of physical properties that govern luminal architecture. Lastly, it would be interesting to examine whether these mutant mice display any looping phenotypes, as we might expect if the stiffness of the gut is altered.

The biomechanical mechanisms we provide for how loops and villi form allow for directed follow up studies of genetic underpinnings of differences in growth, geometry, and physical properties between species. A comparison of chick and quail looping would allow for an investigation of the genetic basis of the difference in pattern between these closely related species. We find that, although growth strains are similar between the chick and quail, the quail mesentery has a tension approximately five times that in the chick mesentery. Qualitatively, this greater elastic force produces a smaller loop, hence inducing more loops per length and thus the same number of loops in the smaller bird. With this mechanical understanding in hand, we can explore the genetic basis behind the interspecies differences in pattern by specifically pursuing the molecular mechanisms of a thinner mesentery in chick.

Although both looping and villi provide opportunity for added surface area, there may be instances where modifying one pattern may be more advantageous than the other. For example flying vertebrates, especially those that migrate, are known to possess shorter guts than comparable, similarly sized non-flying animals. A shorter gut tube is required because the energetic costs of flight increase with load carried. Therefore these species must achieve the same nutrient absorption in a shorter tube (Caviedes-Vidal et al. 2007). While this can be achieved through molecular and cellular adaptations of the epithelium, a more elaborate luminal surface is also said to play a compensatory role in

this case (Lavin et al. 2008). Further, Elasmobranchs such as the skate and shark have short, unlooped intestines, potentially due to an underdeveloped mesentery, but maintain a significant surface area due to elaborate infolding of the inner surface of the intestine (Wilson et al. 2010, Chatchavalvanich et al. 2006). Therefore in the absence of a mechanism allowing for a longer gut to be folded into the body, these species appear to have evolved elaborate luminal strictures to maximize the surface area of a shorter gut.

Certainly, the final length of the villus dramatically impacts the surface area it contributes. However, while the number of villi is patterned by biomechanical mechanisms, how the length of villi is determined is not understood. While longer villi provide greater surface area, structural limitations must constrain the final height possible. It will be interesting to pursue how villi continue to elongate after the initial villi pattern is set. Once the pattern of villi is set just before hatching, separation of the endoderm from the mesenchme does not abolish the villi pattern suggesting at the stage when villi elongate, the tissue layers are no longer interacting in an elastic way to direct morphogenesis. Instead, proliferating cells at the base of villi may force growth upward to encourage outgrowth, or cells may migrate in the direction of elongation as villi grow.

In Chapter Four, I demonstrate that proliferation is restricted to the base of the pattern as a result of repressive signals from a the villus cluster, a mesenchymal signaling center. Interestingly, the villus cluster arises as the zigzag topography changes from E13 to E15, repressing proliferation at the tips of the pattern just before villi form. According to our quantitative modeling, this non-uniform proliferation pattern is an important part of delineating individual villi. Therefore, the mechanically-driven remodeling of the luminal pattern leads to a change in signaling, altering the pattern of proliferation, which

feeds back on the luminal architecture leading to the formation of villi from zigzags. This mechanism is a fascinating example of the interplay between mechanical forces, morphogenesis, molecular cues, and cellular behaviors such as proliferation during development. Further, this is an important example of an instance where a change in shape of the tissue alters signals rather than signals leading to changes in shape. Therefore, in this case, patterning follows morphogenesis rather than the more canonical reverse scenario.

The role of epithelial architecture in signal articulation and patterning

The villus cluster not only plays a role in villus formation, but may also direct the process by which intestinal stem cells are ultimately localized to the base of each villus. We demonstrate the cluster inhibits proliferation in neighboring cells protecting a pool of embryonic progenitors in the region near the prospective niche.

While this signal mechanism has not been previously implicated in morphogenesis, changing epithelial architecture is likely to play an important role in signal articulation on other settings. This mechanism seems most likely to be important when patterning is performed on a small scale where epithelial signals have the potential to overlap in a pocket of underlying mesenchyme. One example of a setting where epithelial shape may be important is in the formation of epithelial placodes. In chick, feather placodes arise as evenly spaced elements, first as ectodermal thickenings and then instigating mesenchymal condensation (Reviewed in Wolpert et al. 1998). Interactions between the ectoderm-derived epithelium and underlying mesenchyme are known to be essential for proper patterning but to what extent these interactions depend on the

changing shape of the epithelium has not been explored (Mckinnel et al. 2004). It seems possible, as the villi-shaped placode elongates, a cluster-like expression domain forms in the mesenchyme and influences the neighboring ectoderm.

It would also be interesting to pursue local epithelial shape changes in the context of branching morphogenesis. This process often involves small pockets of mesenchymal tissue surrounded by an epithelium, as is the case in forming villi. In the developing mouse lung, as a branch forms, signals are located to the forming tip, and this may be due to signaling dynamics within this epithelial architecture (Lebeche et al. 1999). These localized signals are essential for proper branching, and interestingly, involve many of the same pathways utilized in sculpting villi and placodes (Warburton et al. 2000).

We investigated the cellular and molecular similarities between embryonic progenitors and adult ISCs. Preliminarily, we find that these cells express targets of canonical Wnt signal and Lgr5, both components of the ISC signature. Further study is required to uncover the ontogeny of ISCs but our studies thus far point to an embryonic origin. Although our data suggests Lgr5 is expressed embryonically, our findings also point to lower levels of expression per cell in the embryonic epithelium than in the adult crypt. This increase in expression may be driven by thyroid hormone (T3) at hatching in chick and birth in mouse as is the case during metamorphosis in *Xenopus* (Sun et al. 2010). We speculate that endogenous T3, which does spike near hatching, or alternative factors, induce higher levels of Lgr5 in the intervillous region where the gene is already expressed (Lu et al 2007). Further, a neonatal increase in signal does not conflict with an embryonic origin for ISCs, and in fact T3 induction at birth alone could not account for the localized expression of Lgr5 seen at birth.

Perhaps an embryonic origin for ISCs is not suspiring given the similarity of the roles ISCs and embryonic progenitors play in their relative contexts: embryonic progenitors proliferate and populate the epithelium as it forms just as in the adult ISCs serve to replenish the gut as it is injured and shed during homeostasis. Assaying embryonic expression of Lgr5 may deepen our understanding of its function in adult ISCs. Additionally, it will be interesting to explore the expression pattern of the additional factors that compose the ISC signature. While the presence of these markers in the embryo would strengthen our hypothesis that ISCs share features with embryonic progenitors, because these markers behave differently during injury an disease, it is also possible they will have different embryonic profiles (Iztkovitz et al. 2011).

Reflecting on the similarities between embryonic progenitors and adult ISCs allows for comparison of intestinal development and regeneration. The parallels between these two processes are far reaching and, often what we know of one is used to aid in our understanding of the other. It will be particularly interesting to utilize what we learn about the differences and similarities of embryonic progenitors and adult ISCs in studies aimed at understanding how ISCs are programmed.

Summary

In conclusion, my dissertation studies have shown that looping morphogenesis is driven by mechanical forces that arise from differential growth between the gut tube and the anchoring dorsal mesenteric sheet. A computational model based on measured parameters not only quantitatively predicts the looping pattern in chick, verifying that

these physical forces are sufficient to explain the process, but also accounts for the variation in the gut looping patterns seen in other species.

Second, I find that intestinal villi form in a stepwise process as a result of physical forces generated as proliferating endodermal and mesenchymal tissues are constrained by sequentially differentiating layers of smooth muscle. A computational model incorporating measured differential growth and the geometric and physical properties of the developing chick gut recapitulates the morphological patterns seen during chick villi formation. I also demonstrate that the same basic biophysical processes underlie the formation of intestinal folds in frog and villi in mice.

Finally, I show that as the tissue architecture is morphed by mechanical forces during villi formation, epithelial signals communicated to the underlying mesenchyme shift, resulting in a localized, villus cluster signal. Signals from the cluster, in turn, feed back to restrict proliferating progenitors in the endoderm, the presumptive precursors of the stem cells, to the base of each villus. We assay for expression of ISC markers in the embryonic gut and find that embryonic progenitors resemble adult ISCs, suggesting ISCs may be remnants of this pool of embryonic progenitors

Together, these studies provide new insight into the formation of the small intestine as a functional organ and highlight the interplay between physical forces, tissue-level growth, and signaling during development.

References

Caviedes-Vidal, E. *et al*. The digestive adaptation of flying vertebrates: high intestinal paracellular absorption compensates for smaller guts. *Proc. Natl. Acad. Sci. U. S. A.* **104**, 19132-19137 (2007).

Chatchavalvanich, K., Marcos, R., Poonpirom, J., Thongpan, A. & Rocha, E. Histology of the digestive tract of the freshwater stingray Himantura signifer Compagno and Roberts, 1982 (Elasmobranchii, Dasyatidae). *Anat. Embryol. (Berl)* **211**, 507-518 (2006).

Itzkovitz, S., Blat, I. C., Jacks, T., Clevers, H. & van Oudenaarden, A. Optimality in the development of intestinal crypts. *Cell* **148**, 608-619 (2012).

Itzkovitz, S. *et al*. Single-molecule transcript counting of stem-cell markers in the mouse intestine. *Nat. Cell Biol.* **14**, 106-114 (2011).

Lavin, S. R., Karasov, W. H., Ives, A. R., Middleton, K. M. & Garland, T.,Jr. Morphometrics of the avian small intestine compared with that of nonflying mammals: a phylogenetic approach. *Physiol. Biochem. Zool.* **81**, 526-550 (2008).

Lebeche, D., Malpel, S. & Cardoso, W. V. Fibroblast growth factor interactions in the developing lung. *Mech. Dev.* **86**, 125-136 (1999).

Lu, J. W., McMurtry, J. P. & Coon, C. N. Developmental changes of plasma insulin, glucagon, insulin-like growth factors, thyroid hormones, and glucose concentrations in chick embryos and hatched chicks. *Poult. Sci.* **86**, 673-683 (2007).

Mahoney, Z. X., Stappenbeck, T. S. & Miner, J. H. Laminin alpha 5 influences the architecture of the mouse small intestine mucosa. *J. Cell. Sci.* **121**, 2493-2502 (2008).

Mandler, M. & Neubuser, A. FGF signaling is required for initiation of feather placode development. *Development* **131**, 3333-3343 (2004).

McKinnell, I. W., Turmaine, M. & Patel, K. Sonic Hedgehog functions by localizing the region of proliferation in early developing feather buds. *Dev. Biol.* **272**, 76-88 (2004).

Munoz, J. *et al*. The Lgr5 intestinal stem cell signature: robust expression of proposed quiescent '+4' cell markers. *EMBO J.* **31**, 3079-3091 (2012).

Sun, G. *et al*. Spatio-temporal expression profile of stem cell-associated gene LGR5 in the intestine during thyroid hormone-dependent metamorphosis in Xenopus laevis. *PLoS One* **5**, e13605 (2010).

Warburton, D. *et al*. The molecular basis of lung morphogenesis. *Mech. Dev.* **92**, 55-81 (2000).

Wolpert, L. Pattern formation in epithelial development: the vertebrate limb and feather bud spacing. *Philos. Trans. R. Soc. Lond. B. Biol. Sci.* **353**, 871-875 (1998).

Appendix I: Supplementary Information for On the Growth and Form of the Gut

Supplementary Information for "On the growth and form of the gut" by T. Savin et al.

Cell proliferation along the gut

To characterize cell proliferation in the gut, we used a mitotic marker (see the "Methods" section of the main text) and find that there is no asymmetric proliferation in cross sections of the gut at different positions along it as shown in Figure S1.

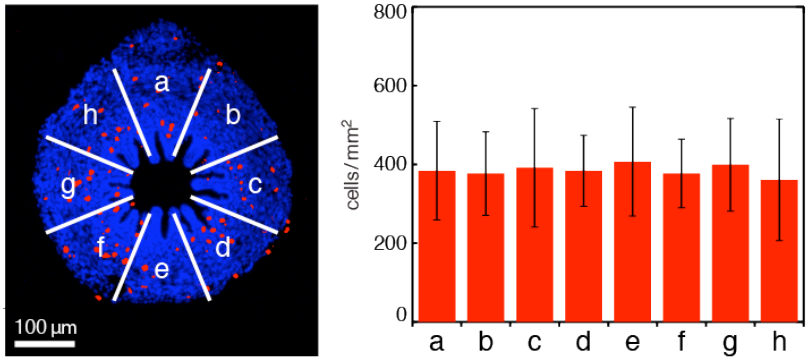

Figure S1 | Cell proliferation patterns in a cross-section of the tube at E12. Ten tube sections, stained for cell nuclei (blue) and mitosis (red), and extracted from approximately equidistant locations along the extent of the entire tube, were each divided into 8 equal slices labelled, as shown, such that the connection with the mesentery is at slice "a" (the "12 o'clock" position). The number of cells per unit area was extracted in each slice and averaged across the sections. We cannot detect different proliferation between the slices, thus validating the radial symmetry of tube growth.

Mesentery histology and thickness

Embryos were fixed in 4% paraformaldehyde and then dehydrated in a graded ethanol series, cleared in xylenes, and embedded in paraffin. Sections at 10 µm thickness were collected. Fast Green staining was performed using standard protocols: briefly, slides were dewaxed in xylenes, rinsed in successive washes with 100% and 95% ethanol, and rehydrated in tap water. Slides were then stained with Fast Green (Sigma Aldrich) for 30 minutes, rinsed in tap water, dehydrated, cleared in xylenes and sealed with DPX mountant (Fluka). Micrographs of these sections are shown in Figure S2 and were used to measure the mesentery thickness h reported in Figs. S9a to S11a.

Physical simulacrum of gut looping using rubber tubes and sheets

To mimic the differential strain induced by differential growth between the gut tube and the mesentery, we used a rubber membrane-strip that was stretched longitudinally and stitched to a naturally straight, unstretched rubber tube, and then allowed the composite to relax to equilibrium while preventing the ends from twisting or otherwise rotating. This preserves the topology of the composite system, puts the gut under compression and the membrane under tension, and leads to looping patterns identical to those seen in the real gut.

We cut wide strips of elastic rubber sheet (McMaster-Carr) of various dimensions (width $> 10\,\mathrm{cm}$, length about $1\,\mathrm{m}$, and thicknesses of $0.25, 0.4, 1$ and $1.3\,\mathrm{mm}$). An individual sheet was held stretched in one direction at the desired extension using clamps. For extension ratios up to 2, we verified that the mechanical response of the rubber is linear. Silicon rubber tubes of radii $r_i = r_o/2$, with $r_o = 4.77$ and $1.59\,\mathrm{mm}$ (NewAge Industries,

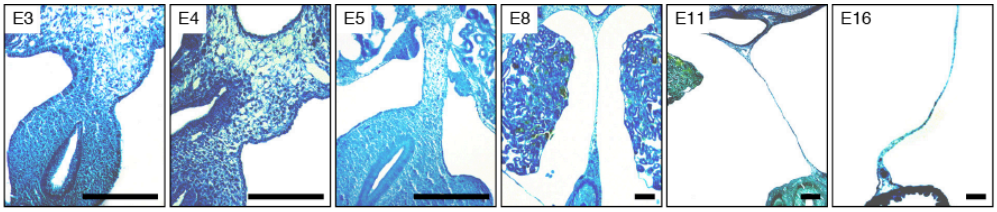

Figure S2 | Cellular morphology of the mesentery during gut development. The dorsal mesentery undergoes cellular rearrangement in the course of gut development during which the asymmetric cellular morphology first seen at E3 of embryonic development is lost and the mesentery consists of only few layers of mesothelium as seen in cross-section of the mature gut (E16). All scale bars represent 100 µm.

inc.), were stitched to the sheet using sewing thread. Upon relaxing the sheet, we observed the spontaneous formation of loops. We verified that the loop radius was always much smaller than the width of the sheet, and also much smaller than the natural radius of the tubes that is associated with residual strains from packaging/transportation, thus qualitatively similar to the real gut-mesentery system. The Young's modulus of the material of the sheets used to model the mesentery was $E_m = 1.3 \pm 0.2$ MPa and that of the tube was $E_t = 1.1 \pm 0.3$ MPa ; both were measured using simple extensional tests.

Admittedly the mesentery and the gut tube are microstructurally far more complex living materials than the simple latex and rubber used in the physical model. Yet, at the mesoscopic length scale of a loop that is much larger than that of local cellular or multicellular heterogeneities (e.g. vessels, collagen fibers) but smaller than the whole gut, these effects average out and allow us to isolate the essential mechanics of the formation of loops in terms of elastic forces driven by the strain mismatch arising from differential growth.

Calibration of magnetic bead force-extension curve

We used the attractive force between a permanent magnet and a millmeter size steel bead attached to the tissue to measure the mechanical properties of the gut and mesentery at different stages of development. This allowed us to apply forces in the $10^{-6} - 10^{-3}$ N range on millimetric biological samples and characterize the stress-strain relation of the tissues.

To calibrate the magnetic force vs. distance curve, we used the known resistance to motion of a steel ball (AISI 440C martensitic stainless steel, density $\rho_b = 7650\,\mathrm{kg\cdot m^{-3}}$, radius $r_b = 0.122$, 0.253 or 0.398 mm, ± 0.01 mm New England Miniature Ball Corp.) in pure glycerol (density $\rho_f = 1260\,\mathrm{kg\cdot m^{-3}}$, viscosity $\eta_f = 0.690$ Pa·s at 29°C). When the ball was placed at the tip of a conical support and a disc magnet (commercial grade, neodymium Nd-Fe-B, diameter $2r_m = 7.5$ mm, height 2.8 mm, nickel plated; The Magnet Source) was then brought above the bead (cylindrical edges facing the bead, vertical flat edges) we observed the motion of the ball which was recorded at 250 frames per second using a digital camera (PL-B781, PixeLINK) equipped with an objective that effectively magnified to 0.045 mm per pixel. All materials used to manipulate the beads and the magnet during the measurements had no magnetic susceptibility. Movies were then processed off-line using the IDL language (ITT Visual Information Solutions) to extract the position of the bead and of the magnet. We used a particle tracking package [?] to extract the bead trajectory. Tracking the magnet was performed by using image registration of a reference sub-array in each frames. The reference image was manually clipped from the initial frame to contain the intensity pattern of the feature (here, the magnet) to be tracked. It was then aligned in the remaining frames onto the "mobile" matching pattern by maximizing intensity correlation [?] These trajectory extraction methods offer a resolution that we estimated to be about 1/2 pixel, i.e. ≈ 20 µm.

To quantify the forces associated with this motion, we used the known analytic description of the dynamics of the steel ball in a viscous fluid [?],

$$\frac{4}{3}\pi r_b^3\left(\rho_b + \frac{\rho_f}{2}\right)\dot{v}(t) = F - 6\pi\eta_f r_b v(t) - \frac{4}{3}\pi r_b^3(\rho_b - \rho_f)g - 6r_b^2(\pi\eta_f\rho_f)^{1/2}\int_0^t \frac{\dot{v}(\tau)d\tau}{(t-\tau)^{1/2}},$$

where the rate of change of the momentum of the bead (left-hand side) is balanced by, in order of appearance in

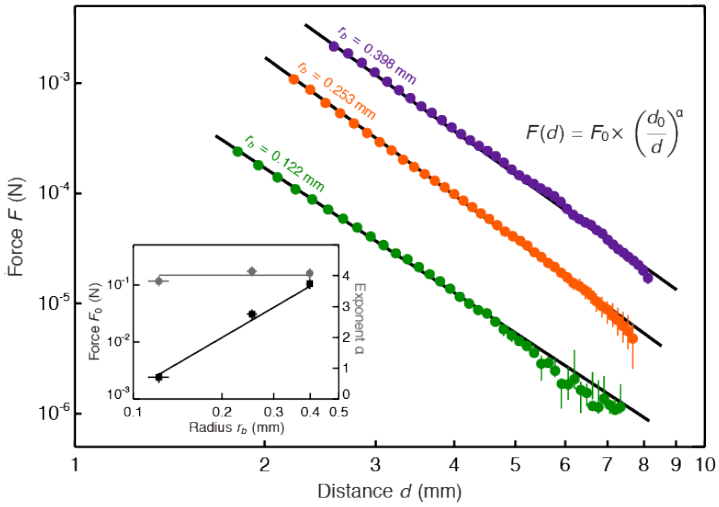

Figure S3 | Calibration of the magnet-bead force-displacement curve. The force vs. distance calibration curves for 3 different sizes of the steel magnetizable bead. The parameters for the power-law fit $F(d) = F_0(d/d_0)^{\alpha}$ are shown in inset; the force is shown on the left ordinate while the exponent is shown on the right.

the right-hand side: the magnetic force F (to be determined), the drag force, the weight, and the Boussinesq-Basset force. Here $v(t)$ and $\dot{v}(t)$ are respectively the velocity and acceleration of the bead at time t and $g = 9.81\,\mathrm{m \cdot s^{-2}}$ is the gravity [1]. We verified that the Reynolds number $\frac{\rho_f r_b v}{\eta_f} < 10^{-1}$ at all times, so that the fluid inertial contributions are small and can be neglected in the above equation. Then the magnetic force is balanced by the Stokes drag and gravity and can thus be measured from the bead trajectory as a function of the bead-magnet distance d, between the ball's center and the cylindrical edge of the magnet, and is shown in Figure S3. We find that over the range of distance $2 < d < 8\,\mathrm{mm}$, the force follows a power-law scaling $F(d) = F_0(d_0/d)^{\alpha}$, where we parametrize the power-law fit using the characteristic magnitude of the force $F_0 = F(d = d_0)$ at the characteristic distance $d_0 = 1\,\mathrm{mm}$. The results are summarized in table S1.

r_b	F_0	α
0.122 ± 0.010 mm	(2.40 ± 0.2) × 10^{-3} N	3.76 ± 0.2
0.253 ± 0.010 mm	(3.07 ± 0.3) × 10^{-2} N	4.16 ± 0.2
0.398 ± 0.010 mm	(1.05 ± 0.1) × 10^{-1} N	4.08 ± 0.2

Table S1 | Power-Law fitting parameters for the bead-magnet interaction force. We observe that the scaling follows closely $F \boxtimes r_b^3 d^{-4}$ (see inset of Fig S3).

We verified that the curves were reproducible for different beads of the same batch, and were unchanged wether or not the steel balls were in contact with the magnet prior to the masurement. Finally, we note that the bead-magnet distances at which the calibration was extracted are in the same range as in the tissue mechanics measurements explained below. Although the scaling for the magnetic force, which closely follows $F(d) \boxtimes r_b^3 d^{-4}$, seems in good agreement with the prediction for a magnetic point dipole interaction, this simple interpretation of the force curves is not applicable here for two reasons: first, the distances d investigated in the calibration curves of Figure S3 are comparable with the size of the magnet: $d \leq 2r_m$ and within this

[1] Note that the terms $6\pi\eta_f r_b v(t)$ and $\frac{4}{3}\pi r_b^3(\rho_b - \rho_f)g$ balances each other in free fall, $v(t) = v_\infty$. We performed this falling ball viscometer experiment separately. We recovered from v_∞ the tabulated viscosity of glycerol to within 8%.

range, the magnet cannot be approximated by a point dipole; second, the magnetization of the steel ball is field dependent, hence a function of d. A detailed study of the bead-magnet interaction force will be included in a forthcoming article [?].

Measurement of mechanical properties of gut and mesentery tissue

The "methods" section of the main text summarizes the protocol used to prepare the tissue samples for uniaxial tensile tests. The steel beads were either handled with aspiration pipettes or with tweezers, depending on their size and were inserted into the gut tube using these handlers. To attach the beads to the mesentery, they were first apposed to a paper tissue imbibed with glue and quickly deposited onto the membrane, which was held at the meniscus surface of the Ringer buffer (while still immersed). Our methods to attach the steel bead on the sample ensures that the applied force is uniformly distributed across the sample section that is perpendicular to the direction of the force. In particular, this is true for the dissected strip of mesentery thanks to the thinness of the tissue. We thus avoid significant complications arising when other fixation techniques must be used [?]. The preparation of tissue samples for tensile test is delicate; a systematic approach to the manipulation of the sample and the beads will be the subject of a forthcoming publication [?].

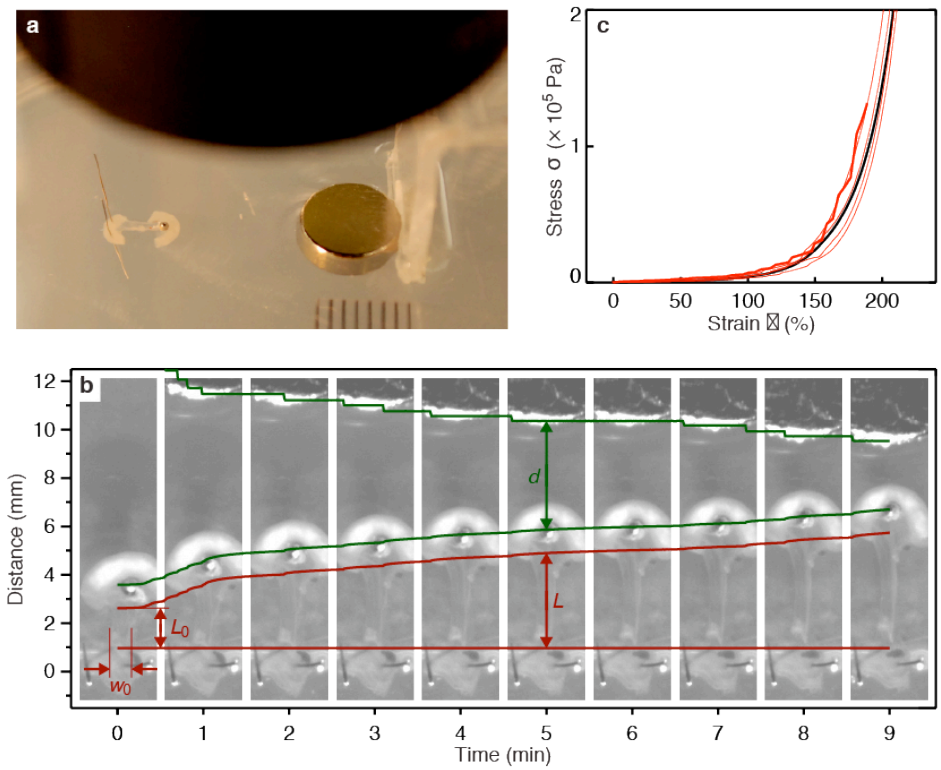

Figure S4 | Measurement of the mechanical properties of the mesentery, illustrated for Chicken E16. a , Ensemble view of the tensile test setup; the shadow is that of the microscope objective, along with the millimetric divisions of the ruler . b, The step-wise approach of the magnet stretches the sample by an amount L/L_0 that can be tracked as a function of the bead-magnet distance d. c, The resulting stress-strain mechanical response of the mesentery, as found for multiple samples (red), and the average (black) reported in Figure 3d of the main text.

Figures S4 and S5 show images from the procedure used for the measurement of the mechanical properties of the gut and mesentery tissue. The sample, to which the ball is attached, is laid out on the agarose gel and

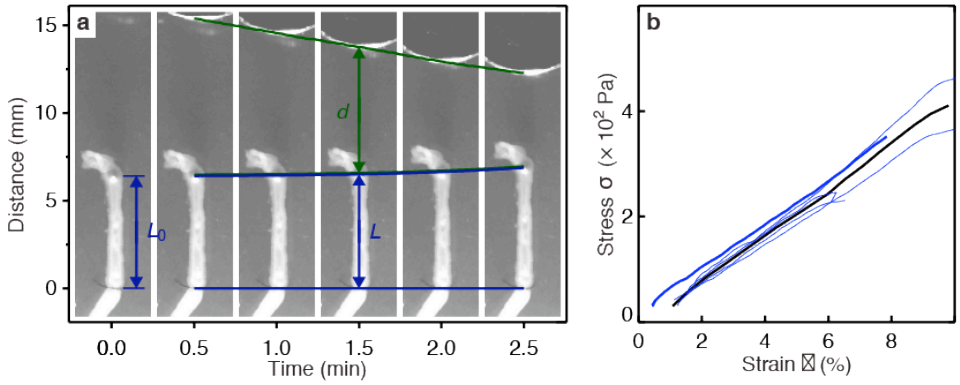

Figure S5 | Measurement of the mechanical properties of the gut tube, illustrated for Chicken E16. a , The approach of the magnet stretches the sample by an amount L/L_0 that can be tracked as a function of the bead-magnet distance d. b, The resulting stress-strain mechanical response of the tube, as found for multiple samples (blue), and the average (black) reported in Figure 3e of the main text.

immersed in the buffer (Figure S4a), while the magnet is brought towards the sample on the agarose gel along the strip's or tube's principal axis (Figs. S4b and S5a).

The supplementary movie 2 (S2.mov) shows a typical run for the tensile test on mesentery sample. Notably, the pre-conditionning stage, shown in the first 10 minutes of the movie time stamp, is commonly employed to produce reliable mechanical measurements relatively independent of previous manipulations [?, ?, ?]. Movies of the tensile tests were recorded using the digital camera at 2 frames per second (magnification of about 10 µm per pixel) and the position of the magnet and the bead are tracked using the image registration method described in the previous section. This allowed us to monitor simultaneously the changes in sample length L and bead-magnet distance d, which correspond to a aniaxial tensile test of the material at low rate, $\frac{1}{L}\frac{dL}{dt} < 10^{-3}\,s^{-1}$, thus ensuring that we probe only static elasticity of the material (i.e. the Young's modulus) [?, ?].

Image analysis allows us to determine both the natural rest length of the sample L_0 and the width w_0 from the micrograph, (see Figure S4b and the supplementary movie 2 (S2.mov)). Using the calibration curve shown in Figure S3, we can deduce the force F(d) applied to the sample as a function of the bead-magnet distance d. For the mesentery samples, we can evaluate the thickness at rest $h_0 = (1 + ⊠_p)^{1/2}h$ from the measurement of the thickness h associated with physiological strain $⊠_p$ (Figure S2). Since the section area of the sample is known ($A_0 = w_0h_0$ for mesentery strips, or $A_0 = \pi(r_o^2 - r_i^2)$ for the gut tube samples where the outer and inner radii r_o and r_i are extracted from micrographs (see Figure 3 of the main text)), we can determine the nominal stress $\sigma = \frac{F(d)}{A_0}$, and plot it against the nominal strain $⊠ = \frac{L}{L_0} - 1$ to quantify the mechanical response of the material. More sophisticated methods to extract the local strain field could be used here, for example by tracking small features in the sample. However we infer that the nominal strain is sufficient to evaluate both the non-linear mechanical response of the mesentery material and its effective differential (linearized) elastic modulus associated with physiologically relevant deformations. This method produces reproducible results, with same-sample variations that are below sample-to-sample variations that we measured at about 50%. Several stress-strain response curves, corresponding to samples of mesentery extracted from different Chicken E16 embryos are shown in Figure 4c and conform the reproducibility of these results.

To assess the existence ofi nhomogeneity and anisotropy of the material properties in the mesentery, we measured the stretching stiffness at a location in various directions (thus probing tissue anisotropy), and at different locations in the mesentery (probing tissue heterogeneity) for a given embryonic stage. We could not detect a significant difference between samples extracted from the same embryo, but at different location in the gut. We find small differences between tangential and radial dissection (radial sample were generally stiffer) for samples extracted from the same embryo, although these small distinctions were in general less

than the sample-to-sample variations across different embryos. This slight anisotropy in the mesentery tissue is compatible with the radial orientation of the distinguishable fibers (or veins), that can be seen on the dissected mesentery shown in Figure 1c of the main text, but not qualitatively relevant for our study here (see Fig. S4).

The tube displays a visible radial non-uniformity in the tube cross sections shown in Figure 3b of the main text (clearly distinguishable on the E16 micrograph), and we thus questioned whether a possible non-uniformity of the tube's Young's modulus could bias our estimate of the bending stiffness. Some tube segments exhibit a residual curvature which was small, and we used such a curved sample from embryonic chicken at day 16 to evaluate the bending stiffness directly from the force required to straighten the tube. If v_0 indicates the initial deflection of the tube from a straight line, and δ the relative displacement of the bead, then $F = \frac{E_t I_t}{v_0^2}\delta$ in the tube straightening regime of the tensile test[2]. We indeed observe two regimes for the force-extension response of the curved tube. Prior to straightening, starting from a deflexion $v_0 \approx 1.5\, r_o$, we measure $\frac{dF}{d\delta} \approx 10^{-4}$ N, while the tube is straightened, and $\frac{dF}{d\delta} \approx 10^{-3}$ N once the tube is straight (note that $\delta \ll 1$). The force-extension slope in the first regime yields a stiffness of $\frac{E_t I_t}{v_0^2}$ while the slope in the second regime yields a stiffness of order $\frac{4E_t I_t}{r_o^2 + r_i^2}$. Plugging the inner and outer tube radii values ($r_i = 230\,\mu m$ and $r_o = 390\,\mu m$, see Figure 3b of the main text) yields the same value ($E_t I_t = 5 \times 10^{-11}\ N \cdot m^2$) for the bending stiffness in either case, thus validating our method of measuring the bending stiffness of the gut tube.

These measurements corroborate the conclusions, based on proliferation rates and presented in the main text, that the stretched mesentery applies a uniform compressive force along the rostro-caudal extent of the gut tube and does not induce individual loops via inhomogeneous differential tension. Furthermore, it allows us to model the mesentery and the gut as isotropic, homogeneous incompressible materials with a mechanical response that can be characterized solely in terms of their incremental Youngs moduli.

Computational model of gut looping

Since growth occurs over a period of days, inertial and viscous effects are negligible. When the gut is surgically separated from the mesentery, it relaxes to a naturally straight configuration while the mesentery shrinks to a slightly non-planar sheet; this is true at all stages of development prior to the formation of the fully developed loops. This implies that the looped configuration arises solely due to the fact that it is an energetic minimum (subject to the constraint of a vanishing linking number) of the composite system whose constituents grow relative to each other, and change their intrinsic morphometric and mechanical properties, over time. In other words, at each time points of development, the loop pattern results from the equilibrated arrangement taken by the composite membrane-tube system for the single values of their mechanical and geometric properties at this particular time point.

To build a computational model that predicts the loops pattern observed at a particular time point, given the mechanical and geometric properties of such composite system (at that time point) as input parameters, we follow a method described in detail elsewhere [?, ?]. That is, we approximate the elastic membrane by a discrete planar mesh of typically 300×60 equilateral-triangular elements. We approximate the tube by a similar planar mesh with different mechanical properties, made of exactly 2 rows of triangular elements (see Figure S6a where, following the conventions used throughout the paper, the tube is marked in blue and the membrane is marked in red). The elastic energy $F = F_m + F_t$ of the composite system is then the sum of the elastic energy of the membrane F_m and that of the tube F_t. In the following, we first summarize the algorithm used to obtain the configuration that minimizes energy. In particular, we justify our approximation of the tube by a 2-rows planar mesh. We then show the results of the simulations in two contexts: first an input

[2] Using the notations of the figure below,

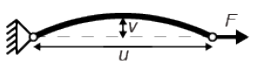

we evaluate the bending moment by $8E_t I_t\, v/u^2 - v_0/u_0^2$, where (u_0, v_0) defines the configuration of the curved tube at rest with $v_0 \ll u_0$. The force applies a torque $2Fv$. Calling $\delta = u/u_0 - 1 \ll 1$ the initial relative displacement, and $L_0 \approx \sqrt{u^2 + (2v)^2}$ the invariant tube contour length, the moment balance reads $F \approx (E_t I_t / v_0^2)\delta$.

parameter sweep, that we used to get the data shown in figure 4 of the main text; and second, by using actual values of the input parameters, as measured on the chicken gut at several time points, to visually compare the simulation with their real-life counterparts.

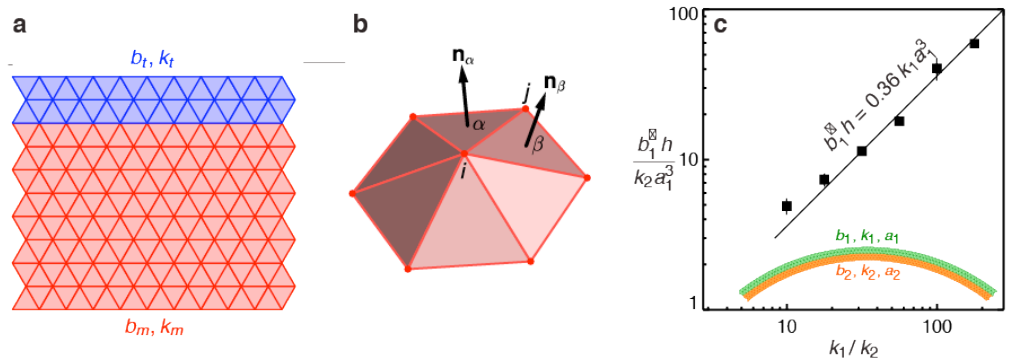

Figure S6 | Computational model for the gut-mesentery system and its calibration. a . The tube-membrane composite system is simulated by using a planar discrete triangular mesh, with an in-plane stretching stiffnesses k_t and an out-of-plane bending stiffness b_t for the tube (blue), and similarly stretching stiffness k_m and bending stiffness b_m for the membrane (red); see text for details and the relative magnitudes of these quantitites. b. The discrete mesh approximation penalizes both in-plane and out-of-plane deformations; the extension/compression of springs ij connecting nodes i, j penalize in-plane stretching, while the relative orientation between the normals n_α and n_β of neighboring facets α, β penalize out-of-plane deformations c. To calibrate the isotropic bending stiffness of the gut tube, and determine the relationship between k_1 and the in-plane bending stiffness $b_1^{\boxtimes}$ we compare our simulations with a simple analytic relationship for the bending of a bimaterial strip (solid line) (see text for details).

The discretized "membrane" and its continuum limit

Following the notations defined in Figure S6b, we may write the elastic energy density of the membrane $F_m = F_{m,s} + F_{m,b}$ as the sum of the stretching energy density $F_{m,s} = \frac{\sqrt{3}k_m}{4}\sum_{ij}(r_{ij} - a_m)^2$, where r_{ij} is the distance between two nodes i and j and a_m is the natural rest length between nodes in the membrane (which can change as a consequence of growth), and the bending energy density $F_{m,b} = \frac{b_m}{\sqrt{3}}\sum_{\alpha\beta}(n_\alpha - n_\beta)^2$, where n_α and n_β are the unit normal vectors of the two facets α and β (see Figure S6b). The membrane material coefficients k_m and b_m are defined as $k_m = E_m h$ and $b_m = E_m \frac{h^3}{12}$ where E_m is the membrane Young's modulus and h is the membrane thickness. In particular, b_m is the out-of-plane bending stiffness per unit width of the membrane. The parameters k_m and b_m can be obtained from the measurements of E_m and h on the real systems. The discrete representation of the membrane we use here has been shown in previous work to converge to the continuum limit of the so-called generalized Föppl-von Kármán equations used to describe the mechanics of thin plates that grow [?, ?], i.e. the discrete energy F_m converges to the elastic energy density of a plate in the continuum limit when $a_m \boxtimes 0$.

The discretized "tube" and its continuum limit

Similarly for the tube, $F_t = F_{t,s} + F_{t,b}$ with $F_{t,s} = \frac{\sqrt{3}k_t}{4}\sum_{ij}(r_{ij} - a_t)^2$ and $F_{t,b} = \frac{b_t}{\sqrt{3}}\sum_{\alpha\beta}(n_\alpha - n_\beta)^2$, where a_t is the natural rest length between nodes along the tube (and can change as a result of growth), and where the sums run over the elements belonging to the tube. The tube material coefficients $k_t = E_t \frac{\pi(r_o^2 - r_i^2)}{2r_o}$ and $b_t = E_t \frac{\pi(r_o^4 - r_i^4)}{8r_o}$, where E_t is the tube's Young modulus and r_i, r_o are the inner and outer tube radii respectively. To assess the validity of the approximation we use here to represent the tube, we first need to ensure that the stretching

and the out-of-plane bending response of the simulated 2-row strip attached at the edge of the membrane, is mathematically equivalent to the continuum limit of an axially symmetric tube that can stretch, bend and twist, i.e. the in-plane and out-of-plane bending stiffnesses must be equal in our discrete representation of the tube (which is isotropic).

To calibrate and verify this we use the same discretization scheme as above, and perform a separate set of simulations of a different system: a bi-material composite strip, shown in Figure S6c. We attach a strip made of a 2-row planar triangular mesh of material 1, with mechanical stretching stiffness k_1, out-of-plane bending stiffness b_1, and spring rest length a_1, to another strip made of a ν-row triangular mesh of material 2 with mechanical parameters k_2 (stretching), b_2 (out-of-plane bending) and a_2 (rest length). Both strips are assumed to have a thickness h. The width of the strip of the material 2 is chosen with $\nu < 10$, in contrast with the tube-membrane simulations described above where the membrane mesh is chosen as wide as possible We introduce a mismatch strain $\epsilon_0 = \frac{a_1}{a_2} - 1$ and calculate the mechanically stable configurations of the bi-material composite by minimizing the total elastic energy using a damped molecular dynamics method [?]. For $b_1 \gg k_1 a_1^2$, $b_2 \gg k_2 a_2^2$, $\nu < 10$ and $\epsilon_0 < 100\%$, we observe that the bi-material composite beam bends in its plane with a uniform radius of curvature ρ (see inset of Figure S6c). In this regime we evaluate the effective in-plane bending stiffnesses per unit thickness, $b_1^{\square}$ and $b_2^{\square}$ of materials 1 and 2 respectively, from the measurement of ρ; indeed a classical result due to Timoshenko [?] shows that the radius of the strip, $\rho = \frac{1}{\epsilon_0}\left(\frac{2a_1+\nu a_2}{2} + 2h\frac{b_1^{\square}+b_2^{\square}}{2a_1+\nu a_2}\right)\left(\frac{1}{2k_1a_1} + \frac{1}{k_2\nu a_2}\right)$. Additionally, we expect [3] $b_1^{\square} \gg k_1$ and $b_2^{\square} \gg k_2$. Furthermore, in the regime $b_1^{\square} \gg b_2^{\square}$, corresponding to the case when the material 1 is much stiffer than the material 2, it follows $k_1 \gg k_2$, so that

$$\frac{\epsilon_0\rho}{a_1} \approx \frac{2+\nu}{2} + \frac{2}{\nu(2+\nu)}\frac{b_1^{\square}h}{a_1^3k_2} \qquad (1)$$

and allows us to calculate $b_1^{\square}$ from the radius ρ for various values of the parameters, as long as the aforementioned inequalities are satisfied [4]. The results of these simulations are shown in Figure S6c and fit the relation $b_1^{\square}h = 0.36\,k_1a_1^3$ for different values of $\epsilon_0 < 100\%$ and $3 \le \nu \le 9$ consistent with the continuum theory [3]; the slight difference from a perfectly linear relationship occurs at $k_1/k_2 \approx 10$ (see Figure S6c), where our approximation of Timoshenko's formula, equation (1), fails. Matching both the in-plane and out-of-plane bending stiffnesses of the 2-rows strip of material 1 (with width $2a_1$ and thickness h) yields $b_1^{\square}h = 2b_1a_1$, so that $k_1a_1^2 = 5.6\,b_1$. This then is the relation between the parameters k_1, b_1 and a_1 that characterize the 2-row edge strip as mathematically identical to an elastic tube of radius a_1 exhibiting an axially symmetric bending stiffness $2b_1a_1$ attached along the edge.

Then k_t and b_t are related by the following relation: $k_tr_o^2 = \frac{4}{1+(r_i/r_o)^2}b_t$. For both the biological and physical (i.e. rubber) experimental systems considered in our study, we measured that $0.3 < \frac{r_i}{r_o} < 0.6$, i.e. $2.9\,b_t < k_tr_o^2 < 3.6\,b_t$. These inequalities are in close agreement with the symmetry of the tube bending stiffness, that requires $k_tr_o^2 = 5.6\,b_t$ as we just demonstrated with the bi-material strip, since the gut is typically very stiff in extension so that it can be modeled as being inextensible[5]. We further verified that changing the ratio $k_tr_o^2/b_t$ by 40% did not actually significantly alter our results.

---

[3] In fact, one expects only small deviations, due to discretization errors, from the laws $b_1^{\square}h = k_1\frac{(2a_1)^3}{12}$ and $b_2^{\square}h = k_2\frac{(\nu a_2)^3}{12}$ (derived in continuum mechanics).

[4] If we take $a_1 = r_o$, $k_1 = k_t$, $b_1 = b_t$, $k_2 = k_m$, $b_2 = b_m$ and $\nu = \frac{\epsilon_0\rho}{r_o} \gg 1$ for the width of membrane, as assumed in the main text, we obtain the scaling $\rho \sim \left(\frac{E_tt_t}{E_mh}\right)^{1/3}\epsilon_0^{\beta}$, with $\beta = -1$ as a consequence of the local torque balance [?]. The loop-wise force balance derived in the main text results in a similar scaling but with $\beta = -\frac{2}{3}$.

[5] For $k_t/k_m \gg 1$, the axial compression of the tube can reach a few percent thus effectively changing the mismatch strain between the membrane and the tube, while for both the biological gut and the rubber models, $k_t/k_m \gg 1$ so that axial compression is negligible. In simulations performed with $b_t < 0.1$, and at input strains $\epsilon_0 < 10\%$, the loop radius is about 50% higher than the theoretical fit presented in Figure 4c of the main text, since the input strain is moderated by the tube axial compression. In this particular case we used the mismatch strain associated with the actual rather than the natural tube length, thus effectively excluding the effects of axial compression.

Building the membrane-tube composite

Growth of the tube and the membrane is simply modeled as a change in the rest lengths between the nodes, so that differential growth (and thus the induced mismatch strain) arises when there are spatial variations in these parameters in either the tube or mesentery, or because the rest lengths are not the same in the tube and the membrane. Since our experimental observations show that there are no spatial variations in either the growth of the edge of the mesentery or along the gut, but there is a mismatch strain $\boxtimes_0$ between the tube and the membrane, we set $\frac{a_t}{a_m} = 1 + \boxtimes_0$. We then use a damped molecular dynamics method to minimize the system energy [?]. The resulting, mechanically stable, equilibrium geometrical configuration adopted by the composite system can then be recorded for the particular choice ofi nput parameters k_m, b_m, k_t, b_t, a_t and $\boxtimes_0$.

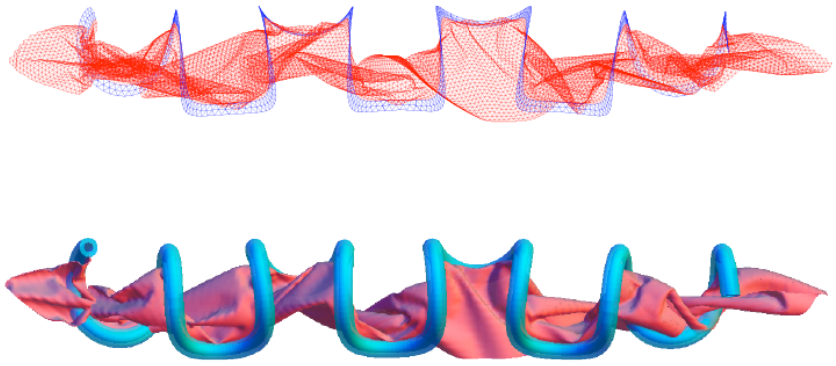

Figure S7 | Rendering of the mesh model. The top image represents a mesh calculated by our simulation procedure (this 3D image can be interactively manipulated in the PDF version; Adobe Reader 9.4 or higher is required), while the bottom image is the corresponding representation of the same configuration (from the same point of view), obtained using a rendering engine. The fine wrinkles in the mesentery are associated with its very small bending stiffness, but are energetically insignificant and do not effect the gut looping patterns.

Results: sweeping the parameter space

The simulations are first used to determine the equilibrated configurations of the tube-membrane system in a wide, yet realistic, range ofi nput parameters values. For the membrane, in terms of the length scale $a_t = r_o$ and of the effective Young's Modulus $E_m \frac{h}{r_o}$, we find that the experimental bending stiffnesses of the membrane encountered in this study (for both the biological mesentery and latex sheet) in the range $10^{-5} < b_m < 10^{-3}$ has no detectable influence on the results presented here. Therefore we ran our simulations using the above set of units, where $k_m = 1$, with $b_m = 10^{-4}$ for the membrane, and $k_t = 5.6\, b_t$ for the tube where b_t varies between 2×10^{-2} and 10 to cover a wide range that encompasses the experimental values measured in our study. For each b_t chosen in this range[5], we investigated values of $\boxtimes_0$ between 0 and 100%.

The supplementary movie 1 (S1.mov) present the resulting equilibrium geometries for various choices of these input parameters. Configurations with three values of b_t are represented[6] at the top, center and bottom of each frame. The parameter $\boxtimes_0$ increases from one frame of the movie to the next while keeping the value

[6] When rescaled correctly, b_t is calculated as the ratio $\frac{E_t I_t}{2E_m h r_o^3}$ where $I_t = \frac{\pi}{4}(r_o^4 - r_i^4)$.

of b_t constant for each top, center and bottom configuration. We note that each frame presents equilibrium configurations of the composite system that have reached minimum energy for a particular set of parameters b_t, ⊠$_b$. Thus the movie does not represent the approach to equilibrium, but is a series of actual equilibrated configurations adopted by the composite system, for the range of parameters shown in the accompanying graph. In this movie, and throughout the article, we use a blue tube to render the configuration adopted by the 2-rows strip along the edge of the mesh (consistent with our calibration ofi ts isotropic bending stiffness as indicated above), and a continuous red membrane to render the remaining mesh of the composite system. Figure S7 shows a mesh configuration, direct output of the simulations, and its rendering following these conventions. We note that there are small boundary layers near the edges of the composite system where the loop radius and wavelength deviate from the values in the interior - these boundary layers arise since the edges are free. We also note that bending the mesentery out of the plane costs very little energy, and thus leads to the formation of many fine wrinkles [?] , as observed in some of the rubber models. However, these are of no relevance in determining the gut looping pattern.

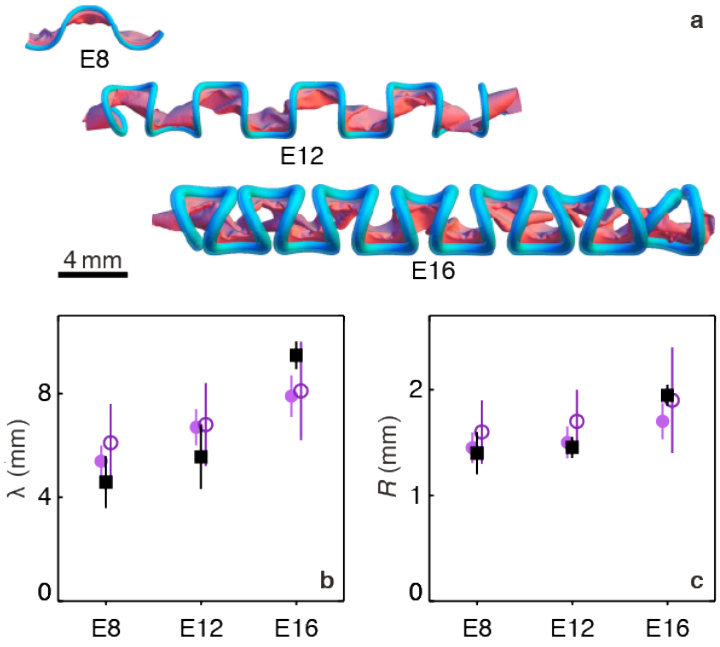

Figure S8 | Numerical evolution of the form of the chick gut. a , Equilibrated configurations of the tube-membrane system calculated numerically using the experimental measurements, performed on chicken embryos at E 8, E 12 and E 16, as input parameters. b, The loop contour wavelength λ measured from the embryos (squares), from the configurations shown in panel a (filled circles) and from the simple model (3) of the main text (open circles) at the three stages E 8 – 12 – 16 of development (symbols are shifted horizontally to show the error bars; in the numerical model, error bars originate from the finite length of the simulated system that leads to small end corrections associated with the presence of boundary layers near the free edge, as expected). c, The loop radius R, symbols as in panel b.

Results: simulating the chicken guts at several time points of development

The mechanical parameters k_m, b_m, k_t, b_t are extracted from the morphometric and mechanical measurements performed at various time points during development (see main text and its Figure 3). In particular, we measure the mismatch strain as explained in the main text and Figure 3d using the fact that the mesentery has a periphery shorter than the tube extent when both lengths are measured upon their surgical separation (thus leading to a physiological mismatch strain $\boxtimes_p$, see main text). We then obtain $\boxtimes_b$ from linearizing the elastic response of the mesentery around the particular value of the physiological strain $\boxtimes_p$ (see main text) [7].

At different time points along the development of the gut, the mesentery thins, the tube thickens and simultaneously grows relative to the mesentery. Thus the mismatch strain $\boxtimes_b$ at a particular time point depends on the total differential growth between the gut and the mesentery. Similarly, the mechanical and geometrical parameters change as the gut develops. At every time point, mechanical equilibrium determines the gut morphology and our simulations can be used to determine the equilibrium shape of the gut-mesentery composite using the measured mechanical and geometrical parameters and the relative growth strain. Using the experimental values of the parameters $h, r_i, r_o, E_t, E_m, \boxtimes_b$ at three time points $E8$, $E12$ and $E16$ of the chicken gut development (see main text, where the data are summarized in Table 1), in Figure S8a we show the numerically obtained (equilibrated) corresponding configurations. This illustrates how we can track the evolution of gut development as a function of the measured mechanical and geometrical parameters that are input in our model. The simulated configurations closely match the shape of the real gut (see Figures 1a, 2c and 4a of the main text). In Figures S8b and c we show how the geometrical characterization of the loops evolves in terms of the contour wavelengths λ and radius R, at these three developmental time points, and the excellent parameter-free agreement with experimental measurements of these quantities in the chick gut. Ideally, we would of course like to predict the evolution of the geometry of the tube, the mesentery and the relative growth - but we have no theoretical basis for this at present.

Comparative mechanical properties of other species: quail, finch and mouse

For each quail, zebra finch, and mouse we selected two developmental time points representing an early and late phase of looping, where the latest stage chosen on the basis of the time after which the number of loop does not change anymore. For each animal, we repeated the morphometric and mechanical measurements, just as shown for the chicken in the main text, and followed the gut development using the same methods for all species.

The results, shown in Figures S9 to S11 follow the same structure used in Figure 3 of the main text. We see that although the actual geometrical dimensions for the different animals are very different (see Figure 5 of the main text), there are similar trends in the morphometric characteristics across species: the thickness of the mesentery decreases with embryonic age, while the tube enlarges. The differential growth between the gut and the mesentery is characterized by the physiological mismatch strain between the tube and the perimeter of the mesentery $\boxtimes_p = \frac{L_t}{L_m} - 1$ (L_t is the tube contour length, and L_m is the mesentery perimeter, see the main text) increases during embryonic development ($\boxtimes_p$ increases with the embryonic age). The physiological strain falls between 100% and 200% at gut development maturation for all species studied here.

The mechanical properties of the tissues are of the same order of magnitude for the 3 birds, while the mouse tissue is in general softer. Although the detailed causes of this mechanical diversity are not investigated here, it is striking that the physiological stresses in the mesentery fall in the same range ($\boxtimes$ 0.1 MPa) for all the species investigated in this study. This suggests that growth and properties of tissues might be regulated by mechanical feedback.

In the inset of Figures S9c to S11c, we report the volumetric growth of the gut and the mesentery. For the embryonic chicken, we observe that the volume increase is well approximated by a simple exponential with growth rates of about $2.5\,\%$ per hour for the tube, and about $1.5\,\%$ per hour for the mesentery. The cell proliferation reported in Figure 1 of the main text indicates that at E12, about 200 cells in a volume $1\,mm^2 \times$

[7] Similarly, for the rubber simulacrum described in the previous section, the mechanical parameters are measured directly and the mismatch strain $\boxtimes_b$ is dialed in by stretching the membrane before it is stitched to the tube, which is kept unstretched, after which the composite system is allowed to relax to its equilibrium.

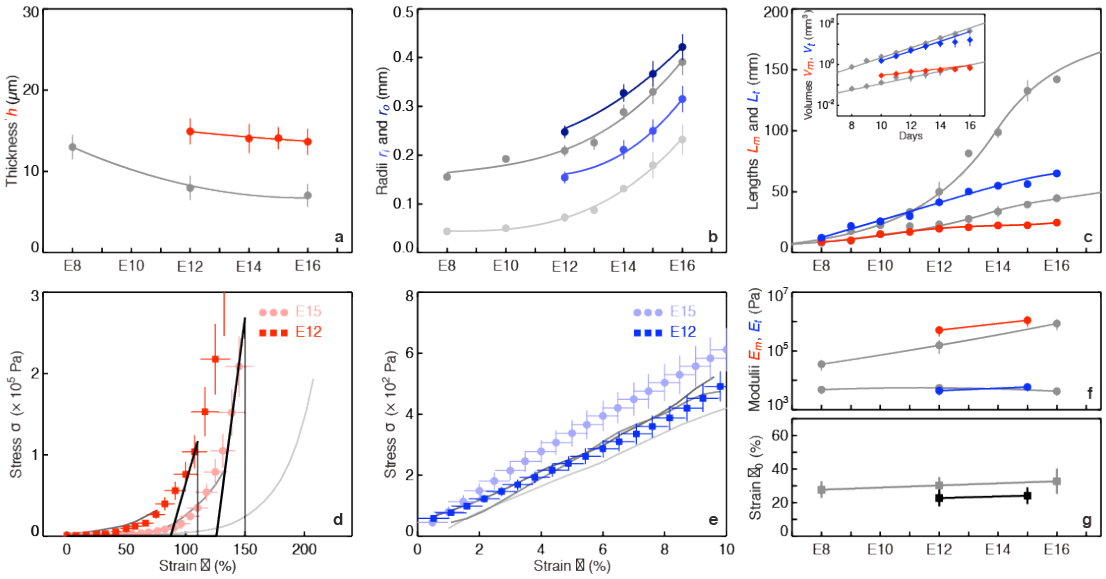

Figure S9 | Morphometric and mechanical measurements for quail at embryonic days E12 and E15. a, Mesentery thickness vs. embryonic day. b, Inner and outer tube radii vs. embryonic day. c, Tube and mesentery differential growth. d, Nominal stress vs. nominal strain response curves for the mesentery. e, Stress vs. strain response curves for the gut tube. f, Mesentery and tube effective Young's modulus vs. embryonic day. g, Effective differential growth strain vs. embryonic day. In all panels, the grey curves are the corresponding results for chick (E8, E12 and E16 are reported, see main text).

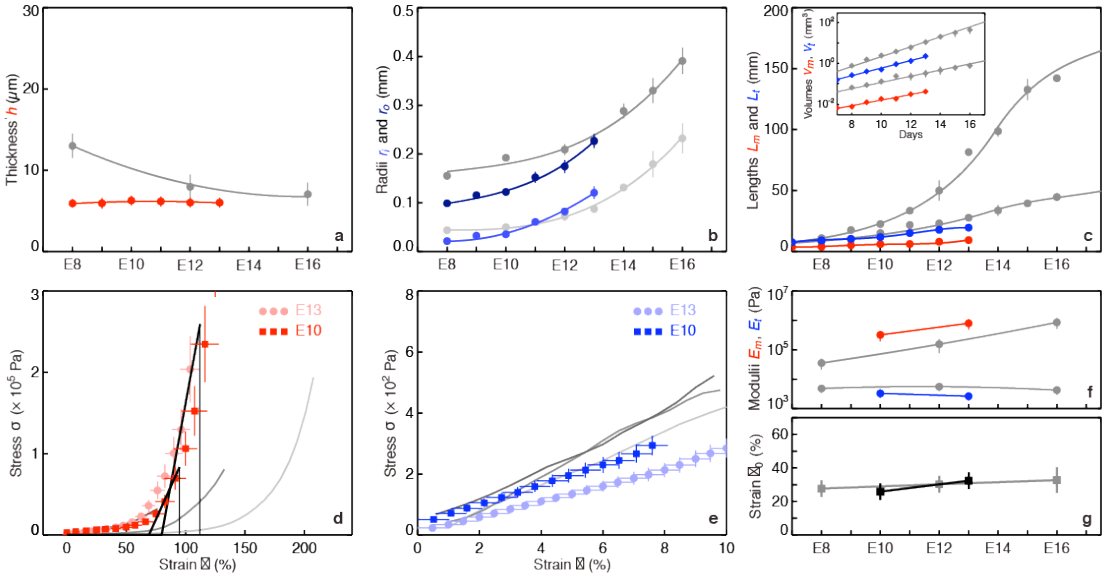

Figure S10 | Morphometric and mechanical measurements for finch at embryonic days E10 and E13. Panels are the same as in Figure S9.

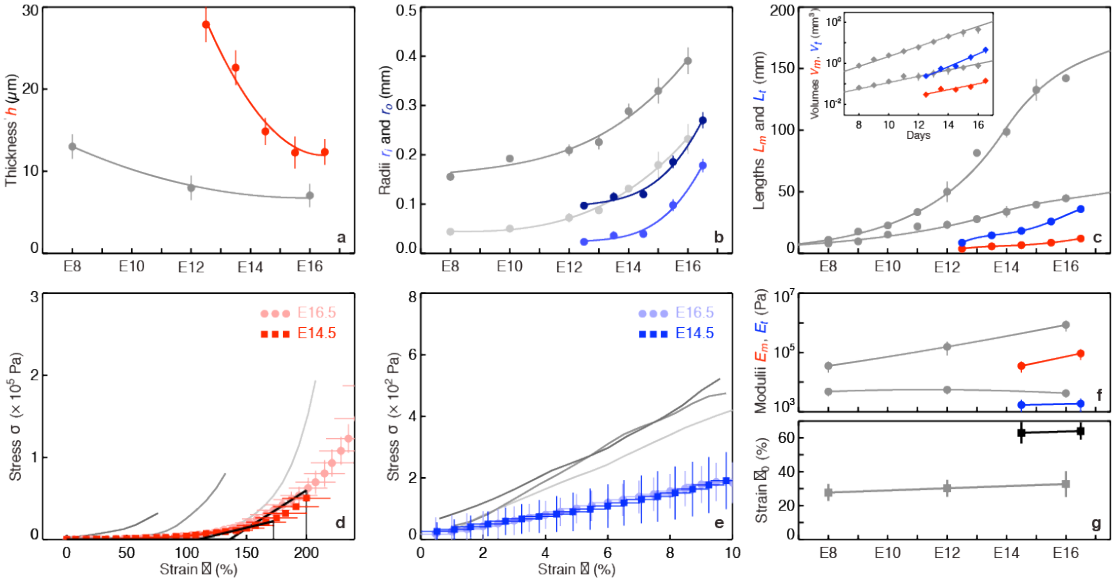

Figure S11 | Morphometric and mechanical measurements for mouse at embryonic days E14.5 and E16.5. Panels are the same as in Figure S9.

are created in the tube per unit generational (mitotic) time, while about 70 cells divide in the same volume of mesentery in the same time. Assuming mitosis takes ⊠ 1 h and an effective cell volume is ⊠ 1 pL, we thus obtain instantaneous volume growth rate of about 2 % per hour in the tube and 1 % per hour in the mesentery, in agreement with our direct volumetric growth rate measurement.

References

[1] Crocker, J. C. & Grier, D. G. Methods of digital video microscopy for colloidal studies. J. Colloid Interface Sci. 179, 298–310 (1996).

[2] Xie, H. J., Hicks, N., Keller, G. R., Huang, H. T. & Kreinovich, V. An IDL/ENVI implementation of the FFT-based algorithm for automatic image registration. Comput. Geosci. 29, 1045–1055 (2003).

[3] Landau, L. D. & Lifshitz, E. M. Fluid mechanics (Pergamon Press, Oxford, England, 1987), 2nd edn.

[4] Savin, T., Shyer, A. E. & Mahadevan, L. In preparation .

[5] Lepetit, J., Favier, R., Grajales, A. & Skjervold, P. O. A simple cryogenic holder for tensile testing of soft biological tissues. J. Biomech. 37, 557–562 (2004).

[6] Fung, Y. C. Elasticity of soft tissues in simple elongation. Am. J. Physiol. 213, 1532–1544 (1967).

[7] Fung, Y. C. Biomechanics : mechanical properties ofl iving tissues (Springer-Verlag, New York, 1993), 2nd edn.

[8] Kenedi, R. M., Gibson, T., Evans, J. H. & Barbenel, J. C. Tissue mechanics. Phys. Med. Biol. 20, 699–717 (1975).

[9] Seung, H. S. & Nelson, D. R. Defects in flexible membranes with crystalline order. Phys. Rev. A 38, 1005–1018 (1988).

[10] Liang, H. & Mahadevan, L. The shape of a long leaf. Proc. Natl. Acad. Sci. U.S.A. 106, 22049–22054 (2009).

[11] Allen, M. P. & Tildesley, D. J. Computer Simulation of Liquids (Oxford University Press, New York, 1989).

[12] Timoshenko, S. Analysis of bi-metal thermostats. J. Opt. Soc. Am. Rev. Sci. 11, 233–255 (1925).

[13] Cerda, E. & Mahadevan, L. Geometry and physics of wrinkling. Phys. Rev. Lett. 90, 074302 (2003).

Appendix II: Supplementary Information for Villification

Supplementary Material for "Villification" Shyer et al.

Computational model of luminal patterns

When the mesenchyme-endoderm composite is surgically separated from the muscle, it expands and unfolds. Furthermore, when the endoderm is peeled from the mesenchyme and cut open it relaxes to an approximately planar sheet. These observations suggest that the patterning is driven by mechanical instabilities and that the folded states are energy minima of an elastic mesenchyme-endoderm composite whose constituents grow uniformly, but at different rates, in a cylindrical volume constrained by a relatively much stiffer muscle. This is true during development at least until approximately E14 or E15 in chick and mouse.

To investigate the folding patterns numerically, we construct a finite element model that minimizes the deformation energy of the system consisting of elastic mesenchyme and endoderm layers. The simulated layers are discretized into a rectangular mesh, and each rectangle is divided into five tetrahedron elements as indicated in Figs. S7. Arrangement of the tetrahedrons in any two neighboring rectangles is reflected in order to preserve the reflection symmetries of the mesh. The mesh spacing is denoted by a.

A stress-free state of a tetrahedron is contained in matrix

$$\hat{\mathbf{A}} = \left[\hat{\mathbf{x}}_1 \quad \hat{\mathbf{x}}_2 \quad \hat{\mathbf{x}}_3\right],$$

where $\hat{\mathbf{x}}_1$, $\hat{\mathbf{x}}_2$ and $\hat{\mathbf{x}}_3$ are vectors describing the tetrahedron (Fig. S7D). Growth is implemented simply by expanding the stress-free state $\hat{\mathbf{A}}$. The deformed state of the tetrahedron is contained in

$$\mathbf{A} = \left[\mathbf{x}_1 \quad \mathbf{x}_2 \quad \mathbf{x}_3\right] = \mathbf{F}\hat{\mathbf{A}},$$

where $\mathbf{x}_1$, $\mathbf{x}_2$ and $\mathbf{x}_3$ are the deformed basis vectors (Fig. S7E) and **F** is the deformation gradient. At each time step of the simulation **F** is obtained by

$$\mathbf{F} = \mathbf{A}\hat{\mathbf{A}}^{-1}.$$

We model the tissues by a neo-Hookean constitutive model with strain energy density

$$W = \frac{\mu}{2}\left[\mathrm{Tr}\left(\mathbf{F}\mathbf{F}^{\mathrm{T}}\right)J^{-2/3} - 3\right] + K(J - \log J - 1),$$

where μ and K are the shear and bulk moduli, respectively, and $J = \det(\mathbf{F})$. We assume $K = 3\mu$ in all simulations. W is the energy per unit volume in the deformed state. The corresponding Cauchy stress, i.e., the force per unit area in the deformed state is given by

$$\sigma = \frac{1}{J}\frac{\partial W}{\partial \mathbf{F}}\mathbf{F}^{\mathrm{T}}.$$

Surface traction of each deformed face (i = 1, 2, 3, 4) of the tetrahedron is given by

$$\mathbf{s}_i = -\sigma\mathbf{n}_i,$$

where $\mathbf{n}_i$ are normals with lengths proportional to the deformed areas of the faces. Nodal forces are obtained by distributing the traction of each face equally to its three vertices.

Our model includes also the self-avoidance of luminal surface. Element faces at the surface make up a triangular lattice for which self-avoidance can be enforced by processing vertex-triangle and edge-edge contacts. Contacts are penalized by energy $Ka^2\left[(h-d)/h\right]^2$ if the separation d between a vertex and triangle, or between two edges,

is less than the contact range $h = a/3$. Contact force from this potential is interpolated to the nodes of the associated geometric primitives.

After the nodal forces are determined the Newton's equations of motion are solved for the nodes by an explicit scheme

$$\mathbf{v}(t + \Delta t) = \mathbf{v}(t) + \frac{\mathbf{f}(t) - \gamma \mathbf{v}(t)}{m} \Delta t ,$$

$$\mathbf{x}(t + \Delta t) = \mathbf{x}(t) + \mathbf{v}(t + \Delta t)\Delta t.$$

Here $\Delta t = 0.1a/\sqrt{K}$ is the time step, $m = a^3$ mass of a node, and $\gamma = 10m$ viscous damping factor. Vectors **f**, **v** and **x** are force, velocity and position of a node, respectively. The damped Newton's dynamics is simulated in order to minimize the elastic energy. Hence the simulations are performed slowly (quasistatically) to allow full elastic relaxation at any time, with negligible inertial and viscous effects.

Details for the tubular chick and mouse simulations (Figs. 4 and 6 in the main article)

To model the relative growth in the mesenchyme-endoderm tubes, time is parameterized by $t \in [0,1]$ and dimensions of the mesenchyme and endoderm are varied as a function of t so as to approximate the observed geometries. In both simulations mesenchyme and endoderm are restricted into a cylindrical tube with diameter D and length $L = 1.25D$. The outer boundary of the mesenchyme is clamped to the cylinder and periodic boundary conditions are applied at the ends of the tube. Stress-free states of the mesenchyme and endoderm are flat, which means that if they were separated and cut open they would relax into flat sheets.

In the chick simulation (Fig. 4) the size of the simulation mesh, including both layers, is 400 × 160 × 24 rectangles (width × length × thickness). D expands linearly by a factor 2.7 as time goes from $t = 0$ to $t = 1$, corresponding to real time going from E7 to E14. The endoderm is 12 times stiffer than the mesenchyme ($\mu_e / \mu_m = 12$). Stress-free dimensions of the endoderm are

$$\text{thickness} \quad h_e = (0.13 - 0.1t)D ,$$

width (circumferential) $w_e = (0.35 + 2.8t - 1.4t^2)\pi D,$ and

length (longitudinal) $l_e = (1 + 0.5t^2)L$.

Stress-free dimensions of the mesenchyme are

thickness $h_m = (0.39 - 0.3t)D$,

width (circumferential) $w_m = 1.5\pi D,$ and

length (longitudinal) $l_m = (1 + 0.333t^2)L$.

In the mouse simulation (Fig. 6) the size of the simulation mesh, including both layers, is 320 × 160 × 30 rectangles (width × length × thickness). D expands linearly by a factor 2 as time goes from $t = 0$ to $t = 1$, corresponding to real time going from E12.5 to E15.5. The endoderm is 1.5 times stiffer than the mesenchyme ($\mu_e / \mu_m = 1.5$). Stress-free dimensions of the endoderm are

thickness $h_e = (0.2 - 0.1t)D$,

width (circumferential) $w_e = (0.5 + 2t - t^2)\pi D,$ and

length (longitudinal) $l_e = (1.6 + 1.2t - 0.6t^2)L$.

Stress-free dimensions of the mesenchyme are

thickness $h_m = (0.2666 - 0.0666t)D$,

width (circumferential) $w_m = 1.5\pi D,$ and

length (longitudinal) $l_m = (1.4 + 0.8t - 0.4t^2)L$.

We emphasize that direct input parameters of these simulations include the outer diameter D and moduli of the endoderm and mesenchyme. The above stress-free states are chosen so as to approximately yield the observed cross-sectional geometries and expansion ratios of separated mesenchyme-endoderm composite. Even though the dimensions of the stress-free states are not fitting parameters in strict sense, they are fairly tightly guided by the observed deformed states. For example, circumference and thickness of the chick endoderm measured from the cross-section images are close to the corresponding stress-free dimensions due to its relatively high stiffness. On the other hand, mesenchyme appears strongly squeezed in the cross-section images and it is thus difficult to tell precisely what stress-free dimensions it has. Simulations, however, suggest that folding is not sensitive to the exact shape of the stress-free state of the mesenchyme. We have also performed coarse residual strain measurement of the mesenchyme on few samples that indicate that the above stress-free states are realistic.

Details for the zigzag simulation (Fig. 5 in the main article)

The effect of non-uniform growth on a zigzag pattern is investigated by simulating a small planar domain that contains one zigzag cell (visualizations in Fig. 5 and Fig. S5A show nine replicates of the simulated domain). The domain has periodic lateral boundaries and a clamped base. The mesh size is 120 × 120 × 32 rectangles (width × length × thickness). Stiffness of the endoderm is $\mu_e = 12\mu_m$ and its stress-free thickness is $h_e = h_m / 2$.

The simulation starts from a zigzag pattern that is created by growing the endoderm laterally such that its stress-free width $w_e = 2W$ and length $l_e = 2L$, where W and L are the lateral dimensions of the simulation domain. The mesenchyme is grown laterally as well such that its dimensions $w_m = 1.666W$ and $l_m = 1.666L$. The lateral dimensions of the simulation domain are optimized to minimize the energy of the pattern, which yields $W \approx L \approx 2.0(h_e + h_m)$. This result is in agreement with the approximately equal circumferential and longitudinal spacing of the zigzags in real chick intestines.

The flat stress-free state of the endoderm is broken by laterally expanding spots that are centered in the pits of the zigzag pattern, i.e., the points of the endoderm that are nearest to the base (Fig. S5B). For parameterized time going from t = 0 (uniformly compressed state) to t = 1, the relative expansion of a spot is given by $1 + \left(e^{-[r/(3h_e)]^2} - 0.2\right)$, where r is the distance from the origin of the spot along the endoderm in the stress-free state before the expansion. This form of expansion keeps the total stress-free area of the endoderm approximately constant due to the negative expansion far from the spots. The total expansion includes superposed contributions of

both spots in the simulation domain. As a result the whole zigzag valley expands, with the most expansion at the pits (Fig. S5C). Lateral dimensions of the simulation domain and the stress-free state of the mesenchyme are held fixed during this step.

The applied growth field here only qualitatively mimics the experimental observations, since it is difficult to determine the actual growth field. In addition to proliferation, cell migration may contribute in the process of moving from a flat to non-flat stress-free state. Nevertheless, the simulation robustly captures the twisting and rotation of the zigzags that precede the formation of definite villi. Interestingly, this transformation breaks the longitudinal reflection symmetry of the pattern, despite the initial zigzag pattern as well as the applied growth field have the longitudinal reflection symmetry.

Simulation for Measurement of Shear Modulus

To be consistent with the experimental set-up to measure the shear moduli of different layers of chick/mouse gut, we construct the model for simulation as shown in Fig. S.1 using the mean values of geometric parameters measured from experiments. The gut samples, which are modeled as deformable cylindrical tubes, sit in between two rigid planes, the top one being the glitter and the bottom one being the substrate. The stiff layer is colored in green and the soft layer is colored in blue. The incompressible neo Hookean material is used for both layers. Hard contact in the normal direction and frictionless sliding in the tangential direction are imposed as the contact conditions between the plane and outer surface of the tube. Only one eighth of the complete tube is simulated in practice by imposing appropriate symmetric boundary conditions on its symmetric planes. The simulated stiff section is meshed by $50 \times 20 \times 40$ elements along the circumferential, the thickness and the length direction respectively, and the soft section is meshed by $50 \times 30 \times 40$ in the corresponding directions. The reaction force on the top plane is recorded as a function of the displacement by which it is quasistatically compressed down for post analysis to get the shear moduli of both layers. The simulation is run in commercial finite element package ABAQUS 6.11. The extraction of shear modulus of the stiff layer from experimental data is straightforward. As for a given geometry and only one neo Hookean material, the reaction force on the glitter is linear in its shear modulus G. A test simulation with modulus G0 is run, and thus $G = cG0$, where the coefficient c is determined from the least-squares fitting between the simulation curve and the experimental data. Only first 5 to 8 points at which the compression displacement is relatively small are used for the numerical fit to determine c because in the strongly nonlinear regime stiffening occurs in most polymer materials and neo Hookean constitutive model is no longer valid. We also fit the 5 individual measurements separately and then take the mean of the fitted moduli. The two results are almost identical. Knowing the modulus of the stiff layer, in order to get that of the soft layer, we

compress the two layers together laterally. As the dependence of reaction force on the moduli of both layers is implicit, we have to repeat the simulation many times varying the modulus of the soft layer while keeping that of the stiff layer the same until the experimental data is enclosed by a narrow range of simulation curves with different moduli. Within this region, linear interpolation of curves with prescribed moduli is adopted to best match the experimental data by the least-squares fitting. Again, we fit both the averaged curve and the 5 individual measurements separately and then average the moduli. The two results are almost identical.

Supplemental Figures:

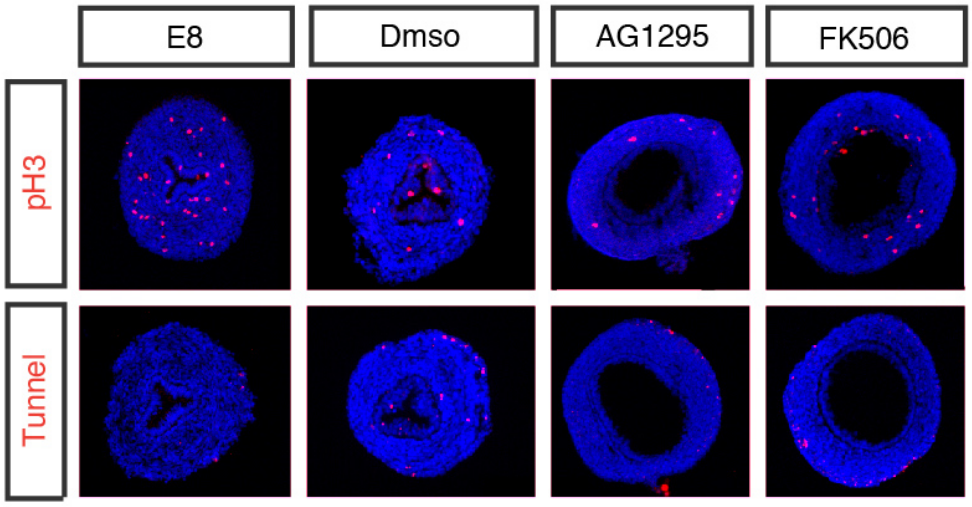

Figure S1: AG1295 and FK506 do not impact proliferation or cell death. E6 chick gut segments were grown in culture for 48 hours, compare with guts collected from E8 embryos, left. While levels of proliferation (top) are lower *in vitro* than to *in vivo,* gut segments cultured in the presence of either AG1295 or FK506 do not display significantly altered proliferation when compared to segments grown in drug vehicle alone. Additionally, while there is slightly more cell death (bottom) in guts grown *in vitro* than *in vivo*, segments grown in the presence of either drug do not exhibit more cell death than those grown in vehicle alone.

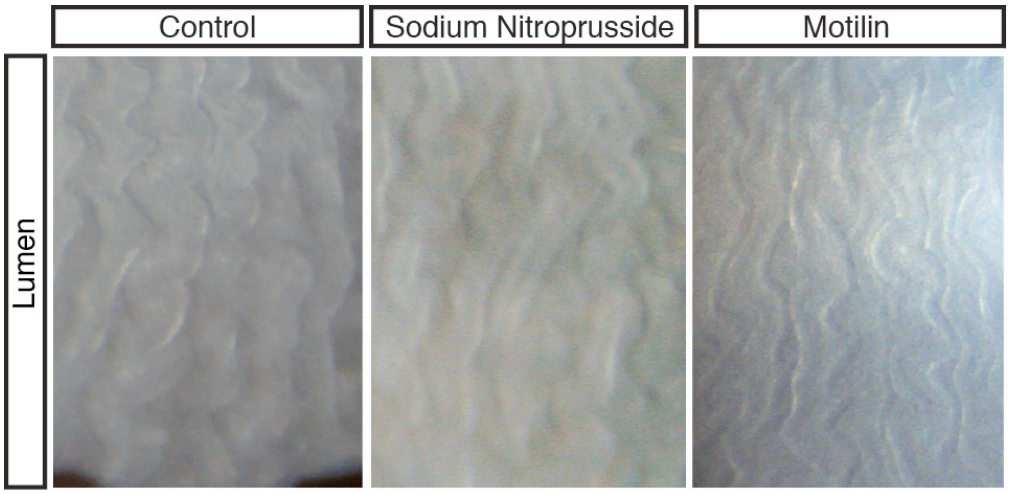

Figure S2: Peristaltic contraction is not involved in the formation of zigzags. E12 guts were cultured for 48 hours with either sodium nitroprssuide or motilin or no drug (control). Sodium nitroprusside inhibits contraction and motilin stimulates contraction, in all cases zigzags begins to form.

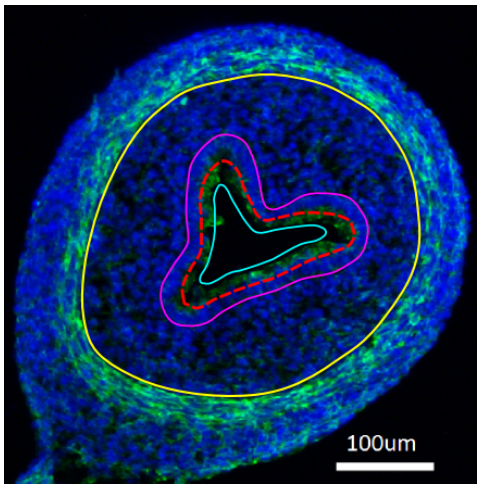

Figure S3: Segmentation of a cross-section. Solid lines show the outer circumference S_0 of the mesenchyme (yellow), outer circumference of the endoderm (magenta) and inner circumference of the endoderm (cyan). The dashed red line is the mean circumference S_e of the endoderm that is plotted in Figs. 4A and 6C. Thickness of the deformed endoderm can be approximated as the area occupied by the endoderm divided by S_e.

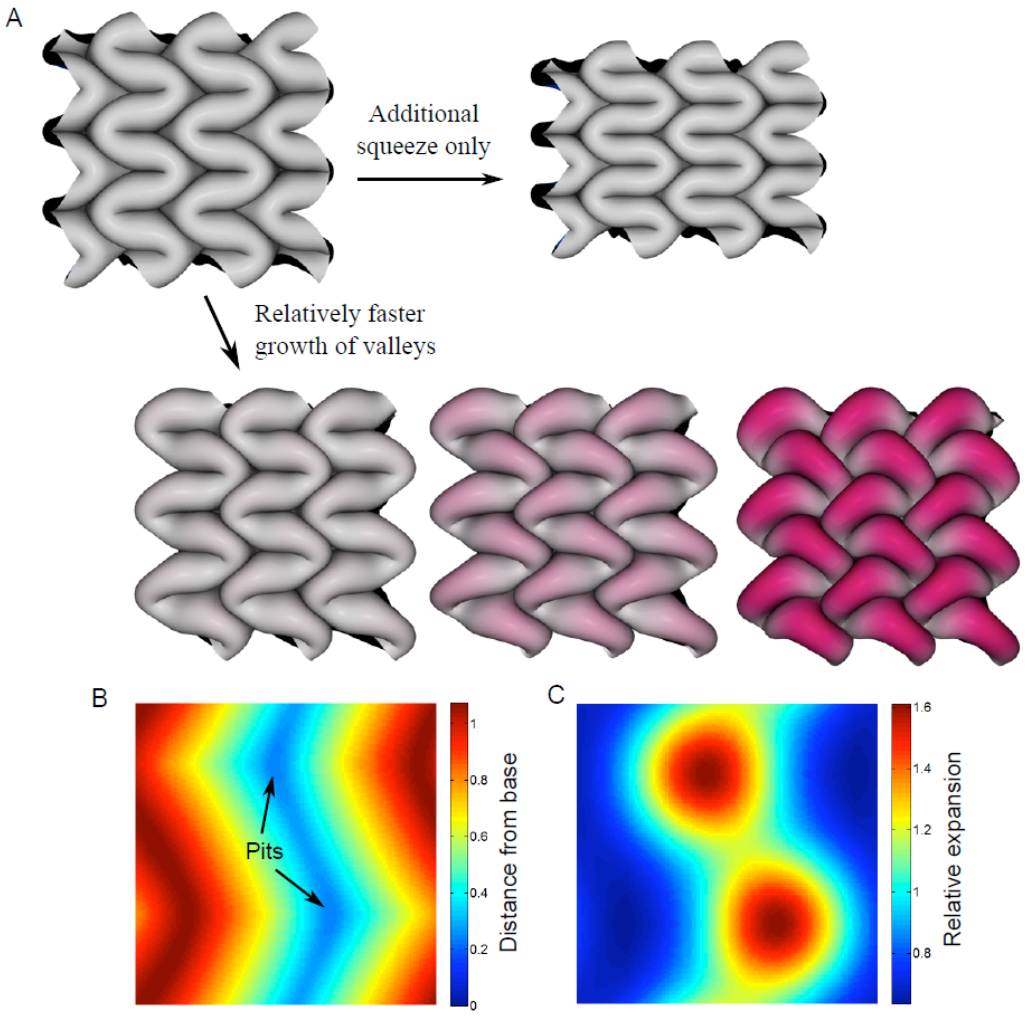

Figure S4: Localized growth of a zigzag pattern leads to twisting and bulging of arms. (**A**) A zigzag pattern resulting from uniform growth is show top left. With additional longitudinal compression the zigzags only squeeze, preserving the up/down reflection symmetry. The cascade on bottom shows the twisting and up/down symmetry breaking due to enhanced growth of the valleys (parameterized time t = 0.5, 0.75, and 1 from left to right). The applied growth map is shown in **C** for $t = 1$. The growth map is based on the depth map of the original zigzag pattern (**B**) such that peak growth occurs at the zigzag pits. Purple areas in simulation snapshots have the highest expansion, corresponding to the maxima in the growth map and minima in the height map.

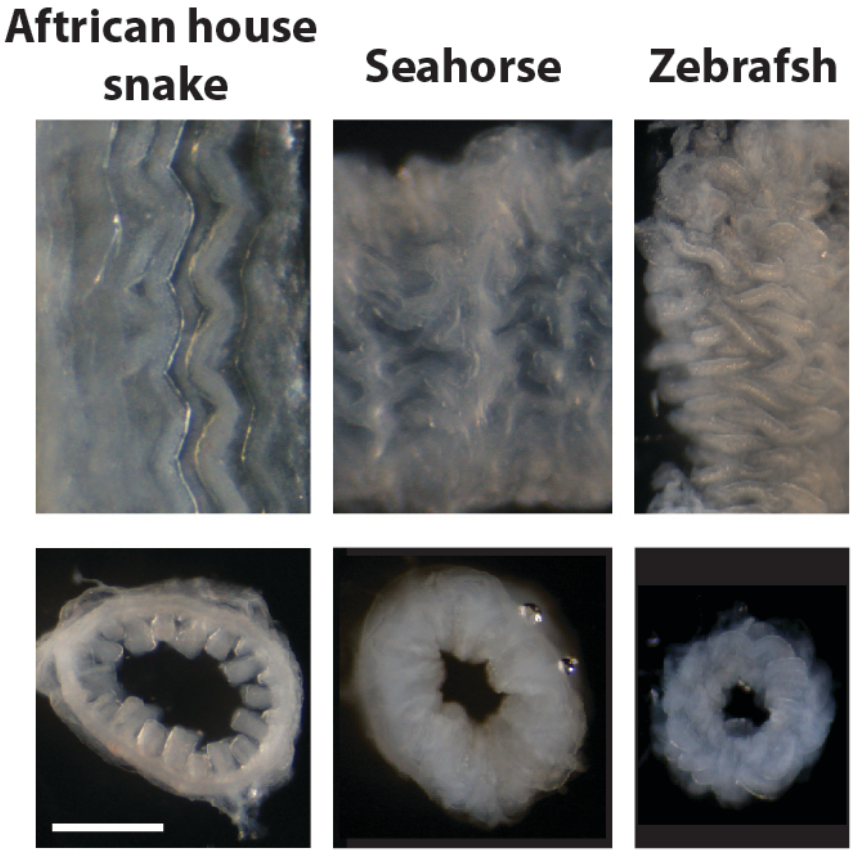

Figure S5: The patterns seen on the luminal surface of the gut vary across species.

Luminal views (top) and cross sectional view (bottom) of guts of various species. The African house snake gut at E55 shortly before hatching (left) has tall flat zigzags. The adult seahorse gut (middle) has disorganized zigzags with lateral extensions. The zebrafish gut (right) has short zigzagging protrusions that are oriented laterally. Scale bar is 500μm

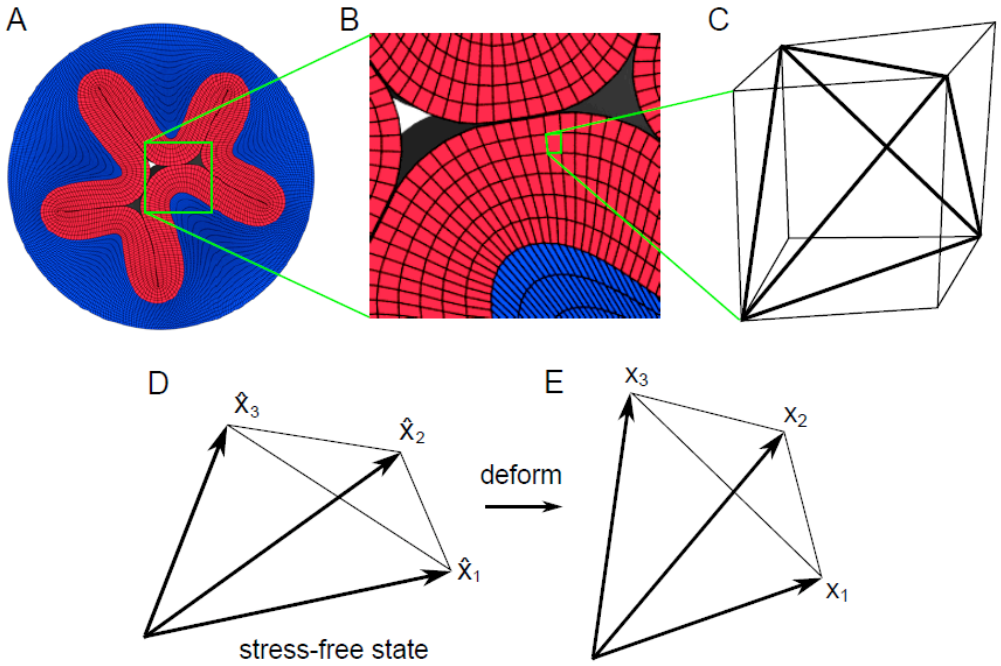

Figure S6: Computational model for the mesenchyme-endoderm tube. (**A**) A composite of elastic mesenchyme (blue) and endoderm (red) layers is squeezed into a cylindrical tube. (**B**) A magnified view of the deformed mesh. (**C**) A schematic of a primitive rectangle showing the arrangement of its five tetrahedrons. Schematic stress-free and deformed states of a tetrahedron are shown in **D** and **E**, respectively.